Assessing the impact of land use changes in South Holland on the local weather using HARMONIE-Climate

Building bridges between water management, climate physics and vector-borne viral outbreaks

A.E.W. (Annelot) Broerze

Delft University of Technology

TU Delft

Assessing the impact of land use changes in South Holland on the local weather using HARMONIE-Climate

Building bridges between water management, climate physics and vector-borne viral outbreaks

by

A.E.W. (Annelot) Broerze

to obtain a masters degree in Applied Physics

at the Delft University of Technology,

to be defended publicly on December 1st, 2023 at 11:00.

Student number:	4727339	
Thesis committee:	Dr. S.R. (Stephan) de Roode,	Delft University of Technology, supervisor
	Prof. dr. A.P. (Pier) Siebesma	Delft University of Technology
	Prof. dr. M. (Marileen) Dogterom	Delft University of Technology, KNAW

TU Delft Delft University of Technology

Acknowledgements

First of all, I would like to thank Pier Siebesma (TUD) and Marileen Dogterom (TUD, KNAW) for being part of my thesis committee.

Next, I want to greatly thank my supervisor Stephan de Roode. A year ago I stepped into your office mentioning I wanted to conduct a project in either atmospheric or health physics, and you proposed the perfect opportunity to combine my interests. Now a year later, I look back happily on a period pioneering in this field of research together and I think we can finally state that we understand the language of all the new research facets we have bumped into and can soon leave our dictionary at home. You have guided and challenged me every week, through long sessions together discussing the progress and sharing a bunch of fun anecdotes. Your enthusiasm about almost everything kept me excited along the way and further sparked my interest in this research field. Also, the endless feedback improved my research significantly. Thank you very much!

A big thanks to Maarten Boonekamp, who has supported me along the way, from getting started in HCLIM, to frustrating FORTRAN debugging sessions, challenging me to improve my research by asking the right questions, and providing feedback. But foremost, you were someone I could always ask any questions to and have a lot of fun with along the way! The project is now all yours, so make me proud.

I would like to greatly thank Bert van Ulft (KNMI) for his endless help with the challenges I faced during experimenting with HARMONIE-Climate, debugging all the faced issues during simulations, and always answering my questions quickly. Thank you Natalie Theeuwes for getting me up and running at the KNMI.

Many thanks to all who were present at the monthly meetings of the PDPC Frontrunner group 1, Climate change and vector-borne virus outbreaks: Pier Siebesma (TUD), Reina Sikkema, Tijmen Hartung (Virology, EMC), Maarten Schrama, Jordy van der Beek (CML Leiden University), Sander Koenraadt (WUR), Henk van der Jeugd (NIOO) and Eldar (UvA). A whole new interesting world has opened up for me, and your assistance in educating me on subjects like mosquito development, bird migration and vector-borne viruses, were crucial to succeed in this project. Hopefully, the results of this study serve as a first stepping stone from the TUD group and enhances it this great interdisciplinary research collaboration!

Also, I want to express my gratitude to all who have discussed land use scenarios and integration techniques with me: Marco Hoogvliet (Deltares), Fransje Hooijmeijer (BK, TU Delft), Bart Rijken (PBL), Bas van Bemmel (PBL), Martha Dellar (CML Leiden University, Deltares), Coen Kramer (alumnus TU Delft), Clara Sanchez and Ivan Paden (BK, TU Delft). Your assistance and enthusiasm aided me a lot in governing through all possible scenarios, leading to a better understanding of the background processes and improving my work on assessing the scenarios.

Abstract

The escalating global threat of arboviral infections, influenced by climate-related hazards, emphasizes the pressing need to explore the relationship between climate change and mosquito-borne viral outbreaks. The role of land use change is critical, significantly impacting the thermal and humidity fluctuations, resulting in changing bird and mosquito habitats in the urban delta.

The impact of new water areas in South Holland on local weather through HARMONIE-Climate (HCLIM) simulations is studied. The physics of surface-atmosphere interaction using the SURFEX and FLake models are examined, and HCLIM hindcast outputs are validated against KNMI and TU Delft weather stations located around Rotterdam, revealing an urban heat island effect. Notably, during a heatwave, HCLIM overestimates temperature and underestimates specific humidity, while on regular summer days, both variables are underestimated. Multiple existing land use scenarios, assessed through Multi-Decision Criteria Analysis, lead to the selection of a potential water buffer east of Zoetermeer (20.1 km^2). Technical modifications in HCLIM's physiographic data package ECOCLIMAP-SG and GlobalLakeDatabase are used for simulating new lakes or wetlands at this location on a 2.5 by 2.5 km grid from April 1, 2022, to October 1, 2022. Results highlight clear temperature increases over new lakes, compared to agricultural land use, with a time-mean local rise of 2.4 K for the surface temperature and 0.65 K for the atmospheric temperature. Specific humidity shows a time-mean increase of 1 g/kg. Nighttime positive sensible heat flux above lakes contributes to constant air warming, while latent heat flux continuously moistens the air. Studying the FLake model through a one-day simulation during a heatwave on August 12th, 2022, emphasizes the critical need for a spin-up period, accounting for low-resolution mean climatological initial values and further interpreting water column temperatures.

The study recommends future research extends simulations over multiple years with higher resolution, including winter periods. Findings reveal large water bodies can unintentionally heighten heat-humidity risks, potentially amplifying vector-borne viral outbreaks in developing blue-green areas in South Holland. Emphasizing interdisciplinary research, this research highlights the importance of thoughtful land use planning in policy and urban development to safeguard public health amid changing environmental conditions.

Contents

List Of Abbreviations v

1 Introduction **1**
1.1 Global climate change as a driver of viral outbreaks 1
1.2 Research approach 4

2 Surface physics in the HARMONIE-Climate model **7**
2.1 HARMONIE-Climate model 7
2.2 SURFEX model 8
2.2.1 The land cover database ECOCLIMAP 8
2.2.2 The gridded GlobalLakeDatabase 9
2.3 SURFEX workflow within HCLIM 10
2.4 The fresh water lake model FLake 12
2.5 Initalization of FLake variables in lakes 14
2.6 Fluxes in the convective boundary layer and at the surface 15
2.6.1 Heat, water and momentum budgets 16
2.6.2 The surface energy balance (SEB) 17
2.6.3 Radiative fluxes 19

3 Comparing HCLIM model results with weather stations observations **21**
3.1 Data sources, experimental set-up and processing methods 21
3.1.1 TU Delft weather stations in Rotterdam 21
3.1.2 KNMI automatic weather stations 22
3.1.3 HCLIM model output 22
3.1.4 Experimental set-up 22
3.2 Results 23
3.2.1 Temperature 23
3.2.2 Specific humidity 26
3.3 Discussion and conclusion 28

4 From land use change scenarios to water storage areas **29**
4.1 Introduction to scenarios 29
4.1.1 Opportunity map Climate buffers 29
4.1.2 Ruimtelijke verkenning 30
4.1.3 Delta Scenarios 31
4.1.4 Redesigning Delta's: Project Delfland 31
4.1.5 A climate-proof buffer for South Holland 32
4.2 Introduction to assessment method: Multi-Criteria Decision Analysis 33
4.3 Assessment of scenarios 34

5 Case set-up **37**
5.1 Periods of interest 37

5.1.1 Weather conditions for mosquito, bird and viral transmission . . . 37
5.1.2 Simulation period . . . 39
5.2 Methods to modify land use maps . . . 39
5.3 Experimental HCLIM system set-up . . . 42
5.3.1 Lake, wetland and control experiments . . . 43
5.3.2 Flake model monitoring experiments . . . 44
5.4 Pre-study of spin-up period within simulations . . . 45
5.5 Processing methods . . . 47

6 Results and discussion **49**
6.1 Temperatures, specific humidity and wind speed . . . 49
6.1.1 Temperature . . . 49
6.1.2 Specific humidity . . . 53
6.1.3 Wind speed . . . 53
6.2 The changing surface energy balance . . . 55
6.2.1 Sensible heat flux . . . 55
6.2.2 Latent heat flux . . . 56
6.2.3 Shortwave radiation . . . 58
6.2.4 Longwave radiation . . . 59
6.3 Relations between prognostic variables and turbulent fluxes . . . 59
6.4 Case study: observing the cold start initialization and diurnal cycle of FLake variables 61

7 Conclusion and recommendations **65**
7.1 Research insights and conclusions . . . 65
7.1.1 Pre-studies and methodology . . . 65
7.1.2 The effect of changes in local land use on the local weather . . . 66
7.2 Recommendations for future research . . . 68

A Retrospective on research choices **71**
A.1 A wide-scale collection of land use scenarios . . . 71
A.2 Approach on selection weather periods of interest . . . 72

B Process background on modifying the HCLIM system for experimental purposes **74**
B.1 Modifying physiographic data files . . . 74
B.1.1 Code for preprocessing: from QGIS to ECOCLIMAP coordinates . . . 74
B.1.2 Modification in ECOCLIMAP-SG . . . 76
B.1.3 Changes in HCLIM system . . . 79
B.2 Monitoring Flake output experiments . . . 81
B.2.1 Technical details . . . 81
B.3 High resolution experiments . . . 83
B.3.1 Technical details . . . 83

C Additional figures **85**

D Air thermodynamics **89**

Bibliography **91**

List of abbreviations

ABL	Atmospheric Boundary Layer
AHN	Algemene Hoogtekaart Nederland
CAS	Stichting Climate Adaptation Services
CBL	Convective Boundary Layer
CESAR	Cabauw Experimental Site for Atmospheric Research
CNRM	Centre National de Recherches Météorologiques
CPB	Centraal Plan Bureau
EID	Emerging Infectious Diseases
ECWMF	European Centre for Medium-Range Weather Forecasts
ERA5	Fifth Generation of the ECMWF ReAnalysis
FLAKE	Fresh-water Lake Model
GLD	Global Lake Database
HARMONIE	HIRLAM ALADIN Research on Mesoscale Operational NWP in Euromed
HCLIM	HARMONIE-Climate
HIRLAM	High-Resolution Limited Area Model
IDAlert	Infectious Disease decision-support tools and Alert systems
IFS	Integrated Forecast System
ISBA	Interactions between the Surface Biosphere Atmosphere
KNMI	Koninklijk Nederlands Meteorologisch Instituut
MCDA	Multi Decision Criteria Analysis
NAP	Normaal Amsterdams Peil
NWP	Numerical Weather Prediction
OneHealthPACT	OneHealth Predicting Arboviruses Climate Tipping points
PDPC	Pandemic & Disaster Preparedness Centre
PBL	Planbureau voor de Leefomgeving
PGD	PhysioGraphic Data
SURFEX	Surface Externalisée
TEB	Town Energy Balance
USUV	Usutu Virus
WNV	West Nile Virus

1

Introduction

1.1. Global climate change as a driver of viral outbreaks

One of the fast-expanding global health threats is the risk of arboviral infections (Weaver and Reisen, 2010; Pierson and Diamond, 2020). Around 58% of infectious diseases affecting the global population have been demonstrated to be influenced by climate-related hazards (Mora et al., 2022). Global pandemics are primarily due to the transport of viruses from animals to humans (zoonotic transport), as seen with SARS, Coronavirus, Ebola, and HIV (Loh et al., 2015). Heat maps predicting the relative risk distribution of zoonotic emerging infectious diseases (EID) events point out that there is also a substantial risk in the Netherlands, as can be seen in figure 1.1 (Allen et al., 2017). Risk distributions are dependent on numerous predictors, such as human and animal behavior, but also environmental developments. One of the key drivers of EID events is changes in land use, which disrupts ecosystems (Morse, 1995; Wolfe et al., 2007; Murray and Daszak, 2013; Allen et al., 2017).

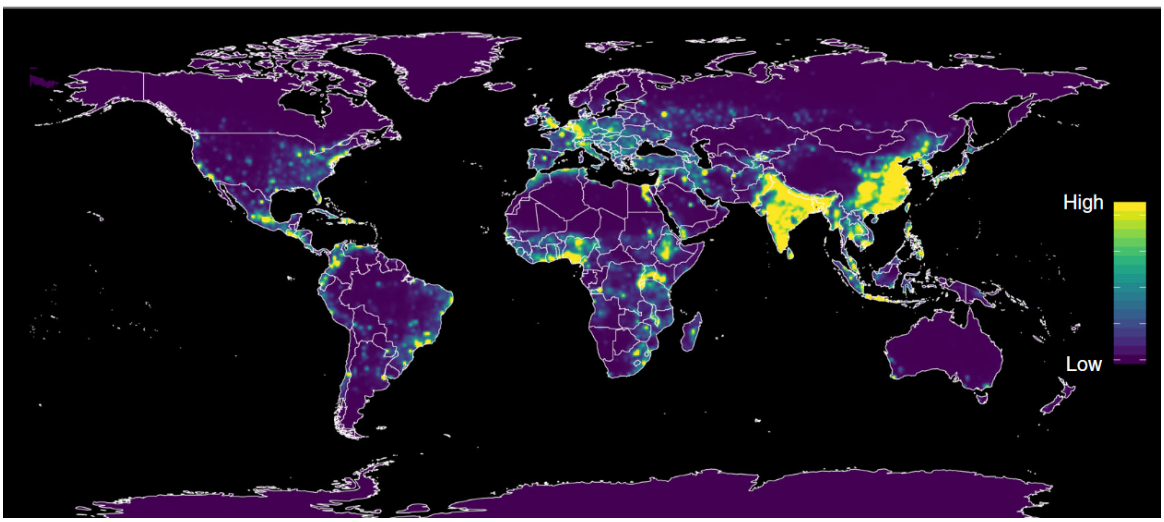

Figure 1.1: A heat map illustrating the predicted distribution of relative risk for zoonotic emerging infectious disease (EID) events. The map indicates the estimated risk at various locations, considering the influence of reporting bias. The model output, which is weighted by population, is utilized to provide a more accurate representation of the risk across different regions. Directly adopted from Allen et al. (2017).

Studies not only reveal the growing threat by impact on global health risks but also great global economy and security impacts resulting in potential economic liability of billions of dollars (Jones et al., 2008; Romanello et al., 2023).

Therefore, an interest in the relationship between climate change and its effect on arboviral emergence has grown over the past decade. Possible climatological drivers contributing to viral outbreaks are increasing temperatures, changing precipitation patterns, and increasing frequency and severity of extreme weather events, such as extreme drought followed by extreme precipitation (Carlson et al., 2022; Baker et al., 2022). Also, climate change affects the salinization of inland waters. This is caused by rising sea levels (0.3 - 1.2m increase by the end of the century), interacting with increasing evaporation (due to higher solar radiation and warmer summers), subsidence of soils (0.6 cm/year) and lower supply of fresh water in rivers in the summer (Koster et al., 2018; KNMI, b, 2023).

Next to global climate change and salinization, the wide-scale land use changes are frequently proven to have a significant impact on the diurnal atmospheric temperature range and the water-energy balance (Dai et al., 1999; Bounoua et al., 2002; Zhang et al., 2007; Sterling et al., 2013; Mahmood et al., 2014). Currently, land use change is evolving rapidly, due to human intervention leading to urbanization and deforestation (Kalnay and Cai, 2003; Angel et al., 2011), and will continue to do so in the coming decades (Mahmood et al., 2010). In the Netherlands, the main land cover changes entail the growth of agricultural and urbanized areas (Verburg et al., 2004). Small-scale studies have been performed on the effects of land use change in The Netherlands, showing higher precipitation levels both in summer and winter (Daniels et al., 2016; Boonekamp, 2023).

Mosquitoes can transmit vector-borne viruses, such as the West Nile Virus (WNV) and Usutu Virus (USUV), which are often carried by the mosquito type *Culex pipiens*. Climate change and ecological developments are anticipated to increase the risk of viral outbreaks caused by mosquitoes, highlighting the significance of predicting and preventing such outbreaks (Calzolari et al., 2012; Daniels et al., 2016). This is because changing climatology leads to higher suitability for mosquitoes with a vector potential, expanding its presence in Europe (Iwamura et al., 2020; Colón-González et al., 2021; van Daalen et al., 2022; Lührsen et al., 2023). In recent years, USUV (2016) and WNV (2020) make their entrance to the Netherlands more often, leading to enzoonotic transmission (Duijster et al., 2016; Rijks et al., 2016; Oude Munnink et al., 2020; Sikkema et al., 2020) and occasionally human spill-over (Vlaskamp et al., 2020; Zaaijer et al., 2019). Ongoing climate change will likely continue to alter vector-borne disease patterns, due to the susceptibility of mosquitoes to thermal and humidity fluctuations (Vogels et al., 2016; Rogers and Randolph, 2006; Brown et al., 2023). These fluctuations disturb the traits like mosquito growth rate, metabolic rate, lifespan, biting rate, and infection and transmission probabilities of vector-borne viruses (Vogels et al., 2017; Brown et al., 2023). The temperature-trait relationships are incorporated in models, together making up the reproduction number R_0. A larger value for R_0 indicates a higher risk of disease establishment in a certain area (Vogels et al., 2017; Brown et al., 2023). An illustration of the thermal relation to the reproductive number is provided in figure 1.2. Therefore it is necessary to set up surveillance studies and project the risk of mosquito-borne diseases in Europe and within the Netherlands (Farooq et al., 2022).

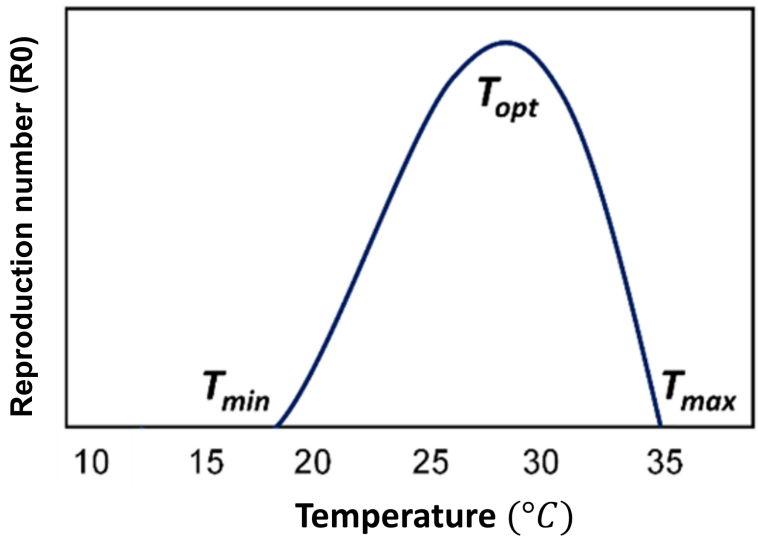

Figure 1.2: An illustration of the thermal relation to the reproduction number R_0. A higher R_0 implies a greater risk of infectious disease establishment in a certain region. Here, $T_{\text{min}} \approx 17$ °C, $T_{\text{opt}} \approx 28$ °C and $T_{\text{max}} \approx 35$ °C. Directly adopted from Brown et al. (2023).

Furthermore, mosquitoes interact with bird populations in their habitats, such as wetlands that predominate the Dutch Delta. Policy planning scenarios indicate an increase of wetlands for climate mitigation (Kuiper et al., 2023). Together with changes in climatology, bird migration patterns might alter. Overall, the anticipated changes in heat and humidity in the Netherlands increase the risk of potential viral pandemic outbreaks. These emerging risks call for an interdisciplinary and cross-doctoral approach (biomedical, social, economic, environmental, political and behavioral) to quantify and mitigate risk. This has led to several international collaboration consortia, such as the Lancet Countdown, Infectious Disease decision-support tools and Alert systems (IDAlert), and OneHealth Predicting Arboviruses Climate Tipping points (OneHealthPACT). Recently, the interdisciplinary national research program Pandemic Disaster Research Centre (PDCP) has been set up, to research various topics about preventing EID events and how to act during EID events. One of the so-called Frontrunner projects is "Climate change and vector-borne virus outbreaks", aiming to answer the question:

How will climate change, changes in water management, and increase in salinization and salt intrusion in deltas affect mosquito and bird populations and their role in direct or indirect transmission of zoonotic pathogens to humans?

A ramification of the Frontrunner project and its work packages (WP) is provided in figure 1.3.

Within the work package climate change, salinization and land use change (WP1), it is necessary to run simulations projecting these expectations and interventions. For this, HARMONIE-Climate (HCLIM) will be used as a climate modeling tool, which is short for HIRLAM-ALADIN Research on Mesoscale Operation NWP In EuroMED Climate. HARMONIE is a model configuration, based on the AROME model operated by HIRLAM countries (all in Europe), and used by the KNMI to run 48-hour weather forecasts for national purposes (Bengtsson et al., 2017; Seity et al., 2010). It is necessary to gain knowledge on technically adapting the physiographic data files serving as input for a climate model, such that land use change can be studied. For example, the establishment of water buffer areas to store excessive precipitation. The primary objective of this research is to technically enable the study of land use change in the HCLIM model and examine the impact of land use

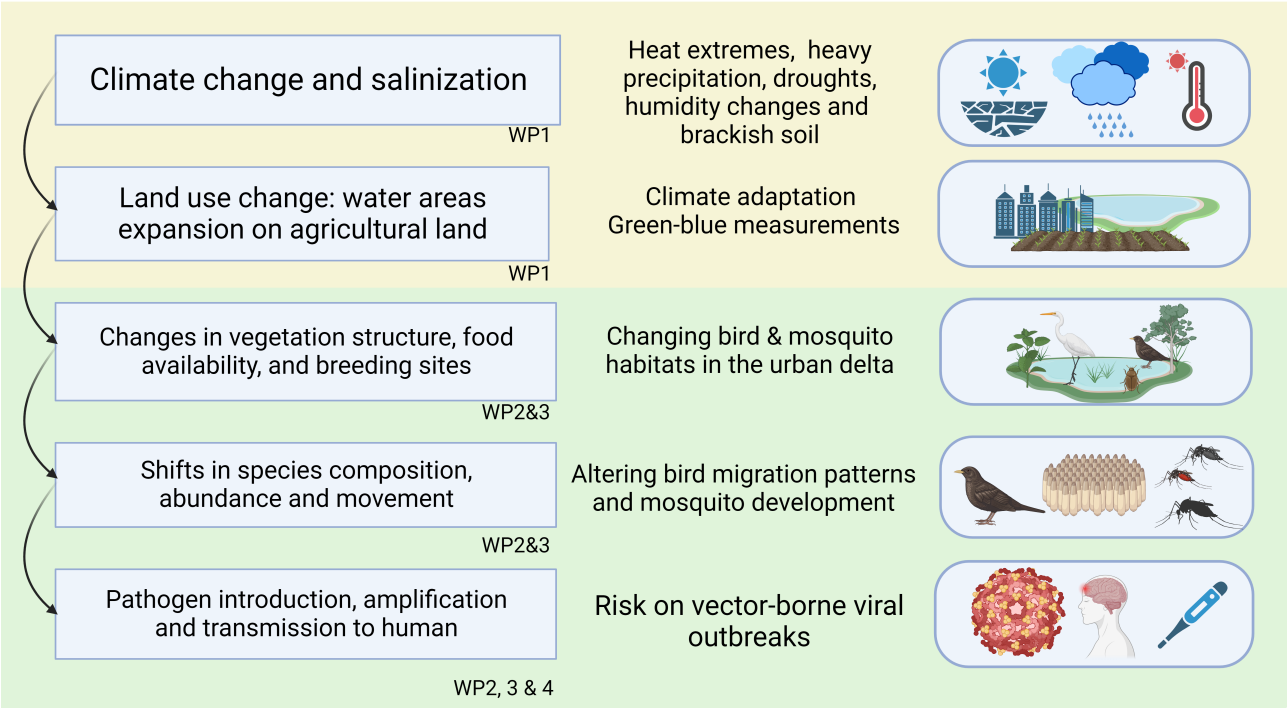

Figure 1.3: An overview of the work packages (WP) within the Frontrunner project "Climate change and vector-borne virus outbreaks". This study is conducted in the light of the WP1. Design by Author, inspired by `https://convergence.nl/`

change scenarios on local weather patterns. As this research is conducted within the framework of the Frontrunner project's Workpackage 1, the focus lies on land use changes in the form of creating new wetlands or lakes. Some studies have investigated lake-atmosphere interactions for large, predominantly high-level lakes using datasets of observations, highlighting increases in temperatures and humidity (Wang et al., 2019; Meng et al., 2023). Another study mimicking the creation of blue areas for urban heat island mitigation, suggests the size and shape of the water bodies are crucial for the impact on temperature, humidity levels, and horizontal wind speed (Ampatzidis et al., 2023). However, no research has been conducted on the effects of creating new water areas by changing the physiographic data maps using HARMONIE-Climate.

Therefore, the main question this study aims to answer is:

How will the development of new water areas in South Holland affect the local weather?

To further elaborate on the posed research question, the research approach is outlined below. Simultaneously, the outline of the thesis report is provided.

1.2. Research approach

To assess the impact of land use change on local weather, the land use cover files of a climate model must be changed. The differences can be studied by comparing simulation results with modified land use to a reference simulation. To this end, the climate model HCLIM is used. All the relevant physics comprises an elaborate collection of Fortran subroutines. Therefore, an effort must be made to understand the working mechanism of the HCLIM system, its relevant subroutines, and physical parameterizations. Mainly parts of the model physics package relevant to the

project, such as the physics of the surface-atmosphere interaction and the incorporation of the physiographic data files, are studied. The surface-atmospheric interface is simulated with a surface scheme named Surface Externalisée (SURFEX) and its sub-models for different surface types (Masson et al., 2013). A description of the characteristics and physics of HCLIM, SURFEX, and other relevant surface-atmospheric interaction models is provided in chapter 2. Furthermore, the relevant governing equations and physical concepts are given.

In this study, the effects are studied through hindcasting, which means using historical weather data to simulate and analyze past weather events. To validate whether HCLIM hindcast output is biased within the Rotterdam Delta area, a study has been done by comparing the output of HCLIM with eight weather stations placed by the Delft University of Technology and KNMI stations in the city of Rotterdam and its near vicinity. This is done under different weather conditions and also compared to data provided by the measuring tower at Cabauw, which is located in a rural area. The second goal is to assess how the model predictions and observations in urban areas compare to rural areas, and whether an urban heat island effect is observed. The heterogeneity of the weather station observations is also relevant for the international IDAlert project, as they have expressed their profound interest in the urban climate of Rotterdam. A similar study comparing observations of TU Delft, KNMI, and Wunderbar weather stations during extreme heat and wind conditions has been done, indicating that the location of placement plays a dominant role in the heterogeneity between the observations (Damen, 2021). The method and results of this validation are presented in chapter 3.

In chapter 4 we assess future scenarios through anticipated land use change, focusing on potential water storage areas in South Holland. In the past years, numerous national and regional spatial development scenarios have been developed, which indicate possible land use changes (ZUS et al., 2022; Wolters et al., 2018; Kramer, 2023; Kuiper et al., 2023; CAS, 2023). Such scenarios present information on water management to mitigate the impacts of climate change-induced weather extremes, such as future risk of flooding and drought events, incorporating socio-economic factors. In the Netherlands, where water management is critical, these water storage areas can play a crucial role in creating a more climate-resilient and water-robust landscape. By conducting meetings with scenario developers and assessing the scenarios using the Multi Decision Criteria Analysis method, we provide input for the final experimental set-up.

The case set-up is presented in chapter 5. To align the results with the interests of ornithologists, entomologists, and virologists, a period of interest for the HCLIM simulations is depicted, in particular a selected period with weather conditions enhancing mosquito development, bird migration, and viral outbreaks. This will further be discussed in section 5.1. In addition, a procedural framework is provided for technically altering the physiographic input files for the model, a follow-up to the work presented in Boonekamp (2023) for studying land use changes on precipitation levels with HCLIM. Finally, this chapter addresses the experimental configuration of the HCLIM system and the associated data processing methodologies.

After this, simulations can be done for the entire case setup. Following this, the results will be analyzed and compared, using variables such as surface and water temperature, specific humidity, and wind speed. The results will be presented and discussed in chapter 6.

To summarize,

- Chapter 2 explores the working mechanism of HCLIM, SURFEX, its submodels and all relevant physical concepts.
- Chapter 3 compares TU Delft and KNMI weather station data with HCLIM model results, to

detect biases and urban-rural differences.

- Chapter 4 discusses possible future land use scenarios in South Holland and assesses them with a Multi Decision Criteria Analysis.
- Chapter 5 describes the entire case set-up: weather conditions likely increasing mosquito-borne viral outbreaks, the procedure to technically adapt the physiographic data files that serve as input for land use cover in the HCLIM system, and all experimental configurations and data processing methodologies.
- Chapter 6 presents and discusses the results of the simulations.

From the results, we will draw conclusions based on the evident effects of land use change on the local weather patterns, such as the modeled local rise of temperature and humidity above water areas. The results will be used to further develop and extend the research of the Frontrunner project of PDPC. Following this, recommendations are provided in chapter 7.

2

Surface physics in the HARMONIE-Climate model

In this chapter, some key aspects of the models used in the present research, most notably the surface and lake models, and the relevant physics behind them are discussed. In section 2.1, the HARMONIE-Climate model (HCLIM) is outlined. Section 2.2 further explores the model covering the surface-atmosphere processes. The workflow of the surface model embedded within HCLIM is described in section 2.3. The embedded model for surface areas encompassing inland water is described in section 2.4 and the way lake-related variables are initialized is discussed in section 2.5. Lastly, relevant physical principles at the surface-atmosphere interface are discussed in 2.6.

2.1. HARMONIE-Climate model

HCLIM is a regional climate modeling system based on the numerical weather prediction (NWP) model HARMONIE (Bengtsson et al., 2017; Seity et al., 2010; Belušić et al., 2020). The fine spatial and temporal resolution of HCLIM allows for deep convection-permitting modeling. This atmospheric forecasting model finds its foundation in numerically solving a governing system of equations (Warner, 2012). These equations include the momentum equations for a spherical earth, which are based on Newton's second law of motion. The thermodynamic energy or heat equations take into account diabatic effects on temperature, such as the warming of air due to the absorption of infrared radiation and the release of latent heat. The continuity equation for total mass specifies that mass is conserved and the water vapor-specific humidity equation is a conservation equation that applies solely to water vapor. Additionally, the ideal gas law relates temperature, pressure, and density. The model is embedded in the European Centre for Medium-Range Weather Forecasts (ECMWF) model, which routinely provides lateral boundary conditions through ERA5 re-analysis results (ECMWF, 2010).

HCLIM entails the whole script required for data assimilation, climate generation, lateral coupling, forecasting, and postprocessing. The reference cycle cy43h currently used by the KNMI uses 65 levels in the vertical, with the model top at 10 hPa and the lowest level of 12 m. The default model grid of HCLIM comprises a spatial resolution of 2.5 km by 2.5 km grid cells, with a model time step of 75 s. The lowest grid cells of the atmospheric column are covered by different surface types, such as water, town, and nature, all with their physical distinct properties. The model dynamics and physics are therefore covered through extensive physical parametrization schemes and submodels embedded in HCLIM. The model physics can be subdivided into radiation, cloud micro-

physics, turbulence, convection, and surface. The surface physics is solved through an external module structured code called SURFEX, which can be embedded inside meteorological models like HCLIM (Masson et al., 2013).

2.2. SURFEX model

In this section, we will discuss the SURFEX model and its underlying databases (subsections 2.2.1 and 2.2.2). As the goal is to evaluate the effect of changes in local land use and the entire HCLIM model physics is too comprehensive, a focus lies on studying the processes close to the surface-atmosphere interface. SURFEX composes various physical schemes for each type of land use to simulate fluxes between the surface and the atmosphere. To accurately estimate surface fluxes over a wide range of spatial resolutions and to account for heterogeneities in the grid box, a tiling approach is used, which is visualized in figure 2.1. SURFEX has a grid mesh where the surface is divided into several homogeneous tiles. Each tile receives the same atmospheric forcing from the lowest model level and calculates its respective fluxes. The fluxes are then averaged over the area in the atmospheric model grid box and returned to the atmosphere. There is no horizontal transfer between the tiles. There are four types of surface tiles: sea/ocean, inland water, nature, or urban/town.

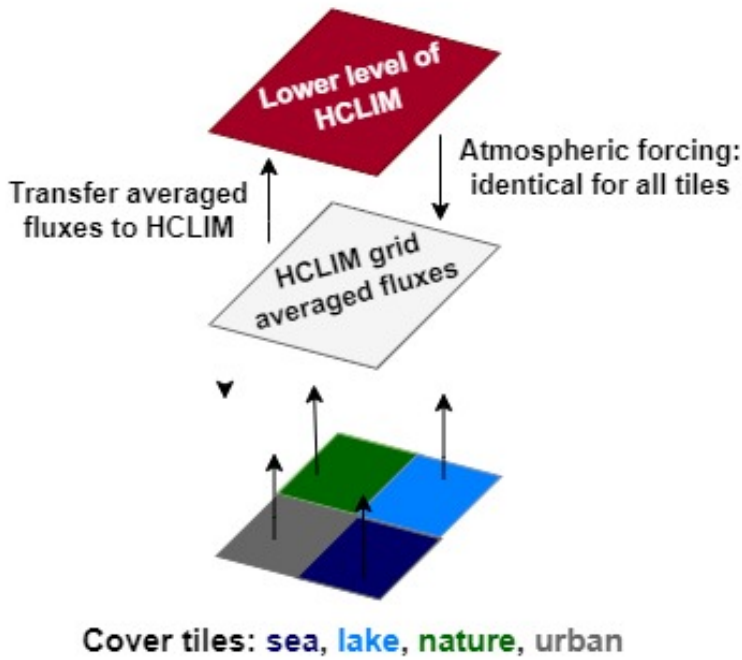

Figure 2.1: A simplified illustration of the processes between HCLIM and the SURFEX model. Designed by author after SURFEX course material (CNRM, 2023).

2.2.1. The land cover database ECOCLIMAP

ECOCLIMAP is the CNRM (Centre National de Recherches Météorologiques) home-made global database of land covers (CNRM, 2018). It describes the various surface types covering the Earth, and associated parameters linked to land surface maps. Multiple iterations of the database have been created (Faroux et al., 2013), with the second-generation variant, ECOCLIMAP-SG, currently in use. One of the physiographic files `ecosg_final_map.dir` includes a map comprising 33 diverse cover types, and each grid point is assigned solely one type. The map features a horizontal

spatial resolution of approximately 300 meters. As mentioned, the four primary categories include sea, inland water, nature, and town, of which the latter two are comprised of 19 and 9 subtypes, respectively. The 19 'natural' functional subtypes include for example crops, wetlands, grasslands, and forest types. A visualization of `ecosg_final_map.dir` for the Netherlands with its respective cover types is displayed in figure 2.2.

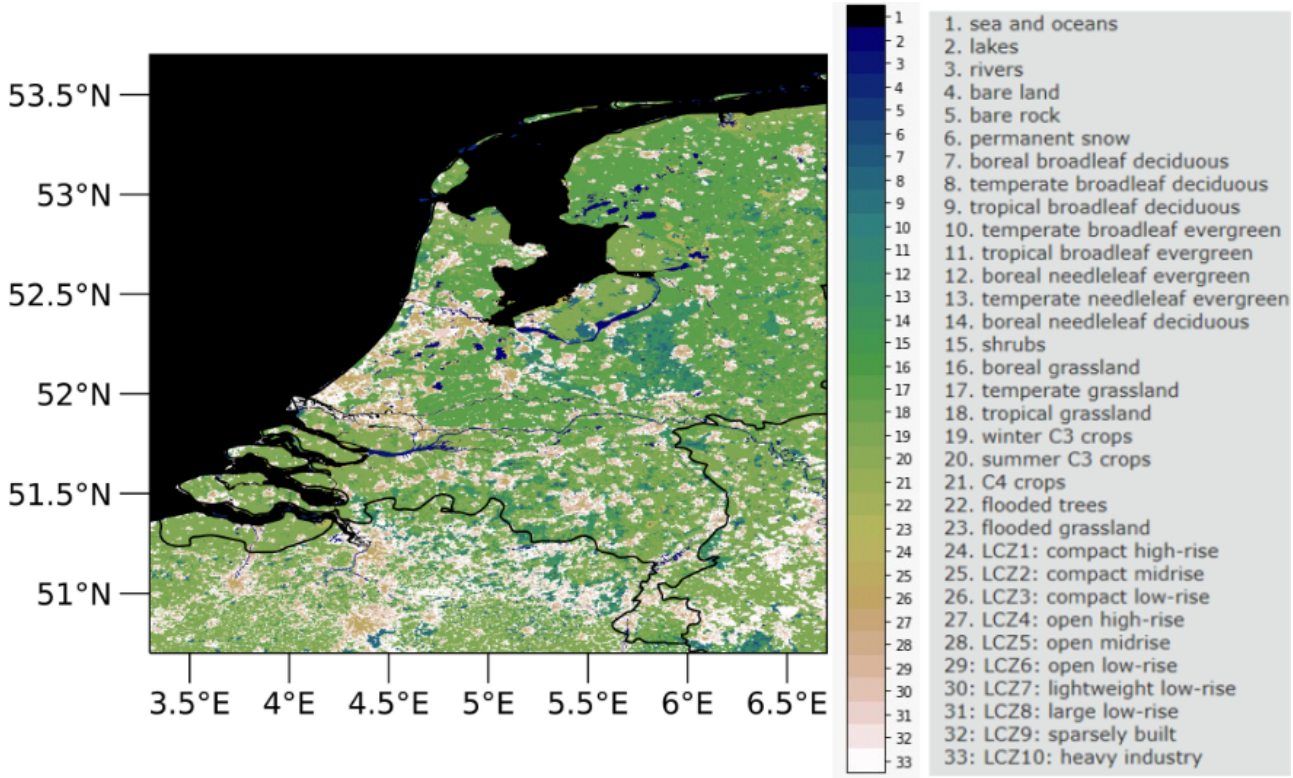

Figure 2.2: An illustration of the ECOCLIMAP-SG binary cover map called `ecosg_final_map.dir` for the Netherlands. A global 300m resolution grid is developed, where each cell is assigned a cover type and explained in the color bar and the legend on the right (CNRM, 2018). The essential surface parameters are supplied by SURFEX and other ECOCLIMAP-SG files, for example for defining the leaf area index and albedos. Number 1 corresponds to sea, number 2 and 3 to inland water, numbers 4 until 23 to nature, and numbers 24 until 33 to town.

All vegetation types are distinguished by properties provided in physiographic data files, such as assumed vegetation height (`HT`), visible and near-infrared albedos (`ALBVIS`, `ALBNIR`), and leaf-area index (`LAI`) depending on its cover type provided by the cover map. These essential surface parameters are supplied in the physiographic data (`PGD`) step.

Numerous surface schemes are available for selection. The current operational HCLIM model default surface schemes include ISBA (Interaction Soil Biosphere Atmosphere) for the nature tiles (Boone et al., 1999), SEAFLX for the sea tiles, TEB (Town Energy Balance) for the town tile (Masson, 2000), and FLake for the inland water tile (Mironov et al., 2003).

2.2.2. The gridded GlobalLakeDatabase

The global gridded lake data set named GlobalLakeDatabase provides both meta-information on the existence of lakes as well as the depth of lakes (Kourzeneva et al., 2012). The resolution is established at 30 arcseconds, which is approximately equivalent to 1 kilometer. Two primary binary files constitute the database: `GlobalLakeStatus_V3.0.dir` and `GlobalLakeDepth_V3.0.dir`.

The former file denotes the current status of data concerning the available information on the lake depth for each grid point. The latter indicates the assigned depth value for a grid point, measured in decimeters, if the data is available. Table 2.1 elaborates on the coded values assigned as lake depth meta-information. The reason for these various status values, some of them appearing non-logical like 1, is due to the usage of several different input files. This is explained in the next section 2.3. The two maps are plotted for the Netherlands in figure 2.3.

Table 2.1: A gridded value of the status of the information about lake depth within the `GlobalLakeStatus_V3.0.dir` file of the GlobalLakeDatabase

0	No inland water
1	No recognization of a lake: set default to 10 meters
2	Lake is recognized without lake depth: set default to 10 meters
3	Lake is recognized and real depth is used
4	A river is recognized: set default value of 3 meter

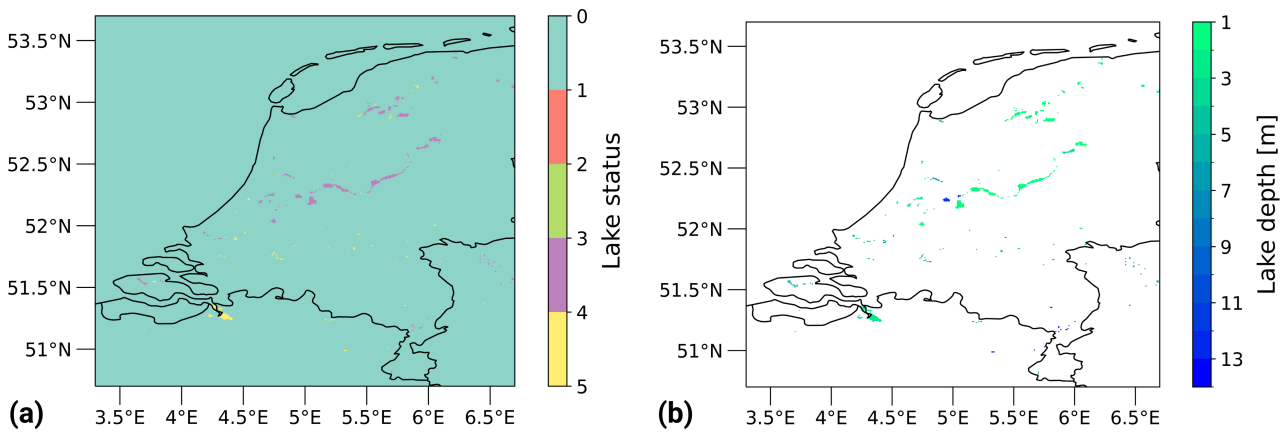

Figure 2.3: A representation of the GlobalLakeDatabase with (a) `GlobalLakeStatus_V3.0.dir`, indicating the meta-information corresponding to the lake depth file as shown in table 2.1, and (b) `GlobalLakeDepth_V3.0.dir` indicating the lake depths. The spatial resolution is about 1 km.

2.3. SURFEX workflow within HCLIM

Various steps within the HCLIM system must be completed to execute the SURFEX model. SURFEX is directly coupled to the HCLIM system through 3 steps: `PGD`, `PREP`, and `RUN`. An overview of the SURFEX workflow is presented in figure 2.4. The `PGD` step is integrated within a suite of subroutines housed under the `MakeCycleInput` module of the HCLIM framework, which oversees the preparation of climate files, boundaries, and observations. Within the preparation of climate files `Climate`, the physiographic data step (`PGD`) is launched.

Physiographic data (`PGD`) step

During the `PGD` step, the physiographic files required to execute the SURFEX model are imported into the system. Here, the surface land-cover physiography database named ECOCLIMAP-SG is loaded, as described in section 2.2.1. In case an inland water tile is assigned, files of the GlobalLakeDatabase provide the lake depth and other optical quantities. In one of the subroutines called `treat_global_lake_depth.F90` a consistency check between the cover files and the lake files takes place. If both grid points exhibit either the presence or absence of a lake, then no consequential action is taken, and the status and depth information from the lake files are utilized.

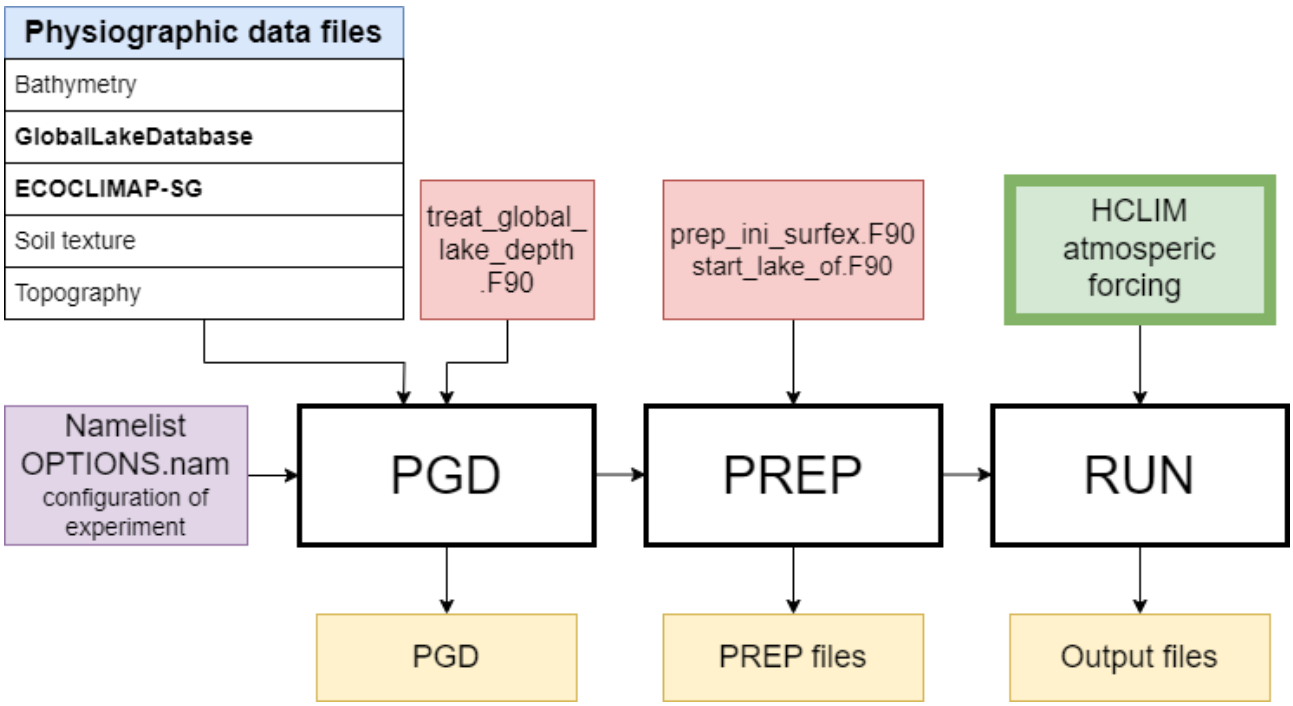

Figure 2.4: An illustration of the steps composing the SURFEX model: `PGD`, `PREP` and `RUN`. In a name list, the configuration for the experiment is set. During the `PGD` step the physiographic data files are loaded, resulting in static field `PGD` output files. Also, the existence and consistency of lakes are checked with the subroutine `treat_global_lake_depth.F90`. In the PREP step, the initial condition files for FLake are defined with `prep_ini_surfex.F90` and `start_lake_of.F90`. In the `RUN` mode, the SURFEX model is directly coupled to HCLIM through atmospheric forcing. The SURFEX output files are returned to HCLIM for further forecasting. Designed by author after SURFEX course material (CNRM, 2023)

In cases where `ecosg_final_map.dir` reads a lake but `GlobalLakeStatus_V3.0.dir` does not, a standard value of 10 meters deep is assigned. If `GlobalLakeStatus_V3.0.dir` indicates a lake, but `ecosg_final_map.dir` does not, the depth is set to zero. Hence, the `ecosg_final_map.dir` has priority over `GlobalLakeStatus_V3.0.dir`. Besides that, the surface schemes and model grids are defined.

`PREP` **step**

In the preparation step (`PREP`) prognostic variables are described and fields are again interpolated, yielding an initial SURFEX state. The subroutine `prep_ini_SURFEX.F90` prepares the initial SURFEX state runs. Specifically regarding the lake initialization, a file for cold start climatological means `Lake_LTA_New.nc` is called, which will be further explained later in section 2.5. Through another subroutine, `start_lake_of.F90`, the initial lake variables are assigned for the given date, the given grid box of the atmospheric model grid in lon-lat, and the given lake depth.

`RUN` **step**

After the `PGD` and `PREP` step, the SURFEX model can move forward to `RUN` mode. In the case of HCLIM, where SURFEX is directly coupled with atmospheric forcing fluxes, SURFEX runs as described and illustrated in figure 2.1. For the further time evolution of a specific inland water tile (lake and rivers), the freshwater lake model FLake model developed by Mironov et al. (2003) is used.

2.4. The fresh water lake model FLake

FLake, short for freshwater lake model, is a two-layer parameterization of the time-dependent vertical temperature profile in the water column and the integral energy budgets within these layers, such as the heat budget of the total water column and the mixed layer. It has been implemented in multiple weather forecast models (Mironov, 2008; Mironov et al., 2009), and also in HIRLAM (Kourzevena et al., 2008). The lake thermocline is the structure between the bottom edge of the mixed layer ($h(t)$) and the lake bottom (D). The thermocline is defined based on the concept of self-similarity of the temperature-depth curve, which assumes a certain shape through a shape factor (C_θ). FLake defines the temperature as θ, not to be confused with potential temperature for atmospheric applications.

The same approach is used for the description of the temperature structure of the thermally active upper layer of the bottom sediments and the ice/snow cover over the lake. The model FLake incorporates the essential physics, through the integration of the heat budgets for different circumstances, but remains computationally efficient. This makes it an appropriate model for operational weather forecasting purposes. A system of ODEs describes the evolution of the time-depending quantities. These are the mixed-layer temperature (θ_{wml}) and its depth ($h(t)$), the temperature (θ_b) at the water-bottom sediment interface, the shape factor (C_θ) for the temperature profile in the thermocline, the temperature (θ_H) at the lower boundary of the upper layer of bottom sediments penetrated by the thermal wave, and the depth ($H(t)$) below the lower boundary of this upper layer (see figure 2.5). The time-depending quantities are related to each other and the mean temperature of the water column $\bar{\theta}$.

For freshwater a quadratic equation of state for its density in terms of the temperature θ is utilized.

$$\rho_w = \rho_r(1 - \frac{1}{2}\alpha_\theta(\theta - \theta_r)^2), \tag{2.1}$$

where ρ_w is the water density, ρ_r = 999.98 kg /m^3 the maximum density of water at the temperature of θ_r = 277.13 K and a_θ = 1.6509·10^{-5}K^{-2} is an empirical thermal expansion coefficient. The buoyancy parameter β and a_θ both depend on the water temperature θ.

$$\beta(\theta) = g\alpha_t(\theta) = g\alpha_t(\theta - \theta_r), \tag{2.2}$$

where g= 9.81 ms^{-2} is the acceleration of gravity. Now the following two-layer parametrization representation of the evolution of the temperature profile, developed by Kitaygorodskiy and Miropolskiy Kitaigorodskii and Miropolsky in 1970, is adopted.

$$\theta = \begin{cases} \theta_{\text{wml}} & 0 \le z \le h \\ \theta_{\text{wml}} - (\theta_{\text{wml}} - \theta_b)\Phi_\theta(\zeta) & h \le z \le D \end{cases} \tag{2.3}$$

Here, $\Phi_\theta = [\theta_{\text{wml}}(t) - \theta(z,t)]/[\theta_{\text{wml}}(t) - \theta_b(t)]$ is a dimensionless function of a dimensionless depth $\zeta = [z - h(t)]/[D - h(t)]$. Thus, the thermocline extends from the basin bottom D to the outer edge of the mixed layer h.

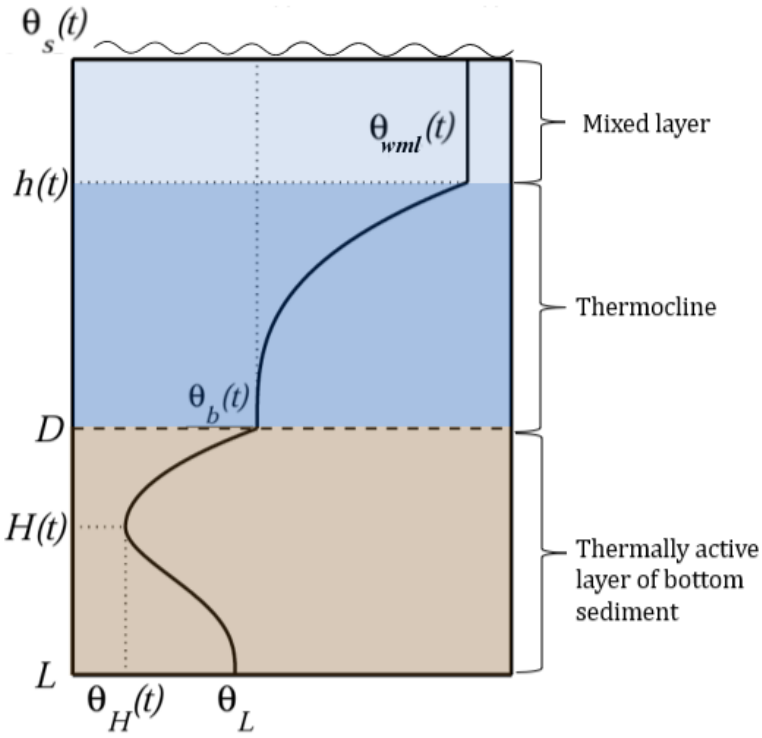

Figure 2.5: A schematic figure on how the temperature profile evolves in the mixed layer, the thermocline, and the thermally active layer of bottom sediments. The temperature profile is expressed by the mixed-layer temperature (θ_{wml}) and its depth ($h(t)$), the temperature (θ_b) at the water-bottom sediment interface, the shape factor (C_θ) for the temperature profile in the thermocline, the temperature (θ_H) at the lower boundary of the upper layer of bottom sediments penetrated by the thermal wave, and the depth ($H(t)$) below the lower boundary of this upper layer. The temperature θ_L at the outer edge z = L of the thermally active layer of bottom sediments is constant (Albergel et al., 2018)

The parameterization of the temperature profile should obey the heat equation. According to the parametrization, h, D, θ_{wml} , θ_b and the mean temperature of the water column, $\bar{\theta} = D^{-1}\int_0^D \theta dz$, are connected through:

$$\bar{\theta} = \theta - C_\theta \left(1 - \frac{h}{D}\right)(\theta_{\text{wml}} - \theta_b), \tag{2.4}$$

where the shape factor C_θ w.r.t. the temperature profile is $C_\theta = \int_0^1 \Phi_\theta(\zeta) d\zeta$.

Integration of the heat budget over the water column from z=0 to z=D yields an equation for the time evolution of the mean temperature $\bar{\theta}(t)$:

$$D\frac{d\bar{\theta}}{dt} = \frac{1}{\rho_w c_w}[Q_s + I_s - Q_b - I(D)], \tag{2.5}$$

where c_w =4.2·10^3 Jkg^{-1}K^{-1} is the specific heat of water. Q_s is the vertical heat flux at the lake surface, a sum of the sensible and latent heat fluxes and the net heat flux due to longwave radiation at the air-water interface. I_s is the heat flux due to solar radiation at the lake surface, obtained by multiplying the incident solar radiation flux from the atmosphere by 1 - a_w, where a_w is the albedo. Lastly, Q_b is the heat flux through the bottom.

Next, integrating the heat transfer equation over the mixed layer yields an equation for the mixed-layer temperature $\theta_{\text{wml}}(t)$.

$$H\frac{d\theta_{\text{wml}}}{dt} = \frac{1}{\rho_w c_w}[Q_s + I_s - Q_h - I(h)], \tag{2.6}$$

where all values are as previously explained, except for Q_h and $I(h)$, which represent the heat flux at the mixed-layer-thermocline interface.

The lake model is much more extensive, and the ordinary differential equations are extended by some algebraic equations for diagnostic quantities, such as the heat fluxes through the lake bottom and the ice-snow layer. In general, the model is forced by incident radiation surface fluxes and also entails many empirically estimated parameters and thermodynamic parameters. The required lake-specific parameters are the lake depth, the depth of the thermally active layer of bottom sediments, and the temperature at this depth. The first one is provided by the Global-LakeDatabase and the others are chosen by default. The model finally predicts the water's surface temperature, which will affect the surface-atmosphere heat fluxes and radiation. Since inland waters are part of the surface tiles, these fluxes are used in the weighted average of the grid boxes, as visualized in figure 2.1.

2.5. Initalization of FLake variables in lakes

The climatological means for the FLake model described in section 2.4 are given in a lake initialization file called `Lake_LTA_New.nc`. In the remainder, we will refer to the temperature with the symbol T (and not θ), unless stated otherwise. Similarly, the climatological means are provided at a temporal resolution and exist for the following FLake variables: bottom temperature (T_{bot}), mixed layer temperature (T_{wml}), mean water temperature (T_{mnw}), the lake surface temperature (T_{sfc}), the mixed layer height (h), the boundary layer height (h_{bl}) and the shape factor of the thermocline (C_{T}). These values vary throughout each one-third of the month, and only for lake depths ranging from 1 to 12 meters. Spatially, they differ per specific latitude (60°to 90°N) and longitude (180°W to 180°E) of the location (the Arctics are left out), on a 1°resolution. Hence, the instant and local model output is very sensitive to the specific moment and locations of a newly created lake. Within the scope of this research, we focus on water areas in South Holland, which are typically around 2 meters deep (Gulati and Donk, 2002).

To get an appreciation of the data included in the file `Lake_LTA_New.nc`, figure 2.6 shows as an example the initial lake surface temperatures T_{sfc} of 2-meter deep lakes for the entire world and West-Europe, for the first 10 days of August on a 1°spatial resolution. Figure 2.7 presents the time-evolving climatological means for T_{wml} ,T_{mnw} , T_{bot} and T_{sfc} over a year in the middle of the Netherlands (52°N,5°E) and the southern province Limburg (51°N,6°E). Here, we observe that for a 2-meter lake, all temperatures obtain the same cold start temperature in the middle of the Netherlands. For the Limburg area, these are different and have a slightly lower value. For example, the difference is approximately 3 Kelvin in April.

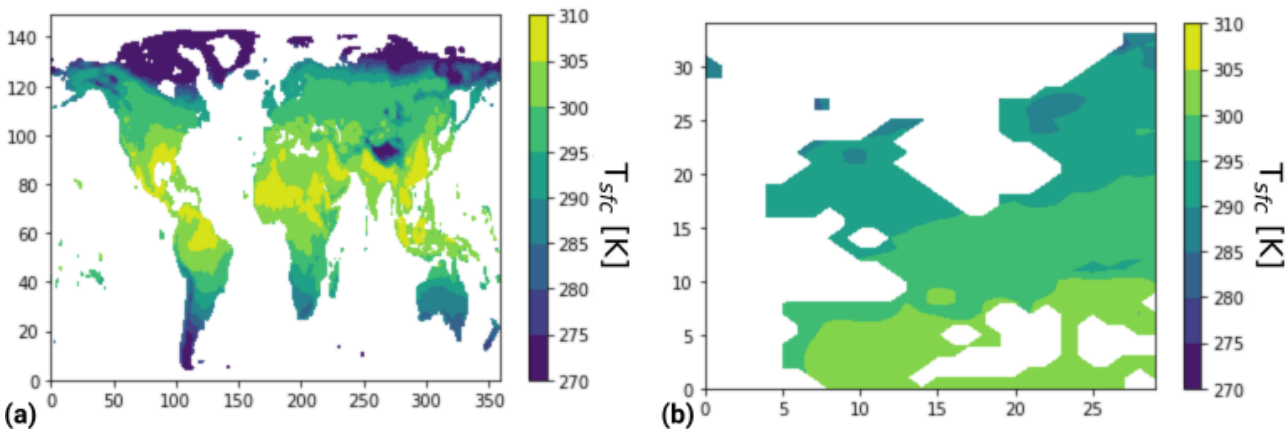

Figure 2.6: Climatological means from the `Lake_LTA_New.nc` map for a 2 meter deep lake. The lake surface temperature T_{sfc} for the first tertial of August is shown (a) on a global scale on a 1°resolution from latitude 60°S to 90°N) and longitude (-180°E, 180°W) and (b) zoomed in on West-Europe.

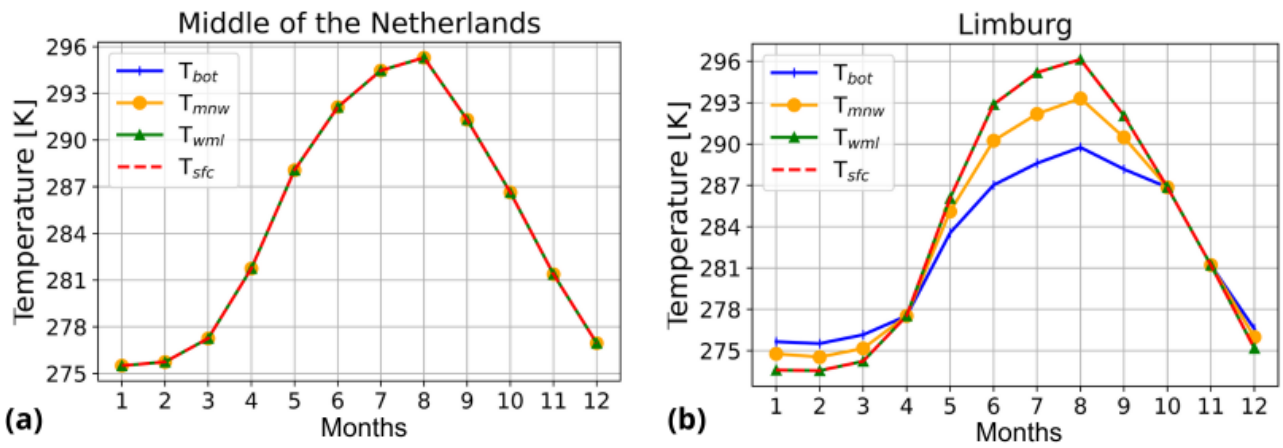

Figure 2.7: Climatological mean values from the `Lake_LTA_New.nc` file for the bottom temperature T_{bot} , the mean water column temperature T_{mnw} , the mixed layer temperature T_{wml} and lake surface temperature T_{sfc} over the year in (a) the middle of the Netherlands (52°N,5°E) and (b) the southern province Limburg (51°N,6°E) for a lake depth of 2 meters.

2.6. Fluxes in the convective boundary layer and at the surface

The atmospheric boundary layer (ABL) is the segment of the troposphere closest to the Earth's surface and is strongly influenced by surface conditions. The ABL typically exhibits a significant amount of turbulence, through wind shear and buoyancy forces.

When wind flows over surfaces like trees, buildings, and grass, it generates turbulence due to the contrast in wind speeds, known as wind shear. Alternatively, temperature can induce turbulence through buoyancy forces. In this case, warmer and less dense air rises while colder, denser air sinks due to gravity, creating a turbulent motion. Turbulence manifests as swirling patterns, often referred to as eddies. On a typical day with no severe weather, sunlight warms the surface, and turbulence is mainly driven by buoyancy. During the daytime, large-scale mixing occurs, leading to a turbulent mixing layer depth of around 1 to 2 kilometers, called the convective boundary layer (CBL).

However, during nighttime, as the surface cools, turbulence is usually suppressed by negative

buoyancy (stratification of the air), and turbulence is primarily driven by wind shear. This results in smaller eddies and a shallower surface mixing layer, typically around 100 to 200 meters in depth. To what extent the surface responds to heating, is dependent on the type of surface. Some surfaces may remain warmer due to significant heat storage from daytime heating, such as lakes. Because they retain warmth, they can act as sources of buoyancy forces. The adjacent air is heated by these warm surfaces, leading to rising warm air, which initiates circulation and generates weak turbulent motions. Surface heterogeneities can, therefore, induce highly localized turbulence. As such, land use changes will modify the local weather patterns.

During the night, the air in the lower few tens of meters in the atmosphere is mainly affected by local surface heterogeneities, inducing turbulent motions. These effects are of interest when studying changes in land use. In section 2.6.1 the governing equations for the heat budget, water budget, and the mixing will be discussed. In section 2.6.2, the surface energy balance is outlined, and its relation to typical surface properties and ground or lake fluxes, as described earlier by the FLake model (refer to section 2.4). Eventually, due to energy conservation, all energy budgets in the lower atmosphere and within the lake are directly related to each other.

2.6.1. Heat, water and momentum budgets

As the focus of this study is to assess the overall mean flow characteristics of heat, humidity, and momentum above various surface types, it is common practice to utilize time-averaged versions of the governing budget equations (Celik, 1999). After taking the time derivative of the conservation of budget equations and applying Reynolds averaging techniques, we arrive at Reynolds-averaged forms of the heat, water, and momentum conservation equations. Here, the large-scale advection and turbulent transport on the mean properties of air are split. Also, incompressibility of property fluctuations and horizontal homogeneity are assumed.

For the heat budget equation, this reduces to equation 2.7.

$$\underbrace{\frac{\partial \overline{T}}{\partial t}}_{\text{local T change}} + \underbrace{\overline{u}\frac{\partial \overline{T}}{\partial x} + \overline{v}\frac{\partial \overline{T}}{\partial y} + \overline{w}\frac{\partial \overline{T}}{\partial z}}_{\text{advection}} = \underbrace{-\overline{w}\frac{g}{c_p}}_{\text{enthalpy}} - \underbrace{\frac{1}{\overline{\rho} c_p}\frac{\partial \overline{F_{rad}}}{\partial z}}_{\text{radiation}} - \underbrace{\frac{L_p}{c_p}\overline{E}}_{\text{latent heating}} - \underbrace{\frac{\partial \overline{w'T'}}{\partial z}}_{\text{turbulence}} \tag{2.7}$$

Here, the first term on the left-hand side is the time-dependent mean temperature and the next three terms are the horizontal and vertical advection, giving the change of the temperature of the air due to transportation by the wind. On the right, the first term states potential energy gz due to an increase in height must be balanced by enthalpy $c_p T$. The second term describes adding energy in the form of radiation. L_p the latent heat release associated to phase change $E = \partial q_v / \partial t$, such as increase of q_v by evaporation of rain. The last term describes the transport of heat due to turbulent eddies.

The Reynolds averaged time-evolving specific humidity is given by equation 2.8.

$$\underbrace{\frac{\partial \overline{q_v}}{\partial t}}_{\text{local } q_\mathrm{v} \text{ change}} + \underbrace{\overline{u}\frac{\partial q_v}{\partial x} + \overline{v}\frac{\partial q_v}{\partial y} + \overline{w}\frac{\partial q_v}{\partial z}}_{\text{advection}} = -\underbrace{\frac{\partial \overline{w' q_v'}}{\partial z}}_{\text{turbulence}} + \underbrace{S_{q,t}}_{\text{source}}, \tag{2.8}$$

where the first term describes the time-dependent mean specific humidity and the next three terms again the horizontal and vertical advection. On the right-hand side, the first term repre-

sents the turbulent eddies due to vertical fluxes. The source term $S_{q,t}$ describes processes like evaporation and condensation.

The Reynolds averaged horizontal momentum budgets are given by equations 2.9a and 2.9b.

$$\underbrace{\frac{\partial \overline{u}}{\partial t}}_{\text{local acceleration}} + \underbrace{\overline{u}\frac{\partial \overline{u}}{\partial x} + \overline{v}\frac{\partial \overline{u}}{\partial y} + \overline{w}\frac{\partial \overline{u}}{\partial z}}_{\text{advection}} = \underbrace{f\overline{v}}_{\text{Coriolis}} - \underbrace{\frac{1}{\overline{\rho}}\frac{\partial \overline{p}}{\partial x}}_{\text{pressure}} - \underbrace{\frac{\partial \overline{u'w'}}{\partial z}}_{\text{turbulence}}, \tag{2.9a}$$

$$\underbrace{\frac{\partial \overline{v}}{\partial t}}_{\text{local acceleration}} + \underbrace{\overline{u}\frac{\partial \overline{v}}{\partial x} + \overline{v}\frac{\partial \overline{v}}{\partial y} + \overline{w}\frac{\partial \overline{v}}{\partial z}}_{\text{advection}} = \underbrace{-f\overline{u}}_{\text{Coriolis}} - \underbrace{\frac{1}{\overline{\rho}}\frac{\partial \overline{p}}{\partial y}}_{\text{pressure}} - \underbrace{\frac{\partial \overline{v'w'}}{\partial z}}_{\text{turbulence}}. \tag{2.9b}$$

The advection term accounts for the alteration in a parcel of air's characteristics caused by wind-induced transport. The pressure gradient force encompasses the horizontal pressure gradient divided by the air density, depicting the force generated by pressure variations across a surface. The Coriolis term characterizes the impact of the Earth's rotation.

2.6.2. The surface energy balance (SEB)

An overview of all processes near the surface-atmosphere interface, incorporated in SURFEX, is provided in figure 2.8.

Directly at the surface $z = 0$, the surface energy balance is determined by the net fluxes of solar radiation (SW), infrared radiation (LW) and the turbulent fluxes for evaporation of moisture and heat, respectively latent heat flux (LHF) and sensible heat flux (SHF), and G is the ground heat flux (Garratt, 1992). These elements add up to:

$$SW_{net} + LW_{net} - G = SHF + LHF \tag{2.10}$$

All mentioned variables are expressed in Wm^{-2}. The CO^2 levels, chemical species, and aerosols play an inherent role in the netto radiation, present under surface fluxes in figure 2.8.

The Bowen ratio describes the relative moistening (LHF) or heating (SHF) of the turbulent fluxes, expressed through the formal definition of the fluxes of heat and moisture, $\overline{w'T_{\mathrm{sfc}}'}$ and $\overline{w'q_{\mathrm{v}}'}$ respectively, following from Reynolds decomposition:

$$B = \frac{SHF}{LHF} = \frac{\rho c_p \overline{w'T_{\mathrm{sfc}}'}}{\rho L_v \overline{w'q_v'}} \tag{2.11}$$

Wetlands have strong evaporation levels, hence a large LHF, decreasing the Bowen ratio. A dry and hot area, which is moisture-free, will typically have a higher SHF and lower LHF for the same radiative forcing. If the LHF reaches near zero, the Bowen ratio could become infinite in a desert.

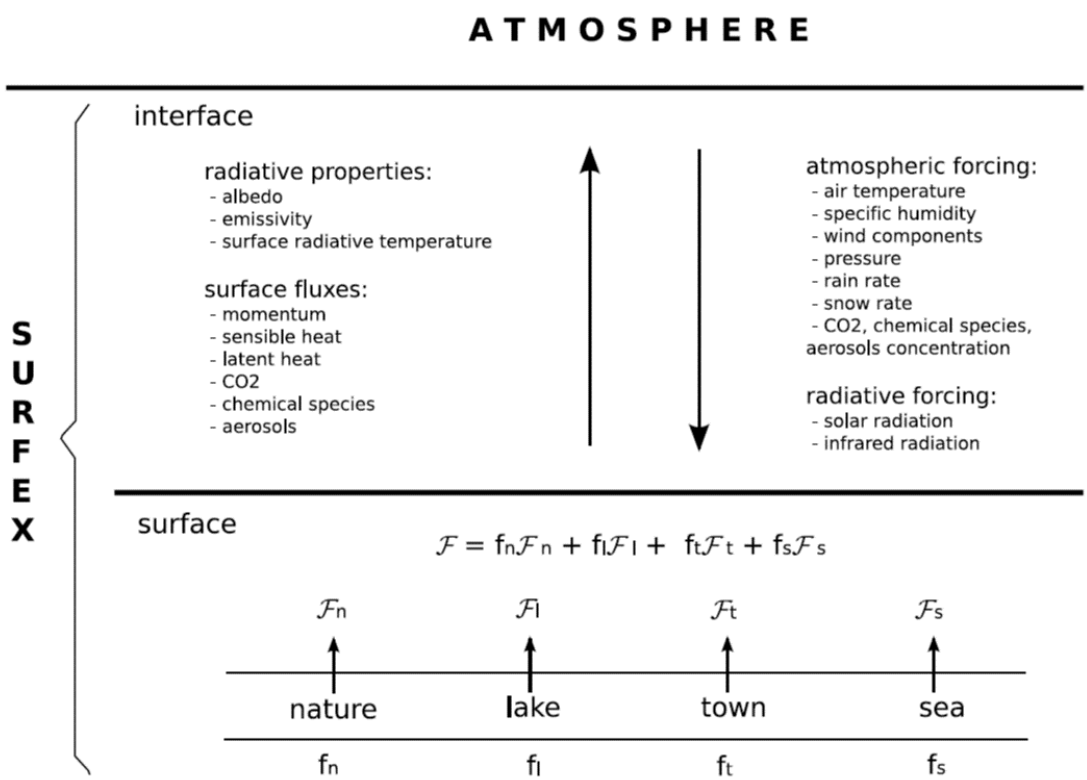

Figure 2.8: A schematic of the phenomena interacting at the surface-atmosphere interface of the SURFEX model, which is directly coupled to the HARMONIE-Climate model. At the surface, the contribution of tiles of the SURFEX model (nature, lake, town, and sea) are averaged over a grid box. The radiative properties of the surface and the fluxes from the surface, contribute to the near-surface atmospheric variables. Conversely, the atmosphere forces the SURFEX model through radiative and atmospheric forcing. Adopted from SURFEX course material (CNRM, 2023)

.

At the soil-atmosphere interface, the SHF and LHF are calculated by the following expressions,

$$LHF = \frac{\rho L_v}{r_{\mathrm{aV}} + r_s}(q_{\mathrm{sat}}\,(T_{\mathrm{sfc}}) - q_{v_{\mathrm{atm}}}), \tag{2.12}$$

and

$$SHF = \frac{\rho c_p}{r_{\mathrm{aH}}}(T_{\mathrm{sfc}} - T_{\mathrm{atm}}). \tag{2.13}$$

Here, ρ is the density of air in g m^{-3}, $L_v = 2.5 \cdot 10^6$ J kg^{-1} is the latent heat of vaporization of water, r_{aV} denotes the aerodynamic resistance to latent exchange, r_{s} is the surface resistance, q_{sat} represents the saturated specific humidity of water vapor, and $q_{\mathrm{v,atm}}$ is the atmospheric water vapor specific humidity. c_p stands for the specific heat capacity of air at constant pressure, and r_{aH} denotes the aerodynamic resistance to sensible heat flux. T_{sfc} and T_{atm} are the temperatures in Kelvin at the surface and in the atmosphere, respectively (Moene and Van Dam, 2014; Garratt, 1992).

The aerodynamic resistance that appears in equation 2.12 r_{aH} and r_{aV} are inversely related to the efficiency of the atmosphere to exchange water vapor and heat with the surface, defining the intensity of the turbulence. These are defined through:

$$r_{\mathrm{aV}} = \frac{1}{C_{\mathrm{E}}\, u_{\mathrm{atm}}}, \tag{2.14}$$

$$r_{\mathrm{aH}} = \frac{1}{C_{\mathrm{H}}\, u_{\mathrm{atm}}}. \tag{2.15}$$

Here, C_e and C_h are the turbulent exchange coefficients for water vapor and heat and u_{atm} is the mixed-layer wind speed at a certain height in the atmosphere (Garratt, 1992; Moene and Van Dam, 2014)

The surface resistance to evaporation r_{s} is dependent on vegetation and soil conditions, varying throughout forests, wetlands, and agricultural spaces. Both r_{veg} and r_{soil} are modeled with the Jarvis parametrization, which is an extensive set of equations and is also employed in the SURFEX model and IFS (ECMWF, 2010). For further understanding, the dependencies of r_{veg} on other functions will be outlined here.

The vegetation resistance is defined as:

$$r_{\mathrm{veg}} = \frac{r_{\mathrm{s,min}}}{LAI} F_1(SW_{\mathrm{dn}})F_2(w_{\mathrm{soil}})F_3(VPD)F_4(T), \tag{2.16}$$

With $r_{\mathrm{s,min}}$ the minimum surface resistance, LAI the leaf area index of the vegetation, F_1 correcting for the downward shortwave radiation SW_{dn} , F_2 a function depending on soil moisture w_{soil} , F_3 as a function depending on the water vapor pressure deficit (VPD) and F_4 a function depending on the temperature T (van Heerwaarden, 2011).

The soil resistance r_{soil} depends on the amount of soil moisture in the upper layer, through

$$r_{\mathrm{soil}} = r_{\mathrm{s,min}}\, F_2(w_{\mathrm{soil}}) \tag{2.17}$$

The total LHF consists of three separate components. There is transpiration from vegetation, soil evaporation, and direct evaporation from liquid water, either from interception or dew water. Therefore, each cover type holds unique constants for $r_{\mathrm{s,min}}$, LAI, and capacities to hold moisture. These elements lead to differences in the latent heat flux. r_{veg} is large for dry soil (reduced evaporation) and reaches zero for saturated conditions, such as lakes (maximum evaporation).

As mentioned discussing the Bowen ratio, the atmospheric temperature T_{atm} and specific humidity q_{v} are directly dependent on the turbulent fluxes according to:

$$SHF = \rho c_p \overline{w' T'_{\mathrm{sfc}}} \tag{2.18a}$$

$$LHF = \rho L_v \overline{w' q_{\mathrm{v}}{}'_{\mathrm{sfc}}} \tag{2.18b}$$

Next to turbulent heat and evaporation fluxes, turbulent momentum fluxes have a friction effect on the mean horizontal wind. When horizontal gradients of the fluxes vanish, and the horizontal wind speed approaches zero over the surface ($u_{\mathrm{sfc}} \to 0$), as typically occurs during nighttime, the momentum turbulent fluxes are expressed by:

$$\overline{u' w'_{\mathrm{sfc}}} = -C_d \left|U_{\mathrm{spd,atm}}\right| u_{\mathrm{atm}}, \tag{2.19a}$$

$$\overline{v' w'_{\mathrm{sfc}}} = -C_d \left|U_{\mathrm{spd,atm}}\right| v_{\mathrm{atm}}. \tag{2.19b}$$

2.6.3. Radiative fluxes

Shortwave radiation refers to the incoming solar radiation, which is the primary source of energy for the Earth's climate system. The solar radiation received at the outer atmosphere of the Earth

defines the solar constant, which is approximately 1361 Wm^{-2}. As solar radiation travels through the atmosphere to the surface, it is attenuated by the atmospheric composition of gases, aerosols, and cloud droplets.

Some of the incoming SW radiation is reflected directly by the Earth's surface, depending on surface properties such as the albedo. The albedo is calculated through $R = SW_{\mathrm{up}} / SW_{\mathrm{dn}}$. For example, water areas have a smaller albedo than grasslands of respectively 0.06 and 0.24 (Moene and Van Dam, 2014).

Upwelling longwave radiation LW_{up} is related to the surface temperature by the surface emissivity ϵ and the Stefan-Boltzmann constant σ through $LW_{\mathrm{up}} = \epsilon\sigma T_{\mathrm{sfc}}{}^{4}$. Downwelling longwave radiation LW_{dn} is due to reflection of LW_{up} by interacting with molecules in the atmosphere, such as water vapor, carbon dioxide, and methane. The surface emits more longwave radiation than it absorbs, yielding a negative LW_{net}.

Clouds not only reflect shortwave radiation but also emit longwave radiation to Earth's surface, contributing to the Greenhouse effect.

3

Comparing HCLIM model results with weather stations observations

HCLIM has a relatively high spatial and temporal resolution compared to other climate and NWP models, enabling it to study the impacts of the urban environment on local atmospheric properties like temperature. As birds are the linking pins between the urban and rural environments, attracted to the human resources in urban areas, climatology studies in these areas will become more important. It is therefore important to get a grip on potential biases in the model results as inferred from a comparison with observations and pinpoint the risks of misinterpreting either one of them. To this end, a study on the local weather observations in and around the city of Rotterdam is performed. This is approached by comparing model results to weather station observations, to gain insight into the heterogeneity.

For the weather station observations we distinguish (1) TU Delft weather stations in Rotterdam and (2) KNMI automatic weather stations. We compare two weather types, a mid-august heatwave in 2020 and a regular Dutch summer period in 2021, for the same dates 5-8 till 18-8. To assess the urban-rural differences in model results and observations, comparisons are also made for the Cabauw research observation tower of the KNMI, situated in Lopik and surrounded by kilometers of grassland.

For the variables, a current focus lies on the temperature and humidity levels, as the wind speeds measurement and model height differ up to 8 m in the vertical.

3.1. Data sources, experimental set-up and processing methods

3.1.1. TU Delft weather stations in Rotterdam

The observational weather station data is obtained through 9 different weather stations placed all over the city of Rotterdam (`https://weather.tudelft.nl`). Pictures of the exact locations of these stations are shown in figure C.2. The 'Heijplaat' station is omitted, as it was non-active during the studied years.

The weather stations are placed in Rotterdam foremost to measure rainfall within the city, but also measure regular weather variables with a time step of 5 minutes. For the validation, the averaged temperature T_{atm} [K] and specific humidity q_{v} [g/kg] are compared.

The measurements are done at the height of the station installation. The exact height is unknown, but deriving the height from the pictures indicates a 1 to 3-meter height (figure C.2).

The temperature is directly observed and real-time available averaged over 5 minutes. The specific humidity is calculated by using equation D.11. As the air pressure is not directly measured, the observed air pressure p of the nearby KNMI station in Rotterdam 'Airport' is used, which is traced to sea level during observations. The saturation vapor pressure is directly observed e_{sat}. With these inputs, the specific humidity q_{v} can be calculated. The formal definitions and approximations to calculate the specific humidity are provided in Appendix D.

To compare the data with the other sources, a rolling mean creates hourly averages.

3.1.2. KNMI automatic weather stations

Throughout the Netherlands 48 KNMI weather stations are placed, of which 14 are located offshore. The KNMI weather stations measure variables like air temperature (at 1.5 m), relative humidity, air pressure, wind velocity and direction, precipitation, presence of clouds, and radiation. Via an online data platform, the KNMI makes the hourly data publicly available to download for each station (`https://www.daggegevens.knmi.nl/klimatologie/uurgegevens`). The data obtained from this platform consists of hourly measurements.

The temperature is directly observed at 1.5 m height. The specific humidity is obtained through two steps. First, the saturation vapor pressure e_{sat} is calculated through equation (D.8). With e_{sat}, the saturated specific humidity q_{sat} can be calculated with the observed temperature T and air pressure p as input for equation (D.9). Finally, the specific humidity is approximated by multiplying q_{sat} with the observed relative humidity RH (D.11).

Station	**Latitude**	**Longitude**	**ECOCLIMAP-SG value**	**Tile type**	**Location**
Bolnes	51.89819	4.55184	26: compact low	Urban	Grass, near house
Capelle	51.92746	4.58506	25: compact mid	Urban	+2m building
Delfshaven	51.90506	4.44618	25: compact mid	Urban	+2m building
Lansingerland	52.01035	4.5288	26: compact low	Urban	+2m building
Ommoord	51.95842	4.54745	25: compact mid	Urban	+2m building
Ridderkerk	51.87786	4.58512	32: sparsely built	Urban	Grass, near house
Oost	51.92530	4.54767	32: sparsely built	Urban	~2m building
Spaanse Polder	51.93245	4.41623	25: compact mid	Urban	~2m building
Airport	51.962	4.447	32: sparsely built	Urban/Nature	Open grass
Cabauw	51.970	4.926	17: grassland	Nature	Open grass

3.1.3. HCLIM model output

The data obtained through HCLIM are hourly averaged. The values are unlike the weather station point observations averaged over a grid cell, which are 2.5 km by 2.5 km by default, or manually increased to a higher resolution. The grid points are chosen by applying the nearest-neighbor method. The specific humidity q_{v} and atmospheric temperature T_{atm} are directly measured.

3.1.4. Experimental set-up

To study the aforementioned aspects two 13-day periods are analyzed. The period of 5th of August 2020 00:00 till the 18th of August 2020 00:00 is referred to as the heatwave and the period of 5th of

August 2021 00:00 till the 18th of August 2021 00:00 is referred to as regular summer. These extreme versus regular periods are chosen based on the seasonal summaries of the KNMI (KNMI, a).

3.2. Results

3.2.1. Temperature

First, we assess the diurnal cycle between modeled and observed temperatures. For this, a selection is made out of 4 stations, to have a mix of an urbanized and rural area, the location (on the grass or a building), and the cover type value (compact or sparsely built) from `ecosg_final_map.dir`. This selection entails the stations Ridderkerk (TUD, urban area, figures 3.1a, 3.3a), Spaanse Polder (TUD, urban area, figures 3.1b, 3.3b), Rotterdam Airport (KNMI, urban/nature area, figures 3.1c, 3.3c) and Cabauw (KNMI, nature area, figures 3.1d, 3.3d).

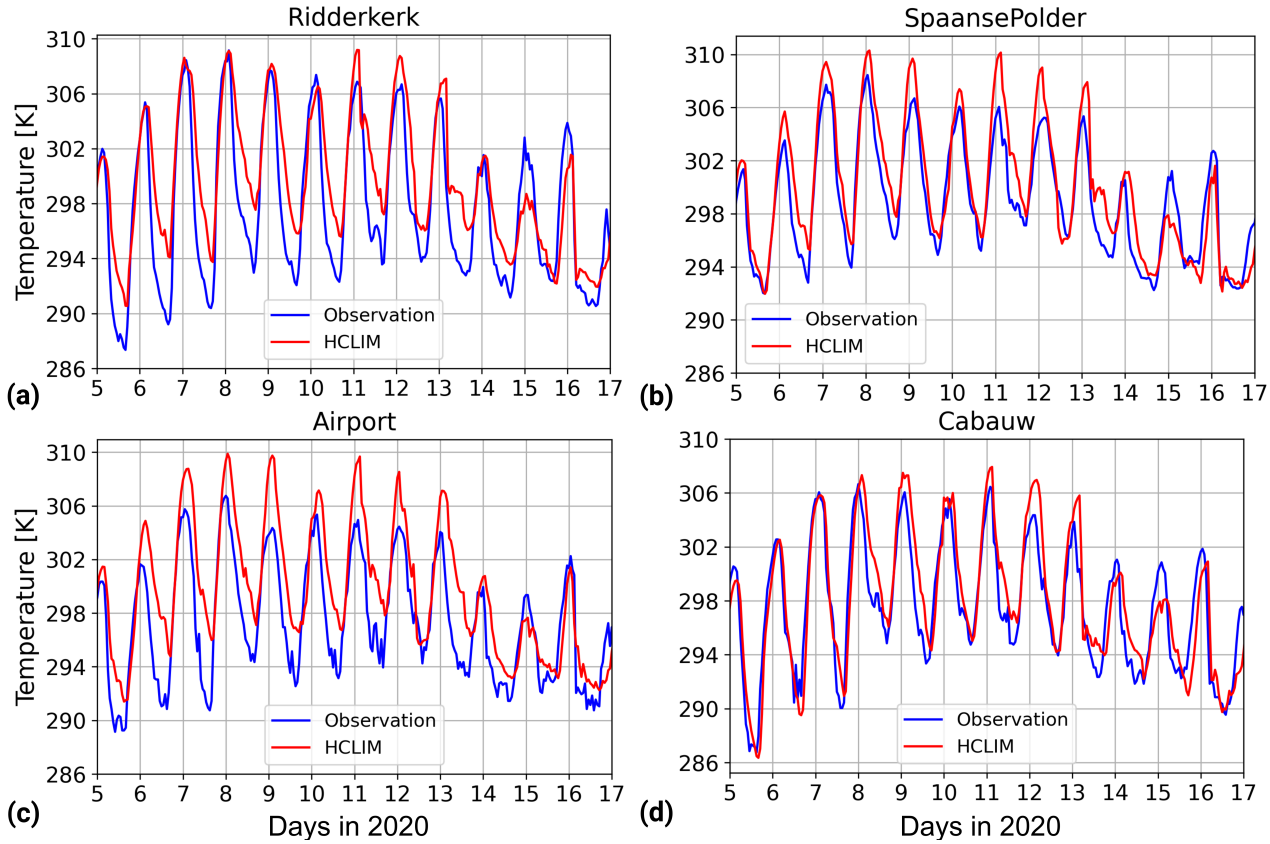

Figure 3.1: A comparison between the HCLIM model results (red) and observed weather station data (blue) for the temperature [K] for a heatwave period from 5-08-2020 till 18-08-2020 for (a) Ridderkerk, (b) Spaanse Polder (c) the Airport and (d) Cabauw.

Note the location of the day labels are at local noon (UTC+2).

For the year 2020, characterized by a heatwave, HCLIM overestimates the temperature during daytime. This is most clearly observed at Spaanse Polder (fig. 3.1b) and the Airport (fig. 3.1c). During the nighttime, this is pointed out mainly in Ridderkerk (fig. 3.1a) and the Airport (fig. 3.1c). At the Airport, a systematic positive bias of HCLIM is observed, also visible during the night. This might be attributed to the fact that at the Airport, the HCLIM model grid cell surface type consists of 55% urban and 45% nature tiles, while the station is actually located on open grass. This implies HCLIM calls predominantly the TEB surface scheme, while the weather station is placed on grassland, overestimating the temperatures. Also, an urban heat island effect is observed, shown

by figure 3.2 plotting the mean difference over the heatwave for all TU Delft stations compared to the Rottterdam Airport KNMI station, through $T_{\text{TUD}} - T_{\text{Airport}}$.

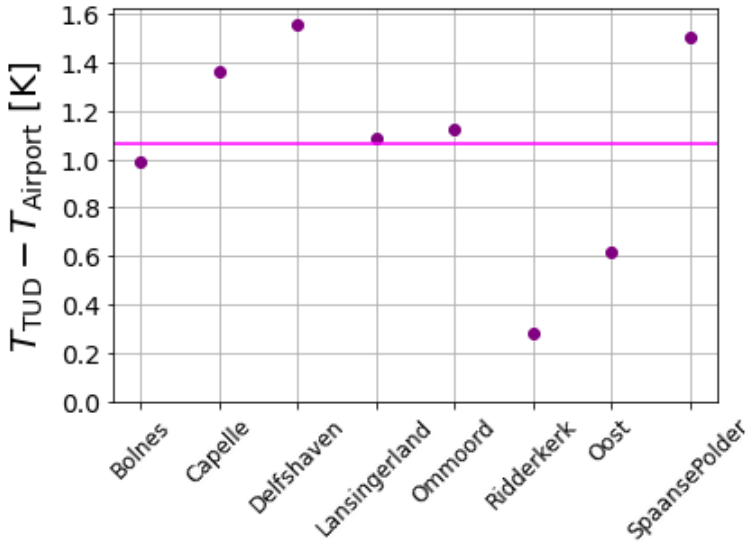

Figure 3.2: The mean difference over the heatwave for the TU Delft weather stations placed within Rotterdam compared to the KNMI station placed just outside Rotterdam at the Airport. The positive values indicate an urban heat island effect from 5-8-2020 till 18-8-2020 in the city of Rotterdam. The horizontal fuchsia-colored line indicates the mean difference averaged over all TUD stations.

The mean observed temperatures of the city-located TU Delft stations during the heatwave are on average 1.08 K higher than at the Airport. For station Delfshaven, centered in the city, the mean difference during the heatwave is up to 1.56 K.

Examining the temperature time series in the 2021 case reveals noticeable fluctuations over the course of days. Especially between 10 and 12 August 2021, the observations fluctuate more than the HCLIM model results do, as can be seen for Ridderkerk (fig. 3.3a) and the Airport (fig. 3.1c), showing up to 3 K lower values for the observations than HCLIM models. Also at the Cabauw station (fig. 3.1d) the HCLIM model results and observations differ by 2 K. The HCLIM averages over a grid cell and the observations are point-like. Combined with relative unpredictable weather compared to a heatwave, this makes it more difficult for the model output to match the actual observations and to interpret the results.

In figure 3.4a and 3.4b, the daily mean temperature differences between the HCLIM model output and the weather station observation are plotted for every station location for the heatwave in 2020 and the regular summer days in 2021. The difference is calculated by subtracting the observed temperature from the model temperature (HCLIM - observation), so a positive difference indicates a higher model result. The fuchsia-colored line indicates the daily mean difference across all TU Delft weather stations as compared to the HCLIM model results.

During the heatwave, we observe that HCLIM frequently overestimates the temperature, based on the daily mean differences. During the regular summer days, the daily mean differences lie closer to zero, indicating the HCLIM errors are averaged out over a period of a day, as the temperature time series are more fluctuating (as seen in figures 3.1 and 3.3). If we focus on specific stations, the clear outliers are Ridderkerk (brown), Airport (mustard), and quite often Oost (pink) and Spaanse Polder (grey) - both in 2020 and 2021. The first three are characterized by a sparsely built urban area. Cabauw (aqua) is the only weather station, which is not placed in an urban area. Even though

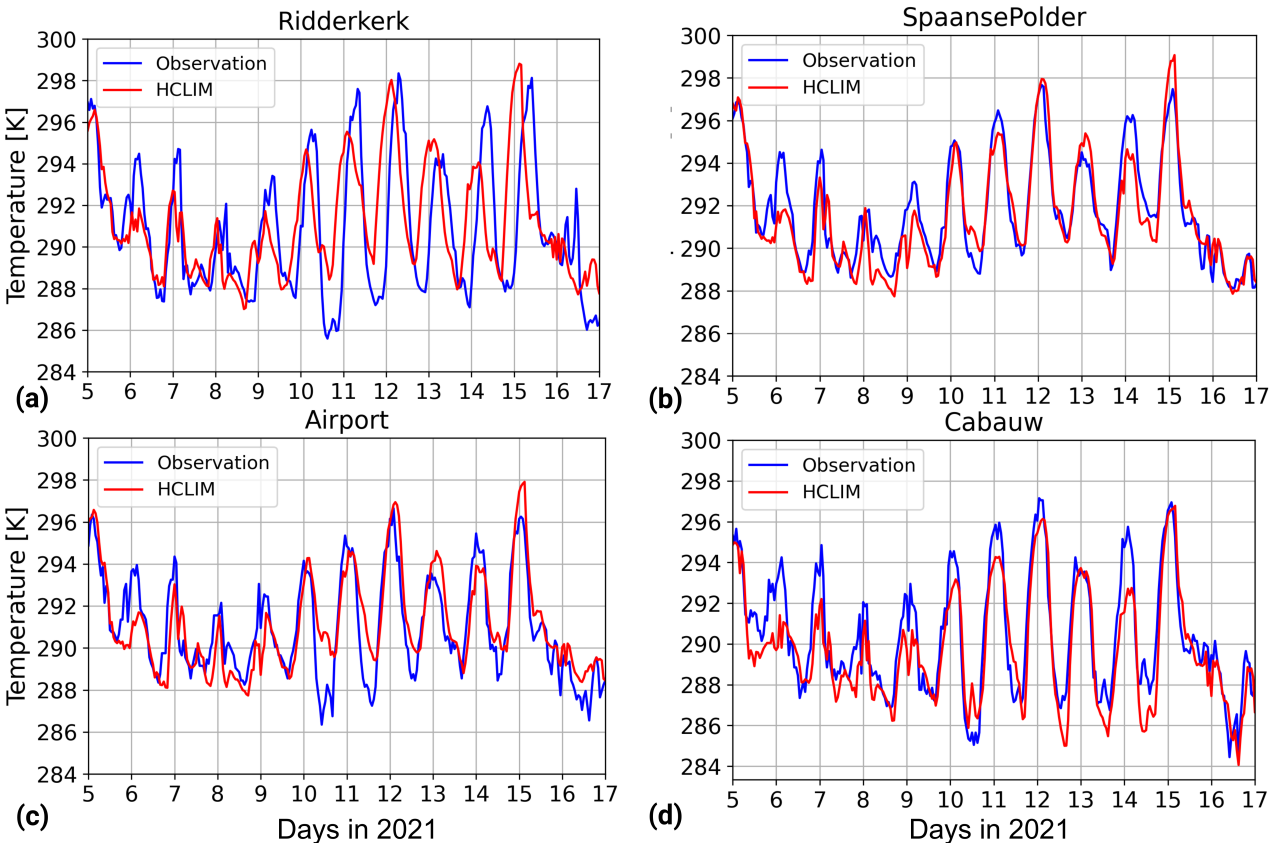

Figure 3.3: A comparison between the HCLIM model results (red) and observed weather station data (blue) for the temperature [K] from 5-08-2021 till 18-08-2021 for (a) Ridderkerk, (b) Spaanse Polder (c) the Airport and (d) and Cabauw.

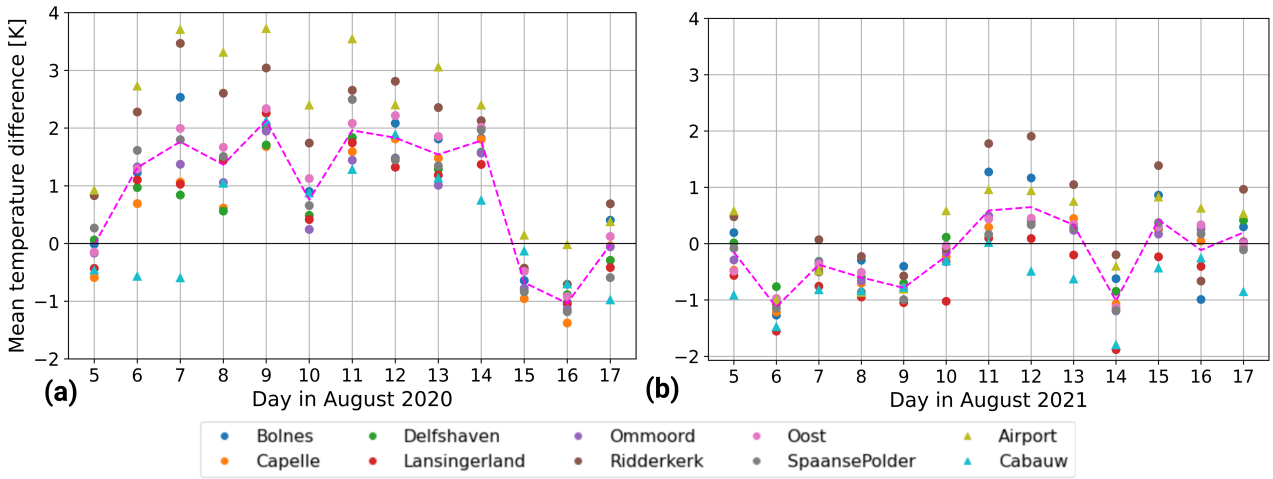

Figure 3.4: The daily mean difference between the HCLIM model results minus the observed weather station data for the temperature [K] from 5-08 till 18-08 during (a) a heatwave period in 2020 and (b) a regular summer period in 2021 for all TU Delft and KNMI weather stations. The fuchsia-colored line is the mean difference of HCLIM model results compared to only the TU Delft stations observations.

optically significant temperature differences are present, the time-mean difference is relatively close to zero, compared to the weather stations in more urbanized areas. These results indicate that HCLIM overestimates temperatures more often on sunny and hot summer days than it does on regular summer days.

3.2.2. Specific humidity

Another variable of interest is the specific humidity. A similar processing approach resulted in diurnal cycles of the specific humidities for the heatwave of 2020 and the regular summer period in 2021. Again, we analyze the same weather stations as for the temperature, namely, Ridderkerk (figures 3.5a, 3.6a), Spaanse Polder (figures 3.5b,3.6b), Airport (figures 3.5c,3.6c) and Cabauw (figures 3.5d, 3.6d).

In 2020, we observe that for Ridderkerk (fig. 3.5a), Spaanse Polder (fig. 3.5b), Airport (fig. 3.5c), HCLIM often underestimates q_v throughout the day and night. The effect of underestimation is substantially observed at Ridderkerk, for example with $\Delta q_v = 4.2$ [g/kg] on 09-08 around noon. For Spaanse Polder (fig. 3.5b), this effect is largest around noon, but the model results are in better agreement with the observations during the night. The HCLIM results for the Airport (fig. 3.5c) and especially Cabauw (fig. 3.5d), deviate less from station observations. This might indicate a better performance of HCLIM predicting the atmospheric water balance for more rural locations compared to urban-placed stations.

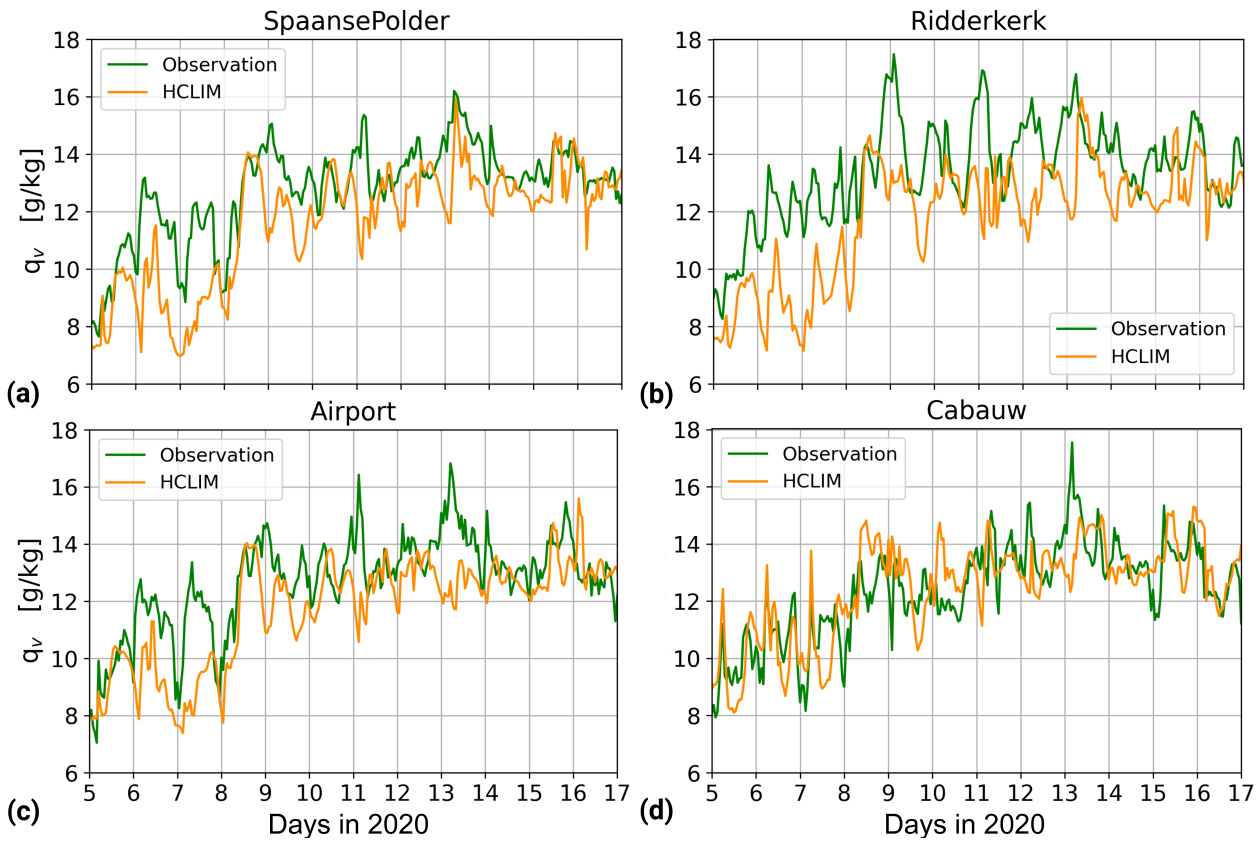

Figure 3.5: A comparison between the HCLIM model results (orange) and observed weather station data (green) for q_v [g/kg] from 5-08-2020 till 18-08-2020 for (a) Ridderkerk, (b) Spaanse Polder, (c) Airport and (d) Cabauw.

Now for 2021 the specific humidity still appears to be underestimated by HCLIM, but to a lesser extent than for 2020. A noteworthy day is August 12, 2021, where HCLIM expects a relatively low q_v compared to the day before, which is in contrast to the model observations. This effect is notable for the stations placed in an urban area (according to HCLIM), whilst again the predictions for Cabauw are most similar to the observations.

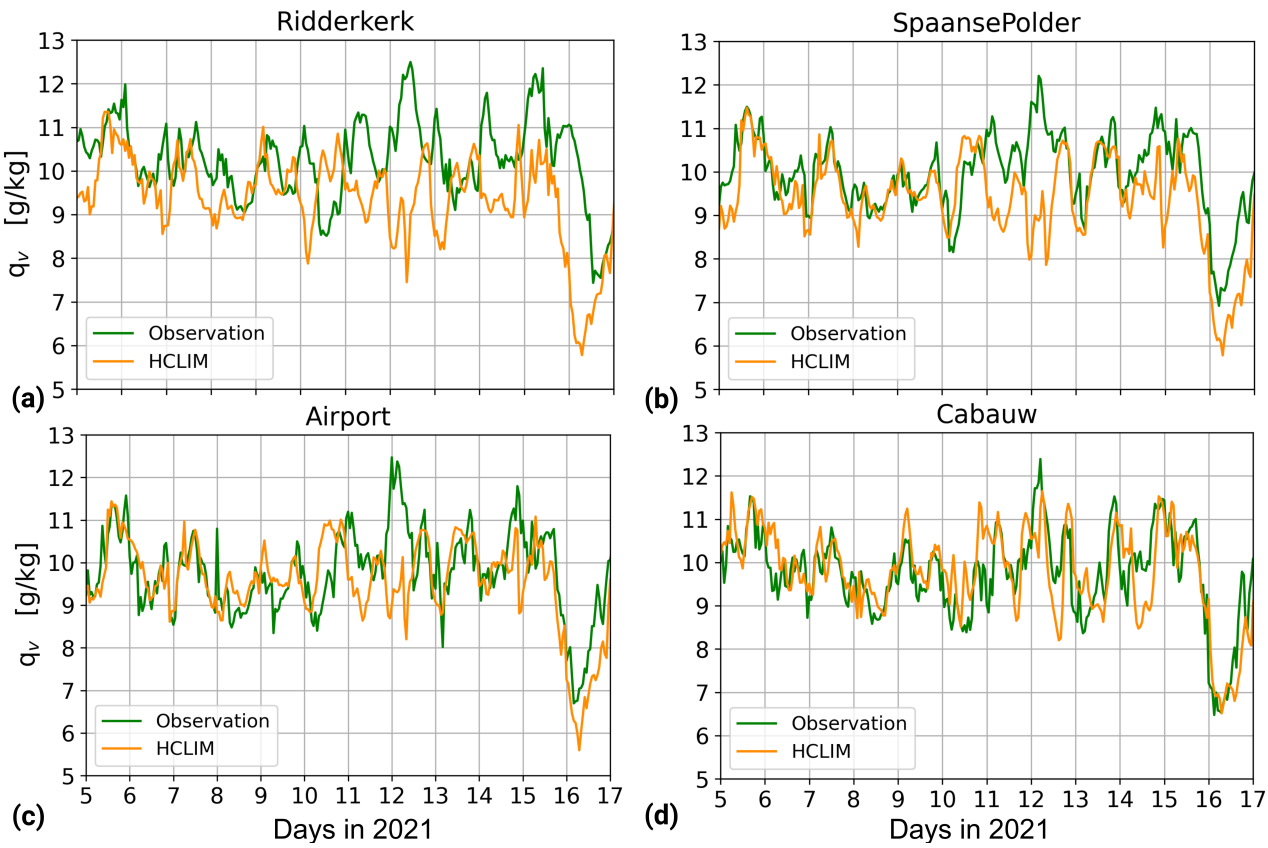

Figure 3.6: A comparison between the HCLIM model results (orange) and observed weather station data (green) for q_v [g/kg] from 5-08-2021 till 18-08-2021 for (a) Ridderkerk, (b) Spaanse Polder (c) the Airport and (d) Cabauw.

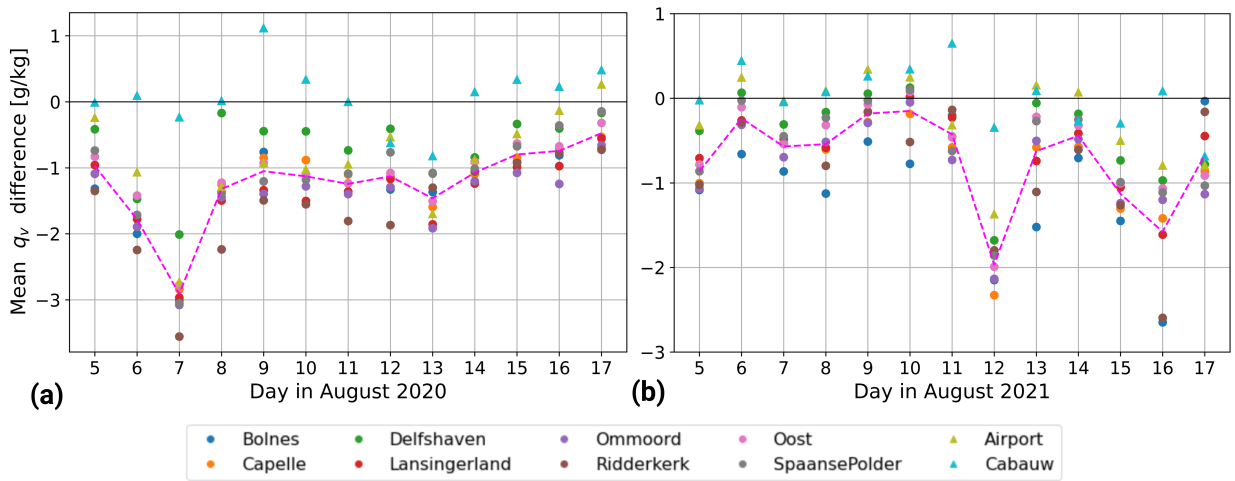

Figure 3.7: The daily mean difference between the HCLIM model results minus the observed weather station data for q_v [g/kg] from 5-08 till 18-08 during (a) a heatwave period in 2020 and (b) a regular summer period in 2021 for all TU Delft and KNMI weather stations. The fuchsia-colored line is the mean difference of HCLIM model results compared to only the TU Delft stations observations.

The mean differences (HCLIM - observations) are plotted for 2020 in figure 3.7a and for 2021 in figure 3.7b. The differences mentioned earlier on August 12, 2021, are distinctly observable. Also, on 7-08-2020, the differences are high. Across all days, the average differences across most weather stations as compared to the HCLIM model results are negative, excluding Cabauw exhibiting a

rather small positive (q_v) difference.

3.3. Discussion and conclusion

Table C summarizes the time-mean differences in temperature and specific humidity (q_v) for the periods of 2020 and 2021.

	Temperature [K]		q_v **[g/kg]**	
	2020	**2021**	**2020**	**2021**
Bolnes	1.11	0.006	-1.312	-1.057
Capelle	0.636	-0.285	-1.204	-0.825
Delfshaven	0.676	-0.0961	-0.688	-0.421
Lansingerland	0.730	-0.645	-1.40	-0.652
Ommoord	0.715	-0.218	-1.459	-0.797
Ridderkerk	1.805	0.370	-1.607	-0.845
Oost	1.166	-0.186	-1.125	-0.593
Spaanse Polder	0.966	-0.297	-1.108	-0.587
Airport	2.206	0.172	-0.900	-0.229
Cabauw	0.435	-0.736	0.082	0.022

Table 3.1: A summary of the mean differences (HCLIM - observation) for the temperature and specific humidity [g/kg] averaged over the period from 5-08 till 18-8 in 2020 and 2021.

While general biases are evident, the method has limitations due to varying observation heights, sub-optimal station locations near buildings, susceptibility to localized weather patterns, and the lower resolution of the HCLIM grid compared to point observations. This prompts the question of whether the HCLIM model inaccurately forecasts the variables or if the weather stations exhibit biases in observations, potentially originating from misplacement. Conclusions should be drawn with consideration of these limitations, emphasizing the need for further study. Overall, this chapter provides insights into model biases relative to weather station observations, concluding:

- HCLIM seems to overestimate the atmospheric temperature both during the day and the night during a heatwave, with a bias of approximately 1.5 K throughout all stations in 2020. For regular summer days of this period in 2021, these patterns are less clear and HCLIM underestimates the temperature more often, depending on the weather station.
- HCLIM seems to underestimate the specific humidity both during the day and night during a heatwave, with a bias of approximately - 1 g/kg throughout all stations in 2020. For the 2021 period, model results and observations are more aligned. For both the heatwave of 2020 and the regular summer days of 2021, outliers continue to be present for days with extreme rises and dips.

Also, some notable findings between urban and natural areas have been presented:

- The average 1 K temperature difference T_{TUD} - T_{Airport} for the weather station observation indicates an urban heat island effect in Rotterdam during the heatwave of 2020, as the KNMI Airport station is located just outside the city.
- HCLIM predicts extreme specific humidity changes better in a rural area than within the vicinity of a city.

4

From land use change scenarios to water storage areas

Both climate change and imposed land use change might demonstrate an impact on the local weather. A comprehensive approach that spans multiple sectors is essential for establishing anticipated land use changes in the Netherlands. Throughout the nation, policymakers, companies, research institutions, water boards, and universities continuously work on developing many scenarios for land use change. This has resulted in a wide range of existing scenarios, each considering various factors and assigning different levels of importance to them. As no decision has been made yet, it is necessary to select the most suitable scenario for this specific research in particular, given some requirements.

This chapter aims to evaluate various land use change scenarios for the future and assess their suitability for identifying potential areas for water storage. The first section 4.1 introduces the potential scenarios. Next, the method used *Multi Decision Criteria Analysis* is explained, and the criteria, weights, and scoring for application of this method are provided in section 4.2. Section 4.3 assesses all scenarios with the described method, leading up to a final decision on an area of interest for this research.

4.1. Introduction to scenarios

4.1.1. Opportunity map Climate buffers

Developed by Stichting Climate Adaptation Services (CAS) (CAS, 2023)

The 'Opportunity Map Climate Buffers' offers insights into ideal locations for natural climate buffers. It includes a primary map and five sub-maps, each focusing on specific buffer types and opportunities. One highlighted buffer type is water storage in the Randstad region, which faces challenges in managing heavy rainfall due to limited space. The map identifies low-lying grassland areas near Randstad's main drainage system as potential natural water storage sites, as illustrated in figure 4.1. These areas can temporarily retain excess rainwater, preventing flooding in nearby urban and rural regions. Additionally, designing these storage areas with natural principles can provide space for nature and recreation, enhancing the region's livability and resilience. To create the map, data analysis of the main drainage system using *Basisregistratie Topografie* (TOP10NL) was performed, and suitable grassland parcels near the system were selected from the *Basisregistratie Gewasperce-*

len (BRP 2020). The *Algemene Hoogtekaart Nederland* (AHN3) helped identify parcels at lower elevations than their surroundings. The final scenario output is a substantial amount of parcels in North and South Holland, which are identified as opportunities for climate buffers related to water storage.

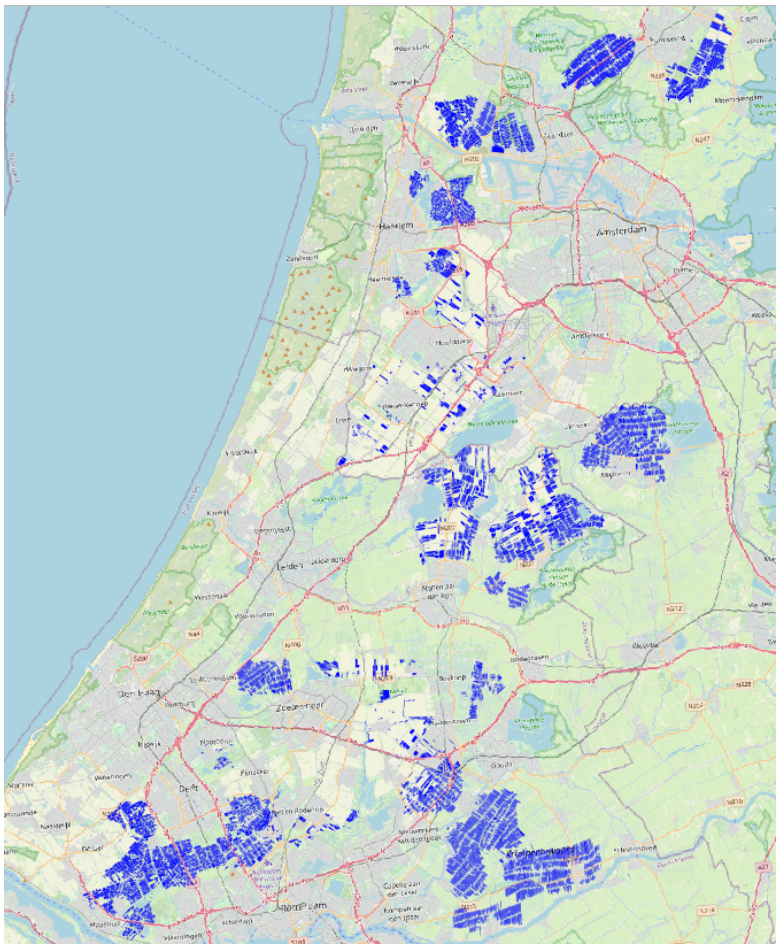

Figure 4.1: Illustration of the Opportunity map Climate buffers developed by Stichting Climate Adaptation Services. The blue areas indicate the parcels that are defined as an opportunity for water buffers (CAS, 2023).

4.1.2. Ruimtelijke verkenning

Developed by The Netherlands Environmental Assessment Agency (PBL). Published in 2023 (Kuiper et al., 2023)

In the *Ruimtelijke verkenning*, the PBL (Netherlands Environmental Assessment Agency) has developed four scenarios to aid policymakers. The objective of the *Ruimtelijke Verkenning* is to provide insights into the spatial aspects (conditions, effects, conflicts, opportunities) of transitions and other significant challenges in the physical living environment. It aims to assist policymakers involved in environmental and related sectoral policies in creating spatially coherent and future-proof policies. For each theme, potential spatial effects of various sectoral challenges that may arise in the long term are presented, including climate adaptation, energy transition, economic growth, strong and healthy cities and regions, and future-proof rural areas. There are four scenarios: "Global Entrepreneurship" with large corporations leading, "Rapid World" with increased digitization reducing distances, "Green Land" emphasizing natural spaces, and "Regionally Rooted"

where citizens initiate changes in their surroundings. For each scenario and theme, a map is created. It depicts the Netherlands in 2050 and was based on spatial modeling and design research to illustrate the consequences of different choices. Spatial modelling is done with *Tigris XL* (Zondag et al., 2015), the *Ruimtescanner* and the *Natuurverkenning* (Breman et al., 2022). Ruimtescanner simulates land use changes based on regional space demand and suitability for different land use types in GIS files with a 100-meter by 100-meter resolution. The representation of these climate adaptation measures, such as water harvesting, water retention, transitions from fresh to salt water, and reserve zones for peak river discharge, is less precise than the thematic map layers derived from spatial model calculations. The general goal of the scenario is to offer a comprehensive understanding of how these themes interrelate and impact the spatial landscape, enabling policymakers to make informed decisions for sustainable and resilient planning and development. The results are presented in multi-layered indicative low-resolution maps.

4.1.3. Delta Scenarios

Developed by The Netherlands Environmental Assessment Agency (PBL) and Deltares and published in 2017 (Wolters et al., 2018).

The goal of the Delta Scenarios is to assess the potential impacts of uncertain developments in the Netherlands' water management over the coming century. These uncertainties mainly include climate change, which could lead to both increased droughts and heavier rainfall, fluctuating river discharges, and rising sea levels. Socio-economic growth is coupled with population increases, demanding higher protection levels for densely populated areas and reliable freshwater supply. These two developments, climate change, and socio-economic growth, are considered autonomous and influenced by external factors. Given their uncertain developments, the Delta Scenarios aim to outline a plausible range, their interconnectedness, and potential consequences for land use and water management. These scenarios named *Stoom, Druk, Warm, Parijs* are built on KNMI'14 Climate scenarios and CPB (Netherlands Bureau for Economic Policy Analysis) and PBL's socio-economic WLO scenarios. The study assesses the Delta Scenarios' impacts on land use in the Netherlands using PBL's land use models, Ruimtescanner. For all water-dependent functions in the Netherlands and the multiple scenarios, key figures are developed, which is the main result of the Delta Scenarios.

4.1.4. Redesigning Delta's: Project Delfland

Developed by ZUS [Zones Urbaines Sensibles], Flux landscape architecture, and Sweco. Published in 2022 (ZUS et al., 2022)

In Midden-Delfland, heavy precipitation drains water rapidly to the Nieuwe Waterweg, while droughts require pumping from Lake Brielse. This system is no longer sustainable, considering the expected increase in periods of heavy precipitation or drought, the Boezem system has reached its maximum capacity. To secure future urban living below sea level, a significant overhaul and integrated solution are mandatory. This has led to the concept of the 'National Productive Park Delfland', which is illustrated in figure 4.2. The urban design plan offers chances to boost biodiversity and address problems like flooding, sinking land, and saltwater intrusion. When there is heavy precipitation, the park prevents nearby cities from flooding and stores water for use when it is dry by adjusting the drainage system.

Figure 4.2: An illustration of the concept of 'National Productive Park Delfland', adopted from the team Midden Delfland of Redesigning Deltas (ZUS et al., 2022).

4.1.5. A climate-proof buffer for South Holland

A study performed by Ir. A.C. (Coen) Kramer at the Department of Water Resources Management at the Faculty of Civil Engineering of Delft University of Technology and Province South-Holland. Under the supervision of Dr. E. (Erik) Mostert, Dr. Ir. Olivier Hoes, and Dr. F. L. (Fransje) Hooijmeijer (Kramer, 2023).

This thesis addresses water challenges in South Holland by proposing a water buffer system to mitigate climate change-induced floods and droughts. Focusing on the central region surrounded by barge canals, a water balance model, calibrated using existing pump data, simulates polder-level water flows. An above-average extreme version of the KNMI '14 Climate scenario is used to design realistic buffer design capacity. The selection of buffer locations is based on several factors: low elevation for ease of inflow and reduced excavation, minimal existing construction to avoid relocation, minimal disruption to existing infrastructure like highways and railways, and proximity to boezem waters. The optimal strategy involves a large buffer in the Noordplaspolder, connecting the Rotte and the Hoogeveensche Vaart, and a smaller buffer in Schieveen, as displayed in figure 4.3. The large buffer, next to Zoetermeer, should hold 34 million m^3 of water, based on the expected required buffer capacity for droughts, flooding, and regular expected climate change. The area covers 20.1 km^2, resulting in an average required water depth of 1.7 meters. These buffers offer historical, ecological, and recreational opportunities, reviving old barge canals and restoring historical connections. This strategy addresses various water management aspects and enhances the area's historical significance.

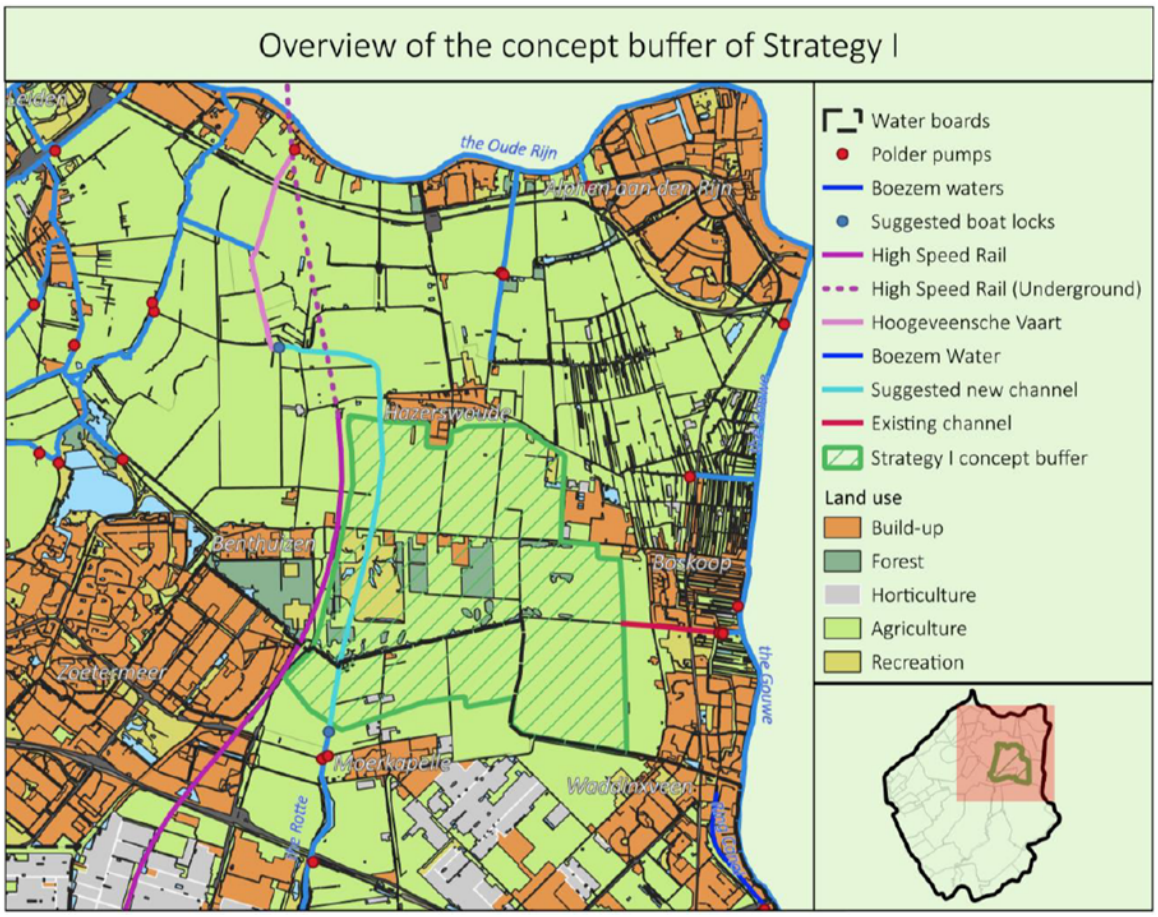

Figure 4.3: The illustration shows the concept buffer area that could be used for water storage in the Noordplaspolder, connecting the Rotte and the Hoogeveensche plassen (Kramer, 2023). Directly adopted from the research project "A climate proof buffer for South Holland" performed by Ir. A.C. (Coen) Kramer.

4.2. Introduction to assessment method: Multi-Criteria Decision Analysis

Several important factors are explored, ultimately leading to the selection of a specific land use scenario for the experimental setup for this research. This scenario will serve as input for the modification of land use maps integrated into the HARMONIE-Climate model. The assessment of each scenario for this particular research goal is based on six key criteria, which are listed and described below:

1. **Spatial resolution**: the scenario is developed on a sub-regional level, preferably with a resolution that is close to matching the 300-meter resolution of the land use map used in HCLIM.

2. **Covered region**: the focus area is in the present study near the city of Rotterdam. The scenario should at least focus on the Netherlands, and scores higher if it focuses on the province South-Holland, and even higher with a focus area near the city of Rotterdam (water boards: Schieland & Krimpenwaard, Delfland and Hollandse Delta).

3. **Water storage area sizes**: the scenario proposes actual water storage locations instead of indicative potential areas. These locations are covering an area of at least 300 meters by 300 meters, preferably at least the model resolution of an HCLIM grid cell.

4. **Water policy aspects**: aspects of water-related policy and factors are included, such as NAP levels, water board policy, polder-boezem water balances, and considerations related to infrastructure.

5. **Resilience to climate change and socio-economic growth**: climate change scenarios, climate adaptation measurements, socio-economic factors, and academic or institutional research are included.

6. **Up-to-date, comprehensive and future-proof**: the more recent the scenarios, the better. Also, the strategy for choosing potential locations should be transparent and comprehensive. The scenario information itself should be presented completely. The scenario is preferably not static and will be continuously updated throughout the years, based on relevant developments.

To quantitatively evaluate the key factors, a Multi-Criteria Decision Analysis (MCDA) has been developed (Belton and Stewart, 2002). For each criterion, a scoring system and a relative weight are defined. The scoring system defines how well a scenario meets the specific criterion. The weight stresses the importance of the criteria for this research, ranging from 1 to 3, less to more important. The scoring table is presented in table 4.1.

No	Name	Weight	Low (1)	Average (2)	High (3)
1	Spatial resolution	3	>2000 m	300 - 2000 m	300 m <
2	Covered region	2	>Netherlands	Randstad region	South-Holland
3	Area size	2	<300 m or none	300 - 2000 m	>2000 m
4	Water policy aspects	3	1 or 2 aspects	3 aspects	4 aspects
5	Climate resilience aspects	2	1 or 2 aspects	3 aspects	4 aspects
6	Up-to-date & future-proof	1	1 aspect	2 aspects	3 aspects

Table 4.1: The 6 criteria of the MCDA, each with its weight, and values. For criteria 4, 5, and 6, a point is assigned if a scenario treats the topics of interest. For criterion 4 and 5 there are four topics in total. For criterion 6 there are 3 topics. Details on the topics of interest are presented in the text.

For criterion 4, a point is assigned when the reasoning behind the scenarios includes matters such as the (1) AHN, (2) water board or provincial policy, (3) polder-boezem calculations, and (4) the effect on existing infrastructure. For criterion 5, the conditions include future climate scenarios (1), climate adaptation measurements (2), socio-economic growth (3), and if it is based on institutional or academic research (4), such as Well-being and Living Environment (WLO), Natuurverkenning and KNMI'14/KNMI'23 Climate scenarios. For criterion 6, a point is assigned when the scenario is up-to-date, comprehensive in its explanation, and future-proof, which means it is a scenario reassessed continuously based on any relevant developments in this field.

Scenarios or research that are in early-stage development or showed incomplete information to utilize them at the date of evaluation, or were out of the scope of this research focus area, are shortly described in the retrospective in A.1.

4.3. Assessment of scenarios

For each scenario individually, additional background information is provided, including who developed the scenarios, the general principles of the scenario, and the assessment of the scenario.

The final scoring and the Multi-Decision Criteria Analysis are shown in figure 4.4. The optimal scenario within the scope of this thesis is presented in the study named *A climate proof buffer for South Holland*, as part of a research project at the Department of Water Resources Management at the Delft University of Technology and Province South Holland.

Multi-Criteria Decision Analysis			**Scenarios**	**1**	**2**	**3**	**4**	**5**
				Opportunity map climate buffers	**Ruimtelijke verkenning**	**Delta scenarios**	**Redesigning Deltas: Project Delfland**	**A climate proof buffer for South-Holland**
	Criteria	**Weights**						
1	Spatial resolution	*3*	Score	**3**	**1**	**1**	**3**	**3**
			Points	*9*	*3*	*3*	*9*	*9*
2	Covered region	*2*	Score	**2**	**1**	**1**	**2**	**3**
			Points	*4*	*2*	*2*	*4*	*6*
3	Lake sizes	*2*	Score	**1**	**1**	**1**	**3**	**3**
			Points	*2*	*2*	*2*	*6*	*6*
4	Water policy aspects	*3*	Score	**1**	**2**	**3**	**2**	**3**
			Points	*3*	*6*	*9*	*6*	*9*
5	Future climate and adaptation	*2*	Score	**1**	**3**	**3**	**3**	**2**
			Points	*2*	*6*	*6*	*6*	*4*
6	Up-to-date and complete	*1*	Score	**2**	**3**	**2**	**2**	**2**
			Points	*2*	*3*	*2*	*2*	*2*
			Total	**32**	**33**	**35**	**48**	**52**

Figure 4.4: A table summarizing the assigned scores for each criterion and scenario. The scores are multiplied by the weight of the criterion, adding up to the number of points. The number of points are added to each other, resulting in a total. The highest total indicates that the scenario based on the multi-decision analysis developed for this research is the most usable.

1. Opportunity map Climate buffers

The proposed opportunities are individual parcels, which results in a high score on criterion 1. The focus area is Randstad, but not with a high focus on the near-Rotterdam area, scoring average on criterion 2. Since the map does not propose specific water storage areas with particular sizes, it scores low on criterion 3. It does include the AHN and the drainage system using TOP10NL, but does not yet elaborate on policy, infrastructure, or water level sections, scoring low on water policy aspects. It focuses on climate adaptation but does not seem to include climate scenarios, socio-economic factors, or extended research yet, scoring low on criterion 5. Lastly, the maps are recently developed, but a thought-out comprehensive strategy is not found. If this scenario would be used for the case setup, many assumptions need to be made to pinpoint specific locations. Further filtering locations can be done by only including the lowest parcels, those distant to infrastructure and high flood depths, next to including water management policies and socio-economic growth. In general, the CAS maps are continuously updated, scoring average on criterion 6.

2. Ruimtelijke verkenning

As the presented maps are not in raster format but more indicative, the scenario scores low on criterion 1 (maps are not shown here). The focus region is the entirety of the Netherlands, scoring low on criterion 2. The water storage areas are vaguely defined and simplified and therefore it scores low on criterion 3. The layer climate adaptation is water management policy focused, with expertise from Deltares and CPB. The exact calculation method is so far unclear, but the report sources and involved stakeholders, indicate at least an average score on criterion 4. As the entire focus of the *Ruimtelijke Verkenning* is projections of spatial design taken into consideration climate change and socio-economic developments, it scores high on criterion 5. The scenario is

presented with extensive background reports in spring 2023, resulting in a high score for criterion 6. Also, it is expected CPB will continue to work on this.

3. Delta scenarios
In general, the usability of the Delta scenarios is relatively similar to the Ruimtelijke Verkenningen. However, the Delta scenarios provide general maps of future land use for each scenario, where no actual new water storage areas are defined (maps are not shown here). On the other hand, the general focus of the Delta Scenarios is water, which is why it scores higher on the water policy criterion. The last update of the scenario is 2017. It is expected the Delta Scenarios will be updated in the upcoming years, based on the recently published KNMI'23 Climate scenario (KNMI, 2023). This results in an average score for criterion 6

4. Redesigning Delta's: Project Delfland
The 'boezem buffer' area comprises a relatively big space. The map shows infrastructure on a relatively zoomed-in level, but the figure is indicative. Also, the area focuses on Delfland, which lies adjacent to the northwest side of Rotterdam. Therefore, the scenario scores high at criteria 1 and 3, but average on criterion 2. Also, it mentions all water policy aspects, but not thorough calculation of the water system and it requires big changes in the infrastructure, scoring average on criterion 4. It comprises climate forecasts and adaptation measurements but does not explicitly mention climate scenarios. The concept was published in 2022, hence the information is up-to-date. It is unknown whether updates will be done or how applicable this concept will be in a practical sense. Also, the concept is well-explained, scoring high for criterion 6. Altogether, the scenario is well thought through, but has more of an urban development and design-focused aspect, instead of a quantitative and water-focused aspect.

5. A climate proof buffer for South Holland
The scenario development of this thesis is very extensive. As specific locations of > 2 km^2 water buffers are provided for water storage areas in the center of South Holland, it scores high on criteria 1, 2, and 3. A full chapter is dedicated to policy, water balance modeling, and hydrological simulations of the entire polder-boezem system, scoring high on criterion 4. Also, it includes climate change scenarios, climate adaptation, and spatial development of the population. However, the socio-economic scenarios are not as extensive as the other scenarios, scoring average on criterion 5. The research was published in the summer of 2023, with full transparency and reasoning on the developed strategies, but lacks a clear note on future updates. This results in an average score on criterion 6.

5

Case set-up

In chapter 4, the location for the water storage area is chosen, by weighing the criteria for different scenarios. This resulted in a location next to Zoetermeer, called the Noordplaspolder, which connects the Rotte and Hoogeveensche Vaart. Now we have decided upon the case study area, we will continue to describe other elements of the case setup. In section 5.1, weather conditions enhancing arboviral emergence are described, based on input from multidisciplinary research. Section 5.2 describes the method for technically modifying the land use maps in HCLIM and is applied to the area in the Noordplaspolder. Section 5.3 provides the HCLIM configuration settings for all experiments and section 5.4 presents a pre-study on the initialization of the experiments. Finally, the data processing methods are given in section 5.5.

5.1. Periods of interest

As mentioned in the introduction, changes in land use and global warming impact salinization, thermal and humidity levels, which in turn influences mosquito abundance and species composition. Climate change also impacts bird migration patterns, which can intensify West Nile Virus (WNV) circulation in birds and spill over to humans in Northern Europe. These relations, which are currently studied in the PDPC Frontrunner project for the Netherlands, raise the question of which periods are of interest for the experimental set-up. Section 5.1.1 discusses the thermal and humidity relation to mosquito development, bird migration and viral transmission. With this knowledge, we motivate in section 5.1.2 the final decision on the simulation periods for the present study.

5.1.1. Weather conditions for mosquito, bird and viral transmission

In general, high temperatures are conducive for the replication of both viruses and mosquitoes (Paz et al., 2013; Vogels et al., 2016, 2017). For the living conditions of mosquitoes themselves, lower temperatures are more favorable, as high temperatures decrease the life span of mosquitoes. The transmission cycle of the WNV seems to establish at a sustained temperature of 28 °C or higher. Above 28 °C or more, the metabolic system of a mosquito accelerates, reducing the likelihood of viral transmission. The development of mosquitoes from eggs to adults also accelerates at higher temperatures, increasing the population. For regions with low average summer temperatures of 18 °C, WNV establishment seems only possible when the mosquito-to-host relation is high (Vogels et al., 2017). Ideally, weather conditions are ten following weeks with a minimum temperature

of 18 °C. All these thermal relations can be incorporated in a model describing the reproduction number R_0, as readily visualized in figure 1.2 ($T_{\min} \approx 17$°C, $T_{\text{opt}} \approx 28$°C and $T_{\max} \approx 35$°C). Additionally, higher humidity levels are beneficial for mosquitoes, as they tend to live longer under such conditions (Costa et al., 2010; Brown et al., 2023). Mosquito-borne diseases typically peak after periods of high precipitation, although the relationship is not as precisely established as it is for temperature. Also, it is mentioned humidity levels are especially important in mosquito life cycles when the ambient temperatures is nearing the upper thermal limit $T_{\max}$, which is less prevalent in Northern regions (Brown et al., 2023). Also, the softness of the winter demonstrates an effect on the virus presence in spring. For example, the Usuntu Virus (USUV) popped up in spring and peaked in August and September of 2016 (Rijks et al., 2016). The summer of 2016 was known for a wet June, with extremely high temperatures in August and September.

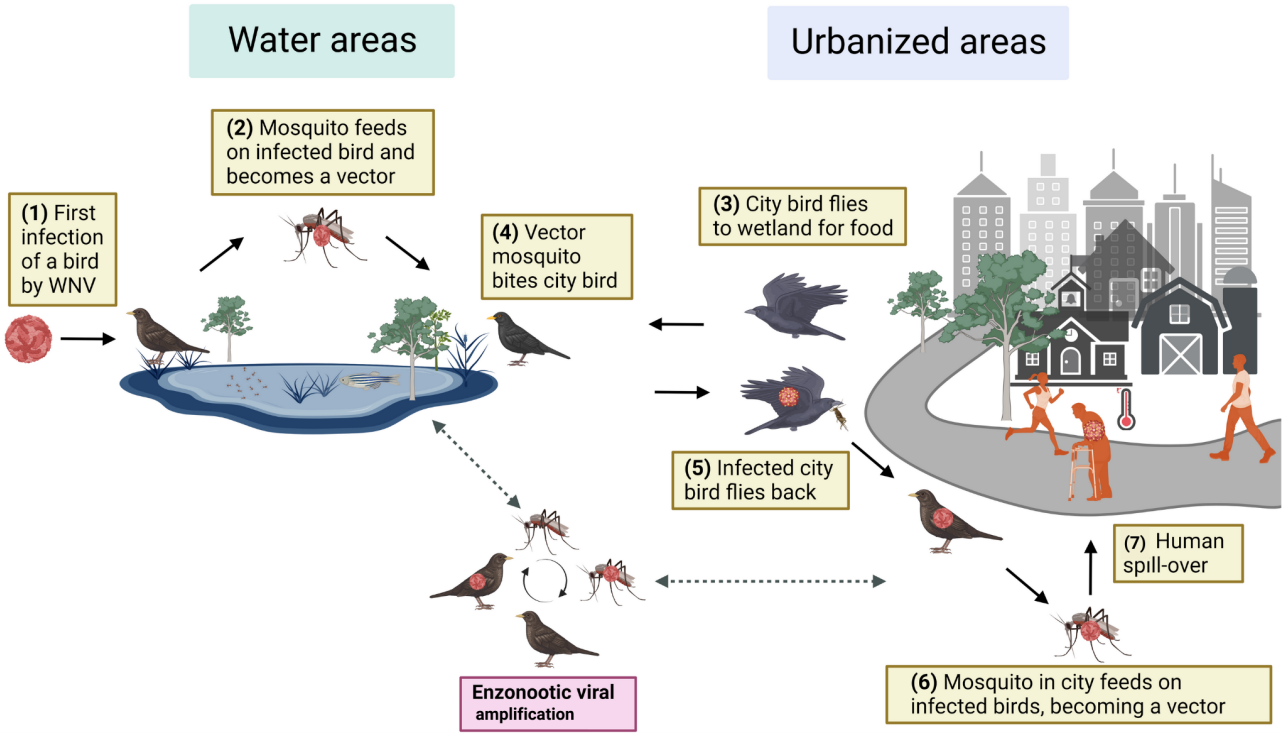

Figure 5.1: An illustration of the transmission cycle of vector-borne diseases. (1) Near a water area, a bird (host) is infected by an arbovirus such as WNV. (2) Healthy mosquitoes feed on the infected birds, resulting in an infected mosquito (vector). (3) City birds relocate to the water area to find food. (4) Infected mosquitoes feed on the city birds, transmitting the virus. (5) The city bird flies back to the urbanized area. (6) The host-vector (bird-mosquito) transmission cycle replays. (7) Mosquitoes also feed on humans (dead-end hosts) and human spillover takes place. Human infection results in fevers or mortality risk. During the transmission cycle, zoonotic viral amplification takes place.

Throughout the year, bird populations travel the world through different flyways, mixing with each other. Especially after the breeding in spring season, birds start migrating. The Netherlands is known to be an intercontinental hub for a substantial amount of migratory birds (Helm et al., 2012). Studies mention water development will drive bird population development more than drought does, especially for water birds (Moulton et al., 2022). Birds relocate due to a lack of food in the city, which is why they transfer between cities and wetlands. In wetland areas, mosquitoes can serve as vectors for the transmission of pathogens between the local infected birds and the healthy birds from urban environments that briefly visit the wetlands for foraging. As these urban-dwelling birds return to their city habitats, mosquitoes may acquire the pathogen from them and

potentially transmit it to humans. Figure 5.1 illustrates the transmission cycle of arboviral spread and the bird-mosquito-human interaction near water and urbanized areas.

As the effect of bird development due to local climate change remains to be further researched, it is preferable to keep a broad view considering the simulation period. In general, periods of mild winters allow mosquitoes to diapause, still circulating in spring, enhancing the risk of viral transmission. Soft springs and summers with long heatwaves are interesting for an indirect increase of vector-borne viral replication as well as the presence of mosquitoes as virus carriers. Considering precipitation events, it appears both extreme drought and extreme precipitation could be of interest for inducing changes in the local ecosystem. Therefore, a year is preferred with periods of low or high precipitation levels, followed by extreme heat. For the changes in land use, it is important to study areas with water development. To this end, both the effect of the ECOCLIMAP-SG cover map types wetlands (23) and lakes (3) are of interest.

5.1.2. Simulation period

We analyzed the climatology of the past 5 years to select a period that roughly meets the favorable conditions for the WNV transmission cycle (KNMI, a). The conditions entail a mild winter and spring, followed by an excessively hot summer, with either a period of high or low amount of precipitation. Within the scope of this research, the selected period is 1 April 2022 till 1 October 2022. This period is characterized by a preceding soft winter, a dry and sunny spring, but also relatively high precipitation levels in June followed by extreme heatwaves, like during the USUV outbreak in 2016 (Rijks et al., 2016). A complete summary of the analysis of seasonal observations is provided in Appendix A.2.

Since higher temperatures disturb the mosquitoes' living conditions and precipitation is useful to study the effect of changes in land use, two short-term periods of interest were chosen: a heatwave and a day of heavy precipitation. In summer 2022, the heatwave ran between 9-16 August and peaked on August 12th. The 5th of June is known for its extreme precipitation, leading to flooding in Dutch towns.

5.2. Methods to modify land use maps

To impose changes in land use and mimic the creation of water storage areas in the Randstad, the physiographic data files `ecosg_final_map.dir`, `GlobalLakeDepth_V3.0.dir` and `GlobalLakeStatus_V3.0.dir` needed to be modified, of which the characteristics are explained in section 2.2.1 and 2.2.2. For the remainder of the text, the individual PGD files will respectively be referred to as the land cover map, lake depth map, and lake status map. All PGD files are of a binary type and are manipulated in `FORTRAN`, which means the data of the files is changed. The code that was readily developed for similar manipulation techniques, and adjusted for this specific research purpose, is provided in Appendix B.1.

As the entire workflow is non-trivial, a general step-by-step workflow combined with the used software is schematically illustrated in figure 5.2.

In the current workflow, the exact location of the new lake is determined by contouring the location in `QGIS`. Within this software, the resulting polygon vertices are obtained as coordinates. In a `Python` script `coord_transfer.ipynb`, these `QGIS` outline coordinates are compared with the grid coordinates of the land cover map, lake depth map and lake status map, which generates an array with modified coordinates for all values within the outline coordinates. In the `FORTRAN` subrou-

tines, specifically in the `mod_ecosg_cover.F90`, `mod_lake_depth.F90`, and `mod_lake_status.F90`, a loop is implemented to iterate over the respective maps. During this process, the code matches the prospective change coordinates with the correct locations within the file. Now that the maps are updated including the presence of a new lake, they must be embedded within the HCLIM system, such that the right map is read properly during simulations.

To this end, it is essential to create new references within the HCLIM system to locate the modified files in the `Env_system.sh` and `Prepare_PGD` subroutines. By doing so, in the `PGD` step, the model can accurately read the new cover and lake data. For further technical details on the manipulation of land cover and lake maps, including a representation of the relevant code structures, please refer to the content provided in Appendix B.1.

A challenging difference between the modification of the land cover map compared to the lake maps is the resolution. The spatial resolution of the land cover map is on average three times higher than the resolution of the lake status and lake depth maps. This results in water storage areas in the lake maps on an approximate 1 by 1 km spatial resolution, which deviates substantially compared to the actual drawn contour. As explained in section 2.3, it is important to note that when it comes to the existence of lakes, the land cover map plays a dominant role. This means that the information provided by the land cover map takes priority over that from the lake maps.

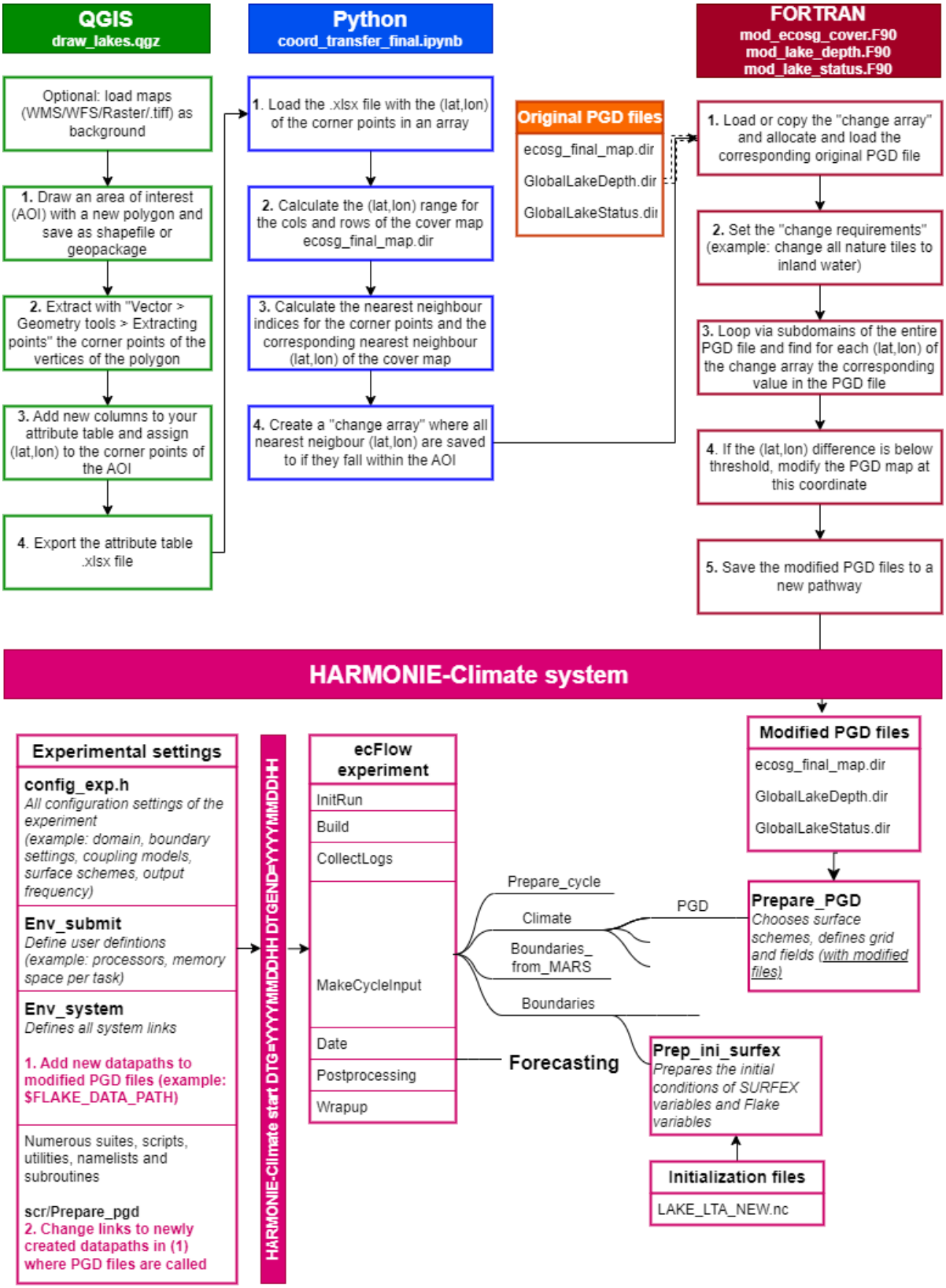

Figure 5.2: A step-by-step software workflow for modifying the land cover and lake maps. The exact location of the new lake is drawn in `QGIS`, resulting in coordinates of the polygon vertices. In `Python`, the `QGIS` outline coordinates are matched with the coordinates of the cover and lake maps, resulting in a changing array with modified coordinates representing the presence of new lakes. In `FORTRAN`, the `mod_ecosg_cover.F90`, `mod_lake_depth.F90`, and `mod_lake_status.F90` code loops over the cover or lake map and matches the prospected change coordinates to the correct location of the file. Within the HCLIM system, new references to the modified files have to be made so the new cover and lake are correctly read by the model (see Appendix B.1).

To provide an idea of the in-between results from the workflow, figure 5.3 shows a visualization of the maps obtained during the different steps. The visualization indicates the lost resolution and accuracy over the course of the workflow. The initial outline of the drawn water storage area is shown in black, which is located at the Noordplaspolder east to Zoetermeer (seen on the lower left). The lighter pink pixels indicate the resulting difference in the cover map. During the `PGD` step in SURFEX, the cover and lake maps are read and the initial SURFEX files are created as described in section 2.1. Amongst them, SURFEX creates NetCDF4 files with for each grid cell the area cover of sea, lake, nature, or town in percentages. The blue shaded area indicates the fraction of inland water present in the grid cell, where darker blue implies more water. Other kinds of land cover tiles from SURFEX make up the other fractions of the single grid cell.

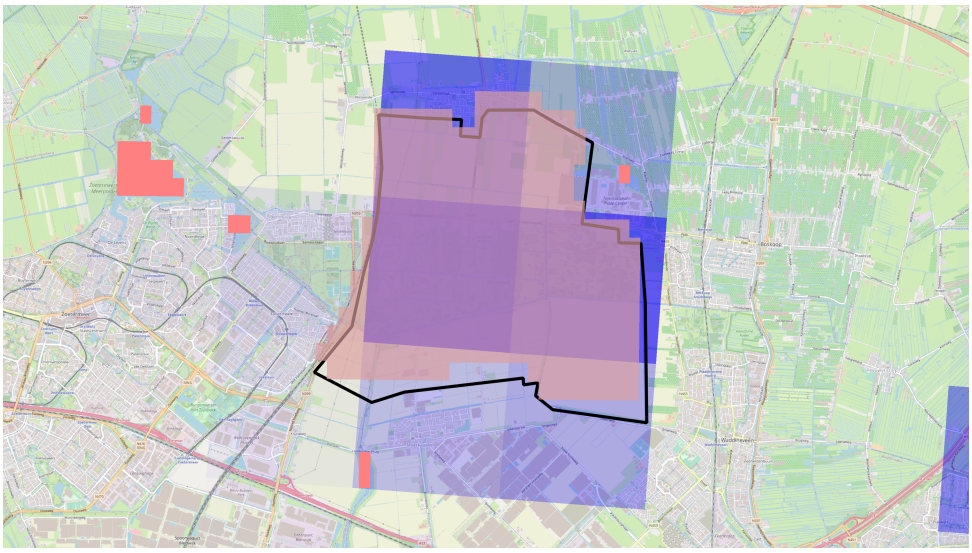

Figure 5.3: A layered illustration of the in-between resulting maps of the workflow to change land cover and lake maps for water storage area design in `QGIS` (black line) and the resulting changes in the cover map after `Python` and `Fortran` manipulations (light pink). The blue shaded squares represent the fraction of inland water area read during the `PGD` step in the HCLIM grid cells (darker blue implies more inland water) since the single grid box allows for multiple kinds of land cover tiles.

Important to note that when you initialize a new lake in the model, you choose a certain location and depth, which is completely fixed, in the sense that the lake remains there permanently and not temporarily. In other words, a time-varying lake depth is not possible, hence a shallow lake can never dry up. For a wetland, a fundamentally different scheme is chosen since its cover type falls under a nature tile, namely ISBA. Therefore, the underlying physical parametrizations are different than for a lake, for which the dynamics are calculated by the FLake model.

5.3. Experimental HCLIM system set-up

In this section, the configuration settings for all experiments are provided. First, the default settings are described, after which the alternative settings for the different experiments are introduced in the subsections.

For all experiments, we utilize the HCLIM model, specifically the 43rd cycle (HCLIM43), which is an evolution of HCLIM38 (Belušić et al., 2020). The model is fed every 3 hours by boundary conditions derived from hourly ERA5 data. ERA5 uses data assimilation from the Integrated Forecast System (IFS) with 4-dimensional variational analysis (4D-var) (ECMWF, 2010). SURFEX is directly

coupled to the experiments and its default surface schemes are used (SEAFLX, FLAKE, ISBA, and TEB). By default, we set the model domain to the `NETHERLANDS` with an input file through a lat lon selection, which results in a spatial resolution of 2.5 by 2.5 km on a Lambert grid with 789 by 789 grid points in a horizontal plane, centered around 51.967°N and 4.9°E. It uses a 65-level structure in the vertical, starting at sea level and increasing with pressure levels. The time resolution is 60 seconds, which is lower than the original 75 seconds, to avoid model instability and subsequent crashes. This problem is eliminated by reducing the time step. For most variables, the output is hourly and grid cell averaged. The write-up times of the model output are daily for history and SURFEX files.

5.3.1. Lake, wetland and control experiments

For the regular experiments, 3 different experiments have been conducted, which are 2 test experiments with either a new lake or a new wetland at the designated area, and a control experiment with original land use.

As described in section 2.2.1, `ecosg_final_map.dir` has 14 vegetation types in its nature tile, of which one of them is wetland (23). Each vegetation type receives time-dependent values from the physiographic data files for the vegetation height (`HT`), visible and near-infrared albedos (`ALBVIS`, `ALBNIR`), and the leaf-area index (`LAI`) depending on its cover type provided by the cover map. These surface parameters remain to their seasonally dependent default values for all experiments.

Each natural cover type receives settings for the minimal stomatal resistance $R_{s,min}$ and the vegetation heat capacity C_v (high or low). The original land use map is an agricultural area, mainly covering types of winter C3 crops, summer C3 crops, and C4 crops, which will together be referred to as C. Also, C stands for control, since it is the original land use in this area. The wetlands are entirely covered in flooded grassland.

The vegetation heat capacity values and minimal stomata resistances for the C and W experiments are provided in table 5.1.

	ECOCLIMAP-SG cover type	C_v [Jkg^{-1}]	$R_{s,min}$ [s/cm]
Crops / Control (C)	winter C3 crops (19)	$2.0 \cdot 10^{-5}$	60
	summer C4 crops (20)	$2.0 \cdot 10^{-5}$	60
	C4 crops (21)	$2.0 \cdot 10^{-5}$	135.6
Wetland (W)	Flooded grassland (23)	$2.0 \cdot 10^{-5}$	40

Table 5.1: An overview of relevant cover type properties, for the crops/control experiment (C), this a mix of winter C3 crops, summer C3 crops, and C4 crops, and the wetland experiment (W). The properties given are the vegetation heat capacity C_v and minimal stomatal resistance $R_{s,min}$

All simulations ran from the 1st of April 2022 until the 30th of September 2022. The modified cover maps for the experiments are shown in figure 5.4 for the (a) original crops, (b) lake, and (c) wetland simulations. The modified lake maps for the experiments are illustrated in figure 5.5, with (a) the lake status map set to 3 and (b) the lake depth map set to 2 meters at the case study area. The domain, spatial and temporal resolution, and boundary conditions remain the same.

As solving an NWP model on a higher resolution provides more insights into the changing local weather patterns occurring due to land use change, efforts have been made to conduct higher spatial resolution (1 x 1 km) and temporal (24 s) experiments. Such resolutions with HCLIM are currently still experimental and not in operation use. Developments on implementing this for

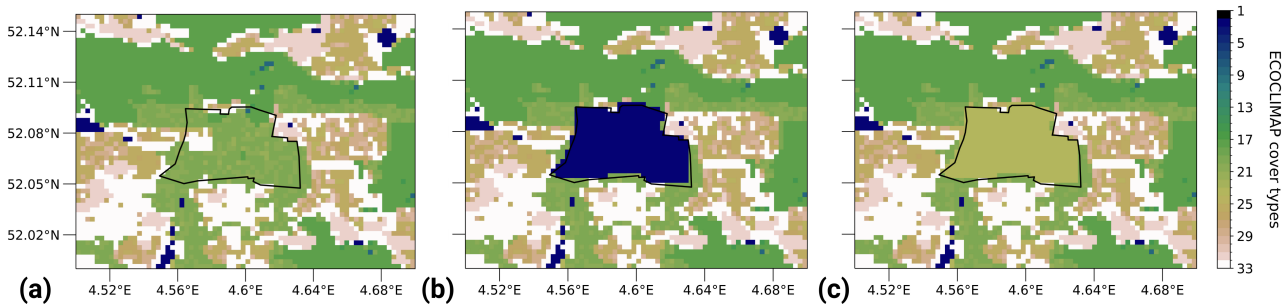

Figure 5.4: An illustration of (a) the original land use cover consisting mainly of nature tiles, characterized by C3 and C4 crops, (b) the cover map for the lake experiments, and (c) the cover map for the wetland experiments, all three at the same location.

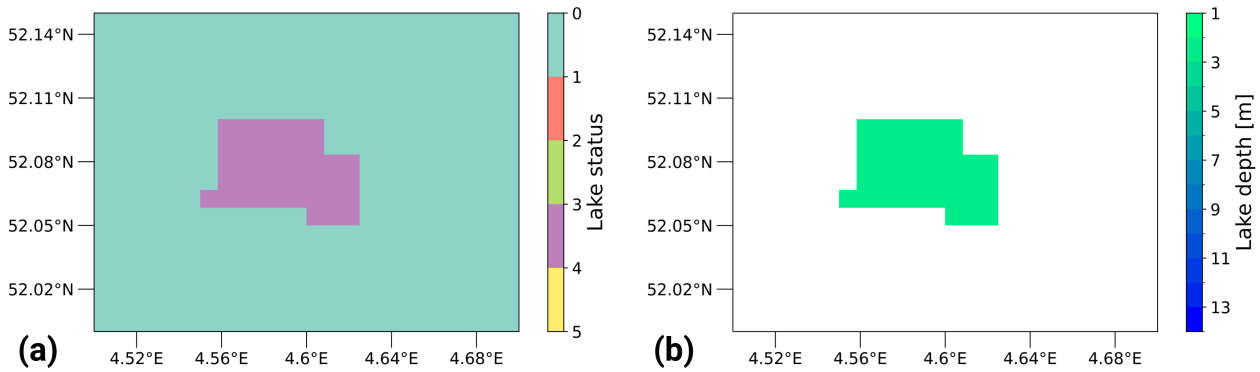

Figure 5.5: An illustration of the modified (a) `GlobalLakeStatus_V3.0.dir` map and the (b) `GlobalLakeDepth_V3.0.dir` map for the case study area. The status is set to 3 since a specific lake depth is assigned (refer to table 2.1). The lake depth is set to 2 meters. The resolution of the map is 30 arcseconds, which is approximately 1 km.

lake and wetland experiments have been made, such as testing the possibilities of high resolution on the `NETHERLANDS` domain and nesting a smaller domain in a default resolution experiment providing lateral boundary conditions. As these experiments are computationally expensive and technical obstacles keep occurring due to data storage problems, no full experiments have been conducted. All required steps to perform such experiments, and a review of the both overcame and remaining obstacles, are outlined in appendix B.3.

An indication of the `NETHERLANDS` domain size is visualized in figure 5.6, which can manually be set with the HIRLAM-NWP domain design tool.

5.3.2. Flake model monitoring experiments

Within SURFEX the Flake model is called if an inland water tile is present. In the regular experiments described in section 5.3.1, the water surface temperature is a default output variable, but the water column temperatures are not. To further study the temperature profile within the water column and the diurnal evolution of the energy budgets at the surface-atmosphere interface, experiments have been set up to obtain such Flake-specific variables. More specifically, we monitored the depths of the mixed-layer h , the temperature of the mixed layer T_{wml} , the mean water column temperature T_{mnw} , the bottom temperature T_{bot} , and the shape factor of the thermocline C_{T} , as presented in figure 2.5 of section 2.4.

The configuration settings and technical details to obtain an output with a high temporal reso-

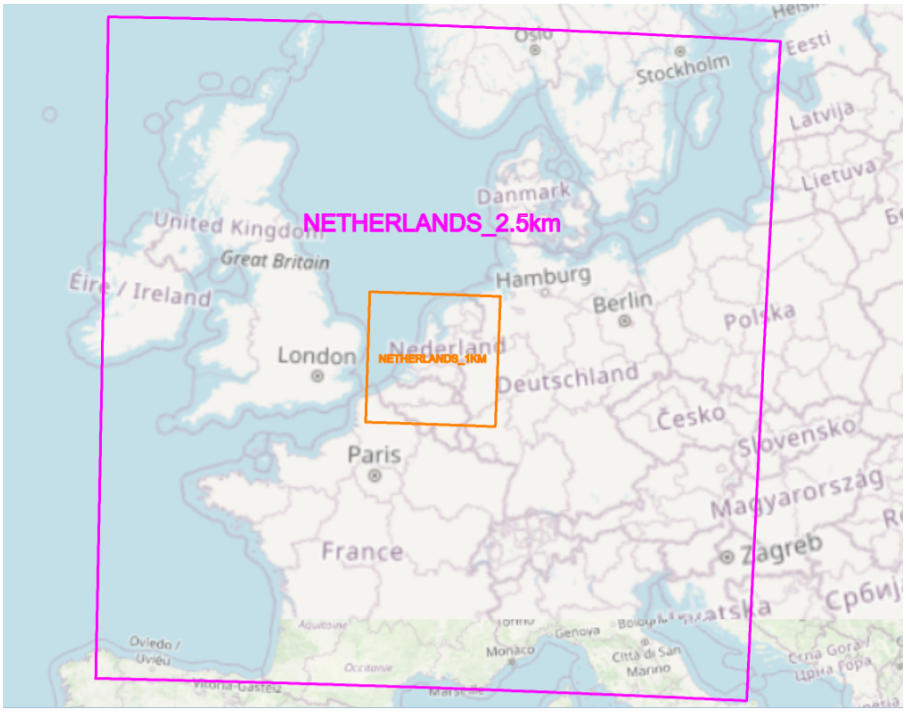

Figure 5.6: The default domain for all experiments `NETHERLANDS` is shown in pink, with a spatial resolution of 2.5 km^2, reaching from the south of Scandinavia to the North of Italy and from Ireland to Poland. The orange domain is the nested domain for 1 km experiments, covering the entirety of the Netherlands. The boundaries of the 1 km^2 spatial resolution domain are hourly fed by the 2.5 km^2 domain forecasts.

lution for FLake variables are not trivial. Therefore, the required adjustments within the HCLIM system are provided in Appendix B. An important current technical limitation restricts the maximum length of a run to a couple of days, due to the limited amount of available digits to store certain file formats used in postprocessing the forecast output. Therefore, for this study, simulations run only 1 full day to monitor a diurnal cycle on the 5th of June 2022 (high precipitation levels) and the 12th of August 2022 (heatwave), with a cold start.

5.4. Pre-study of spin-up period within simulations

As explained in section 2.5, whenever a new lake is created during the PGD step, the system reads a lake temperature from the lake initialization file. As it is not clear whether the same map is used for existing lakes and the spin-up period might have an impact on the interpretation of the results, this section investigates the initialization of lakes further.

The `LAKE_LTA_NEW.nc` map provides climatological mean values on a sparse spatial resolution of 1°, compared to the model grid (refer to section 2.5). Also, it is year-independent and developed in 2012. If a soft winter has passed, average temperatures are higher, or when the experiment starts mid-summer and lacks the heating of previous summer months, actual lake temperatures might be higher than the climatological means of the file. Therefore, to prevent a bias that is due to using a climatological-based temperature a long spin-up period is recommended. However, due to time restrictions, the longest simulations of this study ran only from 1 April 2022 to 1 October 2022, thus a long spin-up period had not been implemented. To investigate the spin-up period of the regular experiments, we took a critical look at the cold start and possible effects of the spin-up period, for both existing and new lakes, for all experiments described in sections 5.3.1 and 5.3.2.

To provide an idea of the spin-up period, a comparison has been done to assess whether the HCLIM model results for the lake surface temperature in the first month do not deviate substantially from the lake surface temperature after a spin-up period of 6 months. Next to this, it enables us to investigate how the initialization of existing lakes works when starting a simulation in the HCLIM system. This can be done by comparing climatological mean values of `LAKE_LTA_NEW.nc` that were used to initialize a new lake and an existing nearby lake with similar depth and size called Reeuwijkse Plassen, for simulations starting at different months. It is hypothesized the existing lake also receives a climatological mean value at the start of an experiment.

Figure 5.7 shows the model results for the water surface temperature for a new lake and Reeuwijkse Plassen for a simulation that started on the 1st of April 2022 (1-4) and for a simulation that started on the 1st of October 2021 (1-10). The latter allows for an adaptation of the lake surface temperature to the actual weather, as simulations have started 6 months before the actual period of interest. Also, the `LAKE_LTA_NEW.nc` cold start tertial values in dark blue are plotted as horizontal lines (refer to section 2.5).

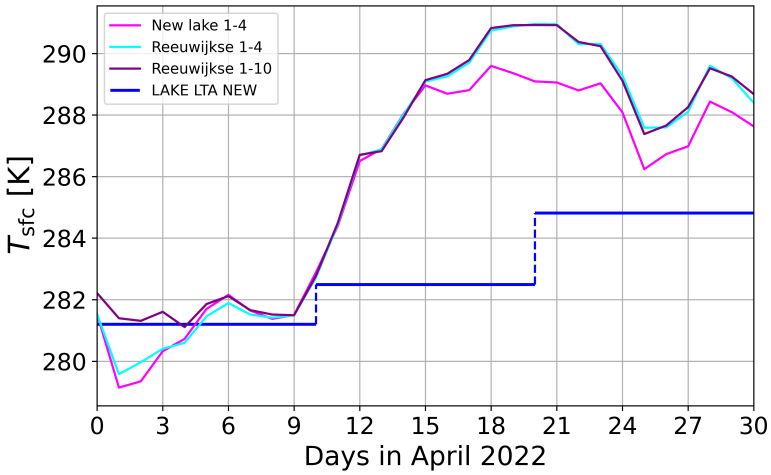

Figure 5.7: Illustration of the spin-up period for the new lake introduced on April 1st, 2022, in the HCLIM system. The new lake is a grid cell in which a land area is replaced by a lake with an experimental start at 1-4. Reeuwijkse 1-4 is an existing lake with a similar depth as the new lake, with an experimental start at 1-4. Reeuwijkse 1-10 is the result of a simulation that started half a year before the period shown. This comparison aims to show 1) the impact of the start time of the simulation on the modeled lake surface temperature, 2) the presence of a cold start of existing lakes at the start of an experiment, and 3) the aligned pattern for the lake surface temperature for the new and neighboring existing lake.

We learn from figure 5.7 that throughout April the new and existing lakes follow the same temperature curve. On April 1st, the water surface temperature received a value of 281.203 K from the input file, for lat-lon (51°N,5°E) at a 2-meter depth. Now, for both the new lake and Reeuwijkse, the water surface temperature averaged over the entire first day is 281.535 K, which is 0.302 K higher than the initialization value at $t = 0$, which might be due to heating during the day. The other experiment started in October, has 282.20 K as a resulting value for the lake surface temperature on April 1st. This deviates 1 K from the initialization value from the input file on April 1st.

From this we conclude existing lakes receive a cold start when an HCLIM simulation starts, using initial conditions from `LAKE_LTA_NEW.nc`, but also that the estimation of the cold start value for April 1st is fairly close to the resulted value from the Reeuwijkse experiment that started at 1 October 2022. However, this appears to be less true as the days in April proceed, which might be due to different atmospheric forcing, and is perhaps just a coincidence for these specific simulations.

In any case, this pre-study indicated the lack of a spin-up period for the regular experiments did not substantially bias the model results.

5.5. Processing methods

To interpret the impact of local changes in land use on the local climate, steps to process the data have been taken. The variables which are investigated are provided in table 5.2

For the experiments running multiple months from April 1st 2022 to October 1st 2022, statistics of some variables are calculated. The statistics include the daily and monthly means, maxima and minima, calculated for the night (00h-06h), morning (06h-12h), afternoon (12h-18h), evening (18h-24h), and full days (00h-24h). For some variables, the diurnal cycle is split into nighttime (18:00-05:59) and daytime (06:00-17:59). With this, the daily, monthly or periodic mean differences between the different surface types can be assessed.

Variable name	**Variable code**	**Units**	**Height (m)**	**Output frequency**
Surface Temperature	ts	K	0	1 hr
Near-Surface Temperature	tas	K	2	1 hr
50 meter Temperature	ta50m	K	50	1 hr
Near-Surface Wind Speeds	sfcWind	m/s	10	1hr
Northward Near-Surface Wind	vas	m/s	10	1hr
Eastward Near-Surface Wind	uas	m/s	10	1hr
Specific humidity	huss	g/m3	2	1 hr
Sensible heat flux	huss	W/m2	0	1 hr
Latent heat flux	huss	W/m2	0	1hr
Shortwave radiation	rsds, rsus	W/m2	0	1 hr
Longwave radiation	rlds, rlus	W/m2	0	1 hr
Roughness length of the vegetation	Z0	m	0	1hr
Soil moisture content of upper layer	mrso L01	kg m-2	0	6 hr
Mean water column temperature	SFX.TMNW	K	in lake	15 min
Mixed layer temperature	SFX.TWML	K	in lake	15 min
Lake bottom temperature	SFX.TBOT	K	in lake	15 min
Surface temperature	SFX.TSFC	K	in lake	15 min
Boundary layer height	SFX.HBL	m	in lake	15 min
Mixed layer height	SFX.HML	m	in lake	15 min

Table 5.2: An overview of the model variables processed in this research, resulting from the HCLIM and SURFEX system, with its variable code, units, projected height, and output frequency.

Three variables that have been indicated to be directly related to the living conditions for mosquitoes around wetlands and lakes are the surface temperature T_{sfc} [K], the atmospheric temperature at 2 meters T_{atm} [K], and the specific humidity at 2 meters q_{v} [g/kg] (refer to section 5.1.1). To explain changes in these variables, the focus lies on near-surface properties such as wind speed, turbulent fluxes, and radiation fluxes.

The wind direction is not directly given and obtained through the Eastward and Northward Near-Surface Wind Speeds, by:

$$\text{sfcWindDir} = \frac{360(\arctan2)(uas, vas) + \pi}{2\pi} \tag{5.1}$$

In this definition, a wind direction of 0 and 360 degrees corresponds to a northerly wind, 90 degrees corresponds to an easterly wind, 180 degrees corresponds to a southerly wind, and so on.

To further investigate the effect of wetlands instead of crops on the model results, we will look at the soil moisture content and roughness length. The upper layer of the soil moisture is 1 cm.

For the FLake experiments, the SURFEX output settings need to be modified manually in the system, leading to 15-minute output of some FLake-related variables described in section 2.4. With this, the temperatures in the water column are further explored and differences will be explained with the aid of the surface energy balance. To indicate the differences between lake depths and their effect on the diurnal temperature cycle of the surface temperature, the new lake (L) is compared with the nearby Reeuwijkse Plassen (R) and Vinkeveense Plassen (V). Further information about these lakes is provided in table 5.3, such as the grid cell coordinates, lake fraction, horizontal distance from L, and estimated lake size. Also, comparing these lake locations aid in understanding the initialization of HCLIM simulations and the spin-up period, concerning new and existing lakes.

	New lake (L)	**Reeuwijkse Plassen (R)**	**Vinkeveense Plassen (V)**
Coordinates (lat,lon)	(52.0700,4.5815)	(52.0403,4.7616)	(52.2346,4.9664)
Lake fraction (%)	100	67	70
Lake depth (m)	2	1.7	12
Δx **to new lake (km)**	n.a.	13	32
Estimated lake size (ha)	70	85	90

Table 5.3: An overview of the lake and location specifications encompassing the coordinates, fraction of inland water (%), lake depth (m), horizontal distance (km), and estimated lake size.

As a reference, the initialization values for the new lake and Reeuwijkse plassen are provided in figure 5.8a and for the Vinkeveense Plassen in figure 5.8b.

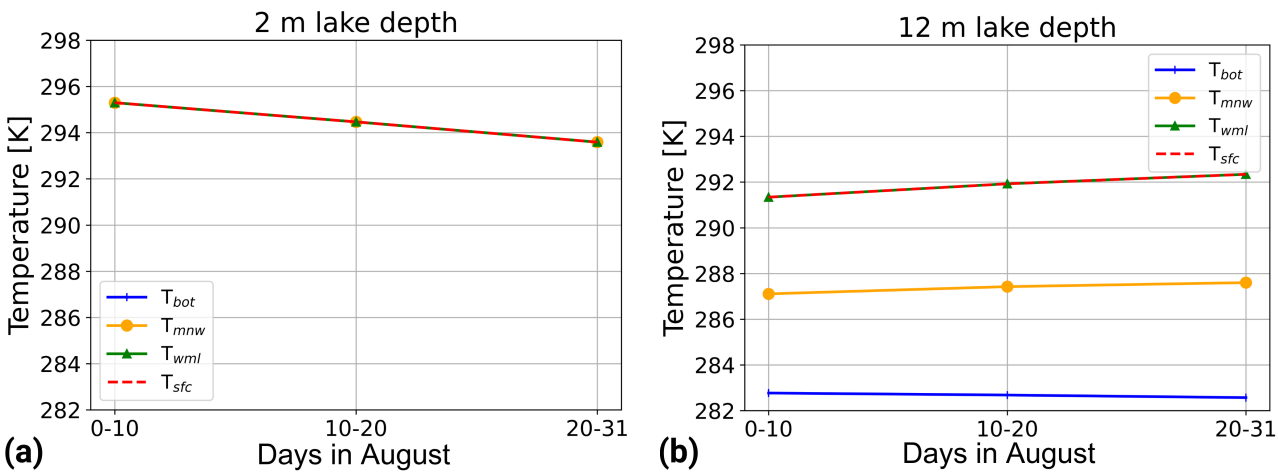

Figure 5.8: Initial conditions from `LAKE_LTA_NEW.nc` for the bottom temperature T_{bot} , the mean water column temperature T_{mnw} , the mixed layer temperature T_{wml} and lake surface temperature T_{sfc} from 1-10 August, 10-20 August and 20 to 31 August in the middle of the Netherlands (51°N,5°E), which apply to the (a) 2-meter deep new lake and Reeuwijkse Plassen and (b) for Vinkeveense Plassen.

6

Results and discussion

In section 6.1, the model outputs of the temperatures at the ground surface T_{sfc} , the lowest model level T_{atm} , the specific humidity q_{v} , and the horizontal wind speeds U_{spd} for the different experiments will be presented and discussed, as these variables interfere directly with mosquitoes' living conditions. Section 6.2 describes the effect of different surface types on the turbulent and radiative fluxes encompassing the surface energy balance (SEB). To demonstrate the effect of different surface types on the SEB, we will elaborate on surface type properties such as albedos, and stomatal resistance. Next, the findings of 6.2 will be related to T_{sfc} ,T_{atm} , T_{50m} , and q_{v} in section 6.3. Lastly, the case study will focus on the initialization of new lakes and its effect on the diurnal water column temperatures in section 6.4. To easily refer to the simulations with different surface types, L is used for the lake, C for the crops/control, and W for the wetland.

6.1. Temperatures, specific humidity and wind speed

6.1.1. Temperature

Figure 6.1 shows the time-mean difference for the lake as compared to the crops over the period of April 1st, 2022 to October 1st, 2022, for the region surrounding the land use change area outlined in black for T_{sfc} (fig. 6.1a) and T_{atm} (fig. 6.1b). The presence of a lake reveals a time-mean difference of 2.4 K for the surface temperature in the center of the lake. The atmospheric temperature at the lowest model level of 2 m (T_{atm}), shows a smaller time-mean difference of 0.65 K. These results indicate that the effect of changing surface types becomes smaller for increasing height, but the temperatures are on average higher above the lake than above crops.

For both T_{sfc} and T_{atm} a time-mean difference northwest of the lake is observed from the model results, of 0.6 K and 0.25 K respectively. Another noteworthy finding is the significant rise in average temperature at about 50 meters (T_{50m}) to the northeast of the lake, with temperature variations extending up to 50 kilometers from the initial land use change. However, this effect is very weak with a time-mean lake minus crops difference of 0.06 K and is not shown here (see figure C.1). A more detailed analysis of these findings will be given in section 6.3, after discussing the model results of other variables.

A similar simulation has been done for wetlands, indicating the effects of a wetland area instead of an agricultural area, averaged over the 1 April 2022 to 1 October 2022 period. Temperature differences are much smaller than for the lake experiments (not shown here, see figure C.3). For

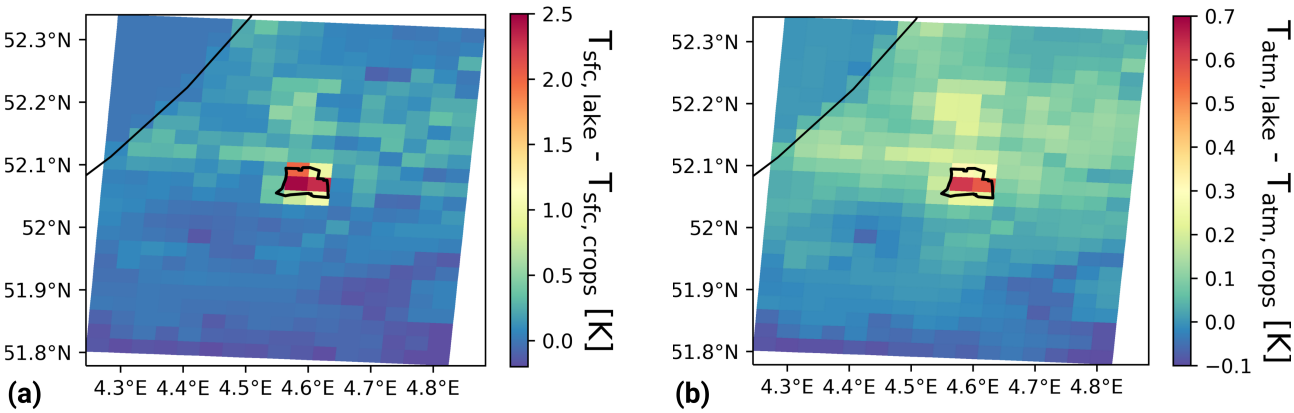

Figure 6.1: The time mean temperature difference between the simulations with lakes and crops at the surface for (a) T_{sfc} and (b) T_{atm} , over a period from 1 April 2022 till 1 October 2022. A positive value indicates a higher temperature for the simulation with the lake as compared to the simulation with crops.

all results that do not involve color maps, like figure 6.1, our focus will be on the HCLIM grid cell positioned at the center of the lake, as outlined in Table 5.3. This approach allows us to highlight the most significant changes in variables, which are a direct result of encompassing land cover changes making up 100% of the grid cell.

As discussed when deciding upon the weather conditions of interest for the experimental set-up, there is an evident thermal relation to mosquitoes' living conditions (refer to section 5.1.1). We will now compare the temperature model results to these thermal relations. Figure 6.2 shows for T_{sfc} the daily means (6.2a) and daily minima (6.2b) from 1-06-2022 till 1-10-2022. Similarly, for the T_{atm} , the daily means and minima are provided in figures 6.2c and 6.2d.

The pronounced peaks in T_{sfc} , serve as a clear indication of extreme heat conditions (figure 6.2a). The daily mean of T_{sfc} of the lake is generally higher than it is for wetlands and crops, except in the week of 13 July 2022 and 10 August 2022, when the days were extremely hot. Around July 19th, 2022, the mean surface temperature of the crops and wetlands becomes 5 K warmer than the mean lake surface temperature (see figure 6.2a). However, during the night, the T_{sfc} of vegetation cools down extremely, dropping almost daily below the 290 K line.

The minimum surface temperature of the lake consistently stays above the 290 K threshold for an uninterrupted period of 13 weeks, spanning from 15 June 2020 to 14 September 2022, as shown in figure 6.2b. During this time, the minima only surpassed the 301 K line in the week of 17 July. In contrast, the wetland and crops model results reach this threshold twice during the hotter periods, as illustrated in Figure 6.2b. The relatively stable lake surface temperature can be attributed to the high thermal capacity of the lake. This characteristic leads to a slower response to extreme temperature fluctuations, particularly evident during severe heat events. A concern regarding the enhancement of mosquito development is that the model results reveal water surface temperatures that remain consistently above T_{min} .

The daily mean air temperatures (T_{atm}) above the lake, wetland, and crops exhibit closer proximity to each other than the daily mean surface temperatures (refer to figures 6.2a and 6.2c). The T_{atm} values for the lake, wetland, and crops fluctuate between the 290 K and 301 K lines for the majority of the time, which favors mosquito development and potential viral establishment. Figure 6.2 shows that in the lake simulation, the minimum T_{atm} fluctuates around the 290 K line, whereas for the wetland and crops, the minimum T_{atm} is consistently below 290 K for the majority of the time. This suggests that during nights, the atmospheric temperature above the wetland simulation

is typically too low for mosquitoes, only surpassing T_{min} during heatwaves.

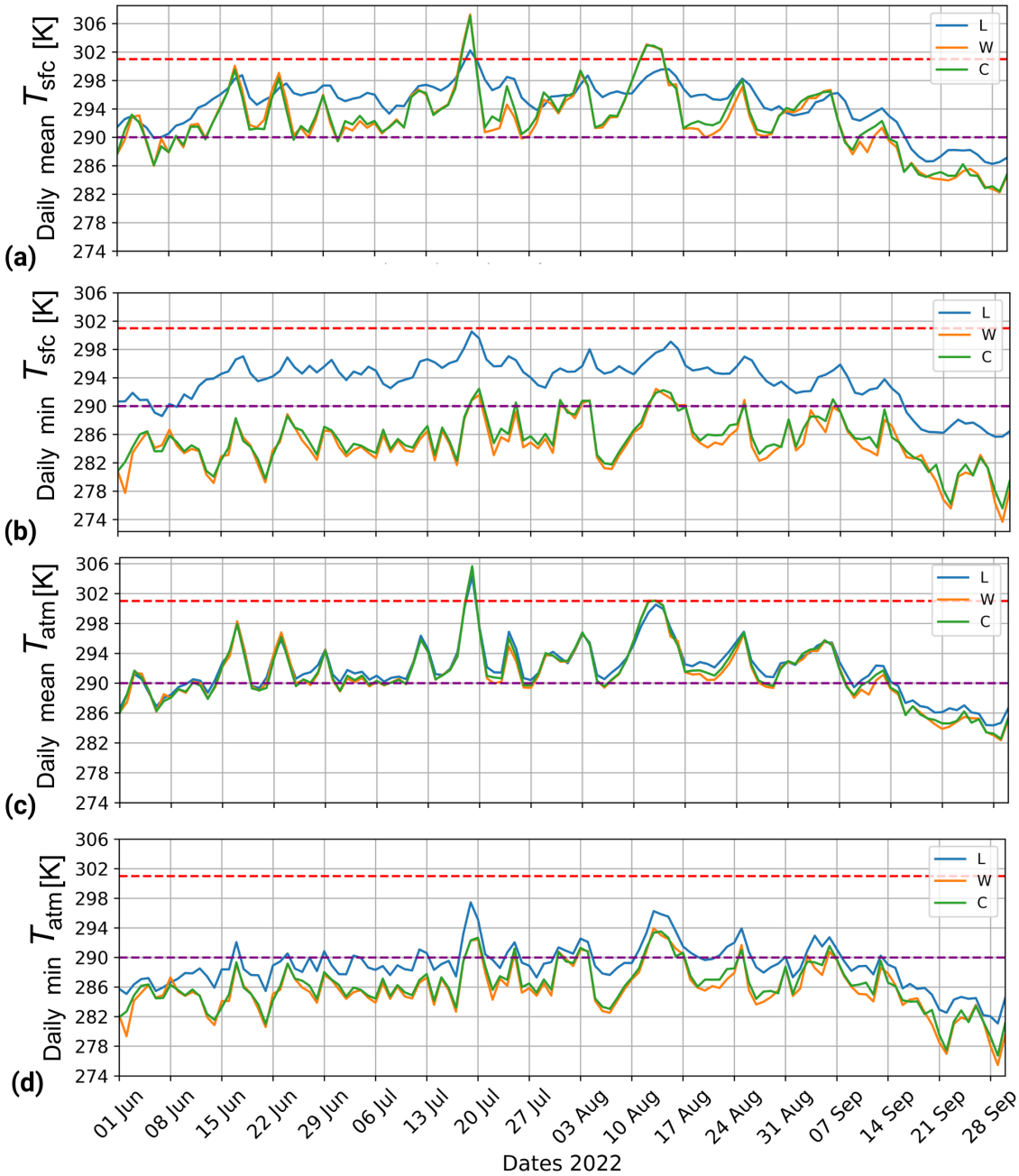

Figure 6.2: The daily (a) means and (b) minima of the surface temperature (T_{sfc}) and the daily (c) means and (d) minima of the atmospheric temperature (T_{atm}), for a period from June 1st, 2022 till October 1st, 2022 at 1 grid cell point (52.07°N,4.58°E), for lake (L), wetland (W) and crops (C). The horizontal purple line indicates the $T_{min} \approx 290$ K line (17°C) and the red line the $T_{opt} \approx 301$ K (28°C) (refer for their meanings to section 5.1.1).

To further study the Diurnal Temperature Range (DTR), figure 6.3a shows the monthly means of T_{sfc} during daytime (06:00-17:59) and figure 6.3b during nighttime (18:00-05:59) local time. The daytime mean T_{sfc} shows rather small different values for the lake, crops and wetland simulation. The lake surface temperature becomes -3 K smaller than the land surfaces in August (figure 6.3a). The opposite turns out to be true during night time, where T_{sfc} of the lake remains about 7 K higher than of wetland and crops throughout the period (figure 6.3b). Comparing daytime and nighttime values with each other, the DTR in T_{sfc} is more pronounced for wetlands and crops, reaching up to

10 K in August, whereas the monthly average values for the lake show minimal differences.

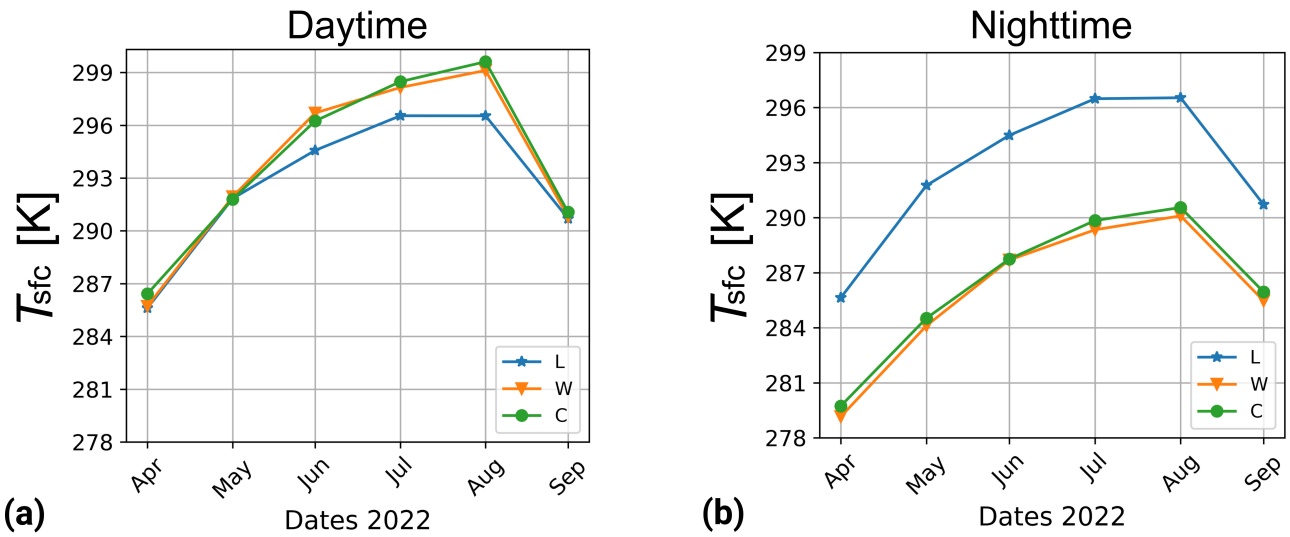

Figure 6.3: The monthly averages over 1 grid cell in the middle of the area of the surface temperature for the simulations with surface types lake (L), wetland (W) and original land use (C) from April 2022 to September 2022, for the (a) daytime and (b) nighttime.

For T_{atm} , the monthly averages for the different simulations are plotted in figure 6.4. The lake simulations exhibit 1 K higher air temperatures compared to the wetland and crops during the summer months, becoming near-zero in spring (fig. 6.4a). However, during nighttime, air temperatures above the lake are 2 K higher compared to wetlands and crops (fig. 6.4b). Between the wetland and crop vegetation types, the crop simulation shows 0.2 K higher air temperature values and negligibly small differences during the day.

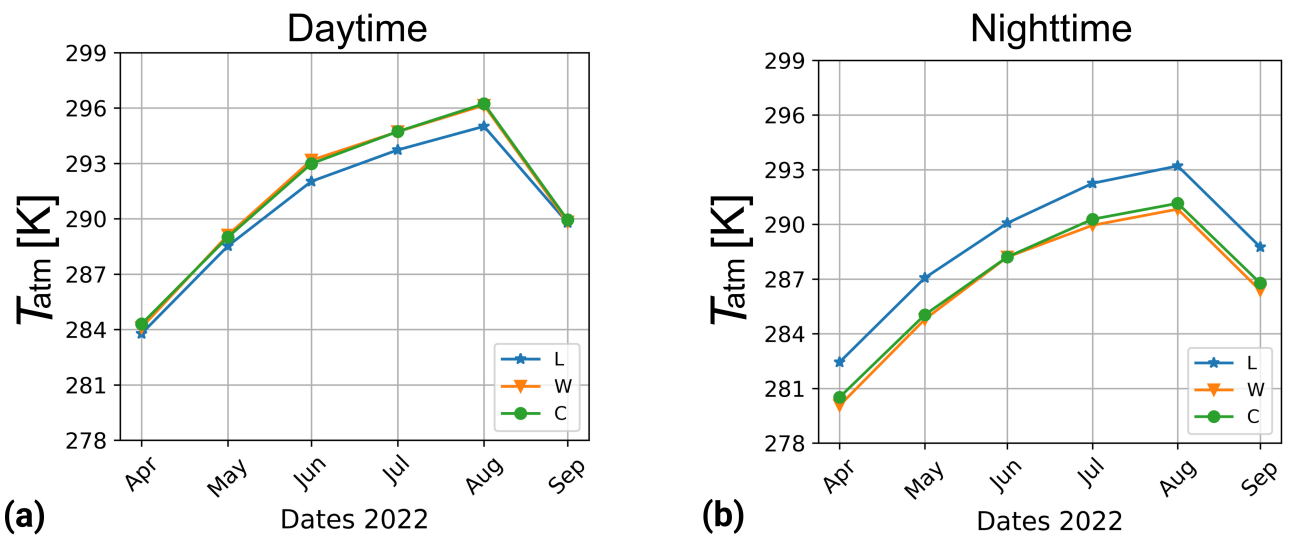

Figure 6.4: The monthly averages over 1 grid cell in the middle of the area of the atmospheric temperature on the lowest model level of 2 meters for the simulations with surface types lake (L), wetland (W) and original land use (C) from April 2022 to September 2022, for the (a) daytime and (b) nighttime.

Surface and atmospheric temperature fluctuations are directly related to changes in turbulent heat fluxes, following equation 2.18a, and the wind behavior, which will be further discussed in later sections.

6.1.2. Specific humidity

Although the identified relation of humidity (and precipitation) on mosquito development is not as established as the thermal relation, it is profoundly present (Brown et al., 2023). Therefore, we discuss the model results for the specific humidity at the lowest model level of 2 meters above the surface. Again, the time mean difference for the simulation with the lake as compared to the crops is plotted for the region surrounding the anticipated land use change (see figure 6.5a). The model shows a time-mean difference of 1.0 g/kg in the middle of the area, with a smaller though noticeable q_v difference next to the lake.

The specific humidity q_v rises over the summer up until September, for all surface types. This can clearly be seen in figure 6.5b, indicating the monthly means. For every month, the specific humidity above lakes is higher than over wetland and crops, since just above the lake the air is at saturation. In July and August, the air above the lake is moister than the air above the crops by about 1.4 g/kg. This is mainly attributed to the extreme dips in specific humidity during heatwaves between 13-20 July and 10-17 August above the wetlands and crops (not shown here, see appendix C.4). The specific humidity is directly dependent on the latent heat flux, and implicitly on the soil moisture levels, according to equation 2.18b. Some supplementary physical explanations on specific humidity fluctuations will therefore be outlined in section 6.2.2 and section 6.3.

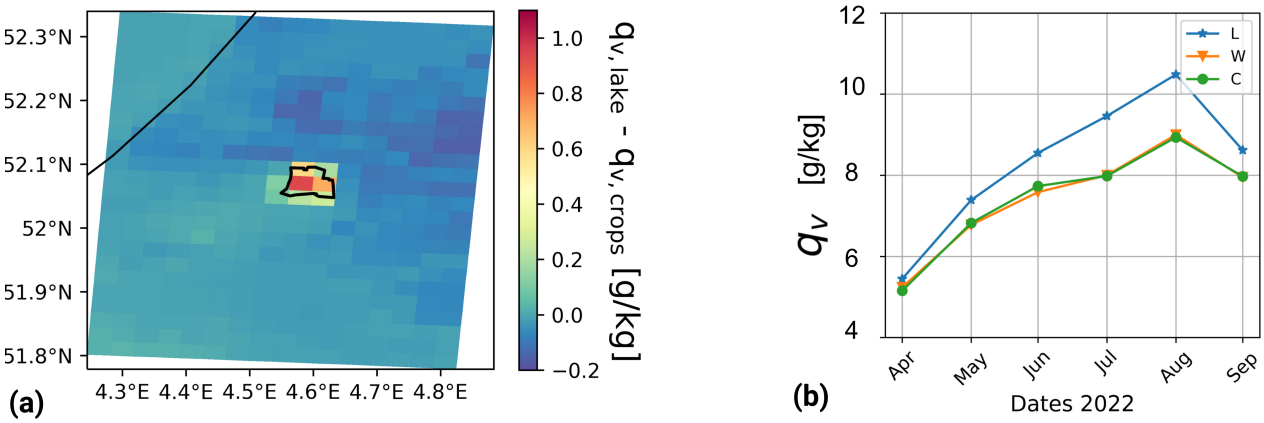

Figure 6.5: (a) The time mean specific humidity difference between the simulations with lakes and crops at the surface over a period from 1 April 2022 till 1 October 2022. A positive value indicates a higher specific humidity for the simulation with the lake as compared to the simulation with crops. (b) The monthly averages over 1 grid cell in the middle of the lake of the specific humidity for the lowest model level for the lake (L), wetland (W) and original land use (C) from April 2022 to September 2022, averaged over a full day.

6.1.3. Wind speed

The wind speeds on the lowest model level are at a 10-meter height. Figure 6.6a shows the time mean differences for the lake simulation as compared to the crops. Distinct differences are foremost present in the near vicinity of the lake. The wind speed model results are up to 1.2 m/s higher over the lake center and ranging from 0.2-0.6 m/s on a 5 km range, compared to the crops. The time-mean wind direction is prevailing north-west (see figure 6.6b).

On a monthly average, the daytime wind speed over the lake compared to wetland and crops is 1 m/s higher (figure 6.7a). This difference is especially visible during the night, when the wind speeds over the lake reach up to 1.5 m/s higher in April and June (figure 6.7b). This is mainly due to a relatively high drop in wind speed above the wetland and crops during nighttime. Unlike the

lake area, the wind over the wetland is very similar to the crop area. These differences in horizontal wind speeds can be explained by the turbulent fluxes and the differences in roughness lengths of the surface types, which will be analyzed more in-depth in section 6.3.

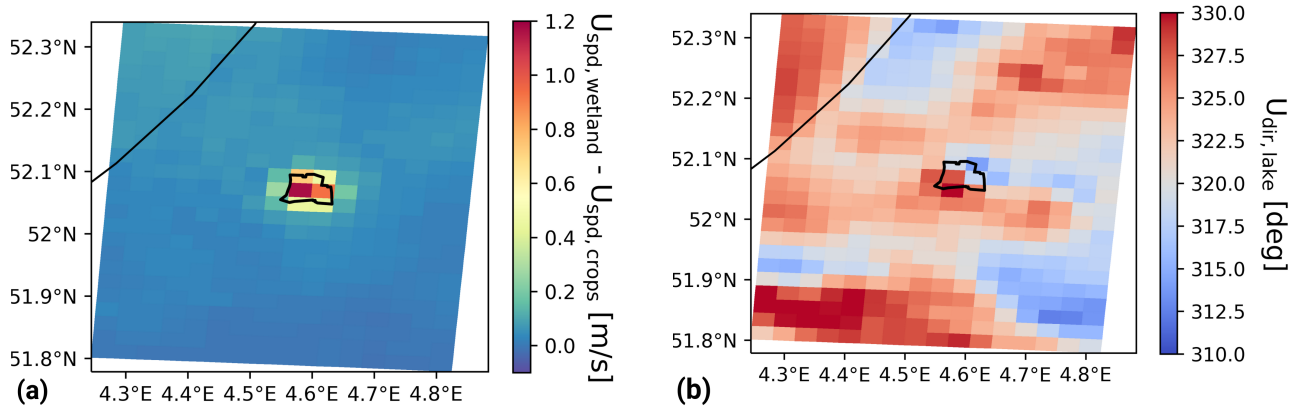

Figure 6.6: (a) The time mean wind speed difference between the simulations with lakes and crops at the lowest model level of 10 meters above the surface over a period from 1 April 2022 till 1 October 2022. A positive value indicates a higher wind speed for the simulation with the lake as compared to the simulation with crops. (b) The time mean wind direction for the simulations with the lake 10 meters above the surface over a period from 1 April 2022 till 1 October 2022.

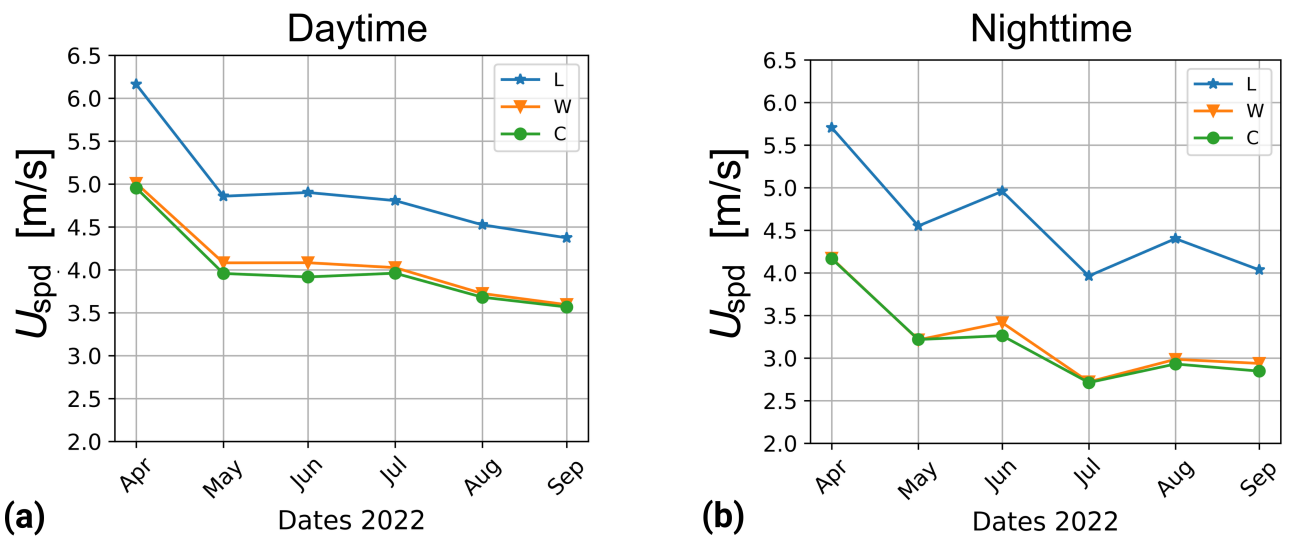

Figure 6.7: The monthly averages over 1 grid cell in the middle of the area of the wind speed on the lowest model level of 10 meters for the simulations with surface types lake (L), wetland (W) and original land use (C) from April 2022 to September 2022, for the (a) daytime and (b) nighttime.

6.2. The changing surface energy balance

In this section, a more detailed exploration of the surface energy balance will be undertaken, demonstrating the impact of different surface-type properties. Next, a detailed analysis of the relation of the surface energy balance with temperature, humidity, and wind speed, is given in section 6.3.

6.2.1. Sensible heat flux

The sensible heat flux is the transfer of heat between the Earth's surface and the atmosphere that directly influences its temperatures. To illustrate the impact of land use change on the time-averaged sensible heat flux (SHF), figure 6.8 shows the presence of a lake induces a time-mean decrease of approximately 30 W/m^2 as compared to the crops.

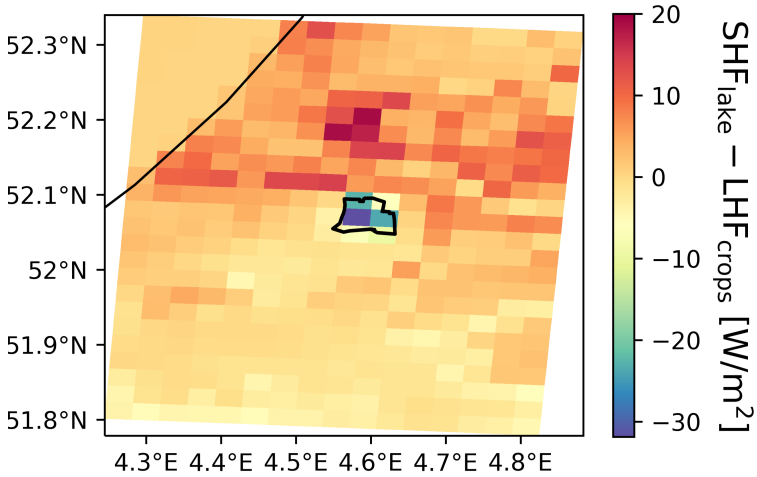

Figure 6.8: The time mean sensible heat flux difference between the simulations with lakes and crops over a period from 1 April 2022 till 1 October 2022. A positive value indicates a higher SHF for the simulation with the lake as compared to the simulation with crops.

On the contrary, north of the lake, the model results show that the presence of the lake modified the sensible heat flux by an amount of about 20 W/m^2 (further discussed in section 6.3). The local effect for the wetland relative to the original crops is near zero (not shown here, see C.3c).

The monthly averages of the sensible heat flux are plotted for daytime (figure 6.9a) and nighttime (figure 6.9b). Here, a distinct higher sensible heat flux over wetlands and crops is observed, compared to the lake. This difference reaches 130 W/m^2 in June and July. On the contrary, during the nighttime, the sensible heat flux over crops and wetland drops and becomes negative (~ -25 W/m^2). If a lake is present, the nighttime SHF remains small but positive (~ 25 W/m^2). This implies that the lake continuously heats the atmosphere during the day- and nighttime for the simulation period.

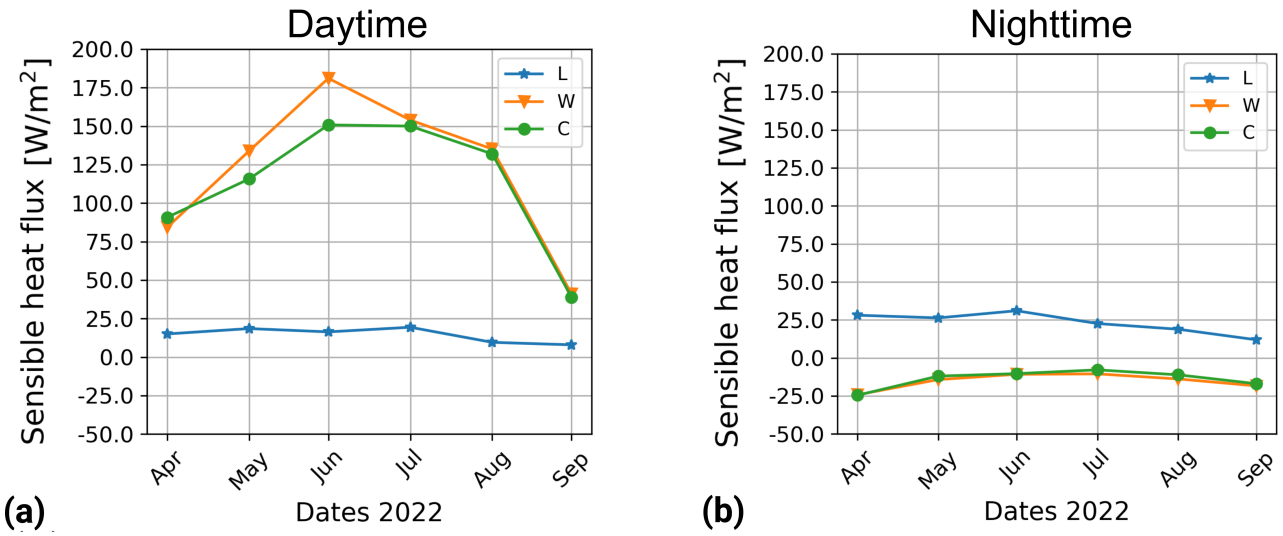

Figure 6.9: The monthly averages over 1 grid cell in the middle of the area of the sensible heat flux for the simulations with surface types lake (L), wetland (W) and original land use (C) from April 2022 to September 2022, for the (a) daytime and (b) nighttime.

6.2.2. Latent heat flux

The model output shows a higher time-mean latent heat flux above lakes compared to crops, up to 35 W/m^2 (see figure 2.12).This can be explained by the lake being saturated with water, which leads to evaporation. North from the area where land use change is imposed, the presence of the lake results in a 30 W/m^2 decrease in LHF, as compared to simulation with crops at this area.

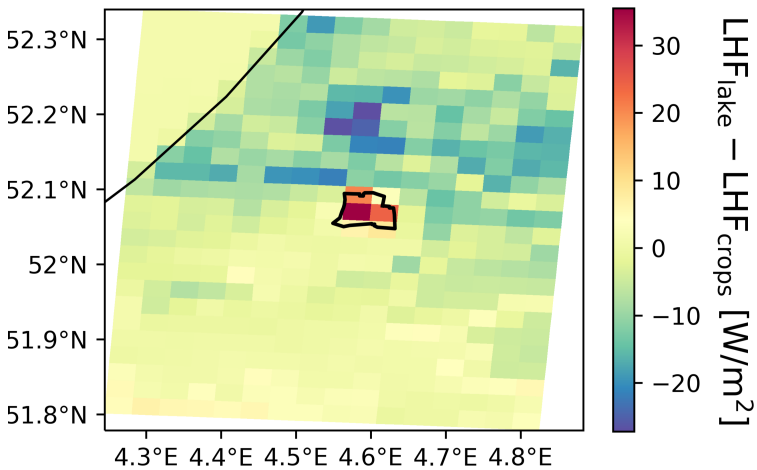

Figure 6.10: The time mean latent heat flux difference between the simulations with lakes and crops over a period from 1 April 2022 till 1 October 2022. A positive value indicates a higher LHF for the simulation with the lake as compared to the simulation with crops

Figure 6.11 shows the daytime (fig. 6.11a) and nighttime (**??**b) latent heat flux. The latent heat release levels for the lake rise over the summer and peak around July.

The latent heat flux is directly related to the vertical humidity gradient. As air just above the lake is saturated with water vapor, the LHF is considerably higher for the lake during day- and nighttime (see figure 6.11). During the night, the lake surface temperature cools due to radiative loss and positive sensible heat flux, as has been shown in figure 6.9. Still, the lake remains an important source of humidity as can be seen from the remaining positive LHF.

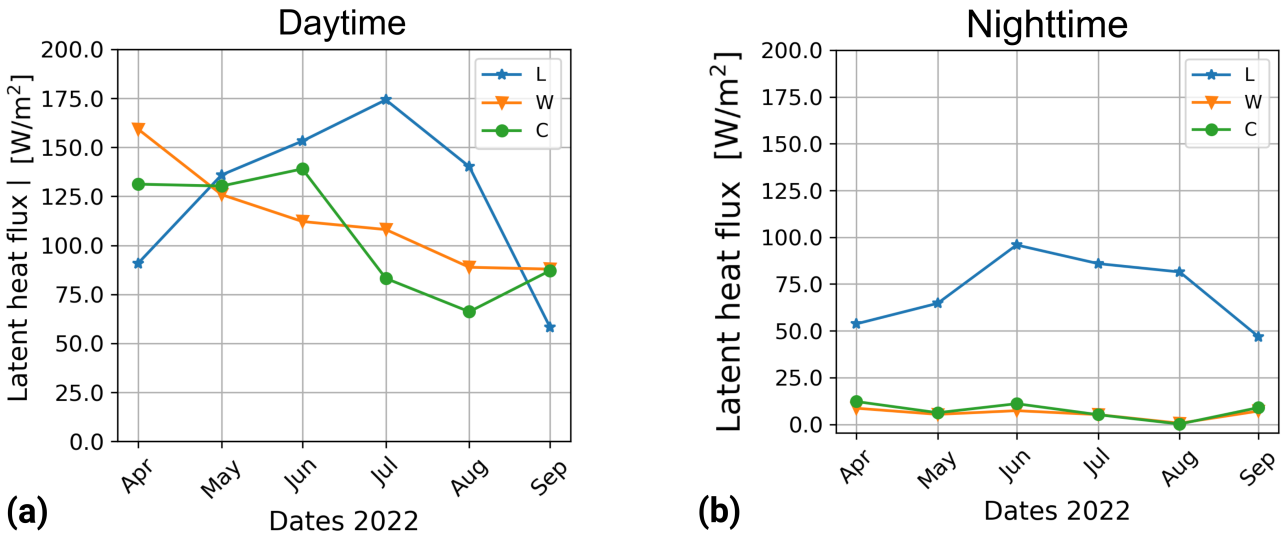

Figure 6.11: The monthly averages over 1 grid cell in the middle of the area of the latent heat flux for the simulations with surface types lake (L), wetland (W) and original land use (C) from April 2022 to September 2022, for the (a) daytime and (b) nighttime.

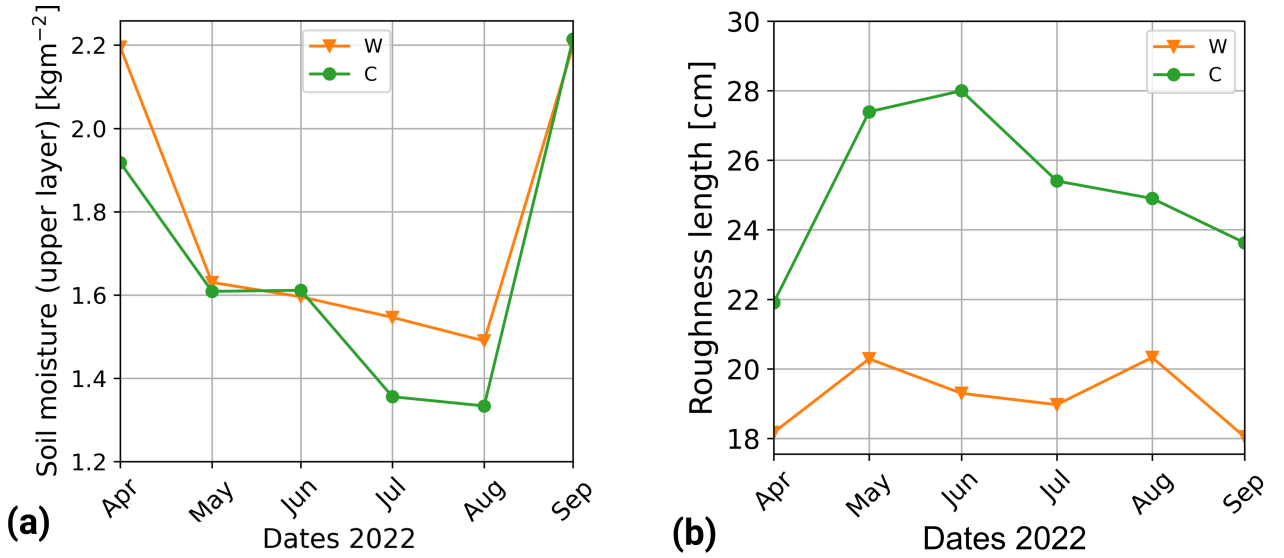

Figure 6.12: The monthly averages over 1 grid cell in the middle of the area of (a) the upper soil layer moisture content and (b) roughness length for the simulations with surface types lake (L), wetland (W) and original land use (C) from April 2022 to September 2022.

According to equation (2.12), the latent heat flux is inversely related to the aerodynamic resistance of the latent heat transport r_{aV} (2.14), the vegetation resistance r_{veg} (2.16) and soil resistance r_{soil} (2.17). The observed higher wind speed over the lake than over vegetation as in figure 6.6, leads to a smaller r_{aV} over the lake than over the vegetation, hence increasing the LHF. As $r_{s,min}$ is lower for wetland than for crops, this decreases r_{aV} over wetland (refer to table 5.1). Illustrated in figure 6.12a, the soil moisture content indicates a a higher moisture level for the upper layer (1 cm) for the wetland wetland. All of these factors imply less resistance to evaporation via the stomata for wetland, than for crops. In turn, this leads to a smaller r_{veg} , which increases the LHF. This observation may provide insight into the elevated latent heat flux above wetlands during the months of April, July, and August. However, this effect contradicts the observed pattern in other months. The total soil moisture content is higher over crops (shown in figure C.5). As vegetation and soil physics comprehend extensive physical concepts, this can further be analyzed by looking into the

actual vegetation height and the factors of the Jarvis parametrization embedded in equation 2.16.

Relation to roughness length and horizontal wind speed
The surface roughness length affects the momentum transfer in the lower atmospheric layer. A higher roughness length $Z0$, hence a rougher surface, leads to more turbulent fluxes, generally leading to a higher vertical momentum flux. The roughness length of the lake is fairly small, especially compared to the wetland and crops, which diminishes the momentum flux. In turn, a lower roughness length means less turbulent drag, so more wind.

The roughness length of the crops is higher than that of the wetland. It is hypothesized the vegetation height for crops is higher than for wetlands, especially in the growing season (April- June), leading to higher roughness length. The data package ECOCLIMAP-SG allows for further analysis.

6.2.3. Shortwave radiation

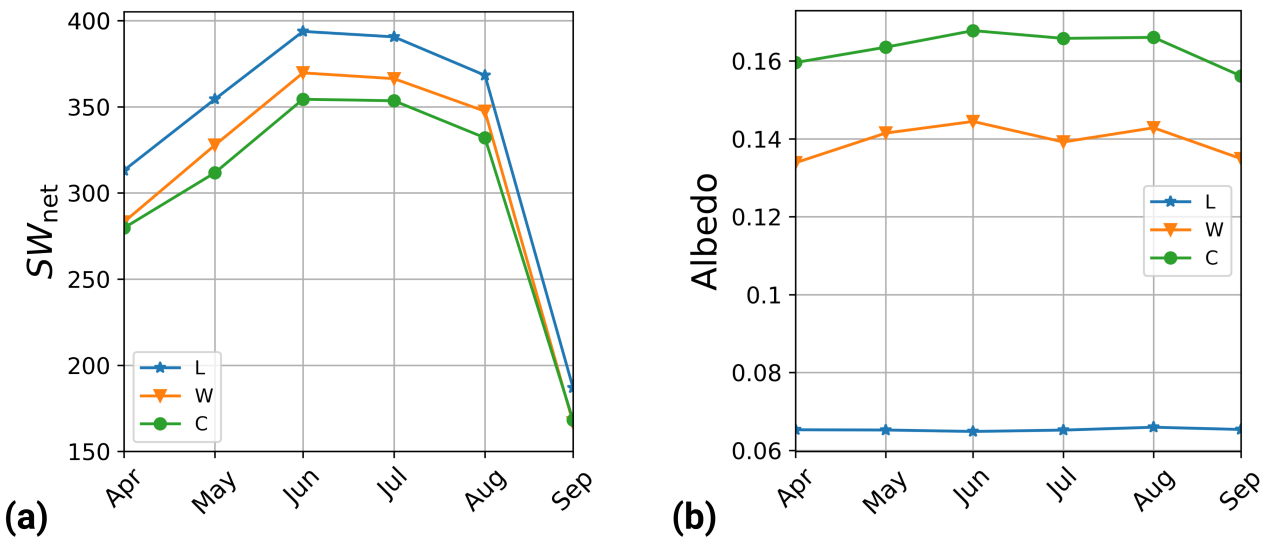

Figure 6.13: The monthly averages over 1 grid cell in the middle of the area of the (a) SW_{net} radiation and (b) albedo for the simulations with surface types lake (L), wetland (W) and original land use (C) from April 2022 to September 2022, during daytime.

Incoming shortwave radiation experiences its peak levels at the top of the atmosphere. We see that the maximum SW_{net} is found in June, primarily because the sun reaches its highest position in the sky, as plotted in figure 6.13a. Following June, the intensity of shortwave radiation gradually declines in tandem with the changing sun angle. Throughout the spring and summer, the net shortwave radiation exhibits a distinct surface-type contrast, with the lake absorbing the most shortwave radiation. The notable variations over different surface types are present due to the different albedos (see figure 6.13b). For the land points, we observe relatively high albedos, with values of about 0.162 for the crops and 0.14 for the wetland. According to the model results, the lake has a low albedo of approximately 0.066. Moene and Van Dam (2014) presents values of 0.1 - 0.2 for wet soil, 0.2 - 0.4 for dry soil and 0.05 for water areas. The HCLIM model values area of the same order. The wetland shows higher moisture levels at the upper layer than the crops (refer to figure 6.12a), indicating the lower value of the albedo from the model results (figure 6.13b).

6.2.4. Longwave radiation

Upward longwave radiation is closely linked to variations in surface temperature (T_{sfc}). It tends to increase during the spring and summer months and decreases as September approaches, as seen in figure 6.14. A similar diurnal pattern is observed for longwave radiation as for the surface temperature (refer to 6.3a and 6.3b).

It is clear from the model results that during the day in the summer months (June - August), the LW_{up} for the lake is relatively smaller, due to the extremely fast heating of the land surfaces, most notably due to the higher temperatures for the latter during the day. This adds up to a maximum difference of -23 W/m^2 comparing the lake and crops during the daytime of August 2022. During the night, the LW_{up} is higher for lakes, again due to the heat capacity of lakes.

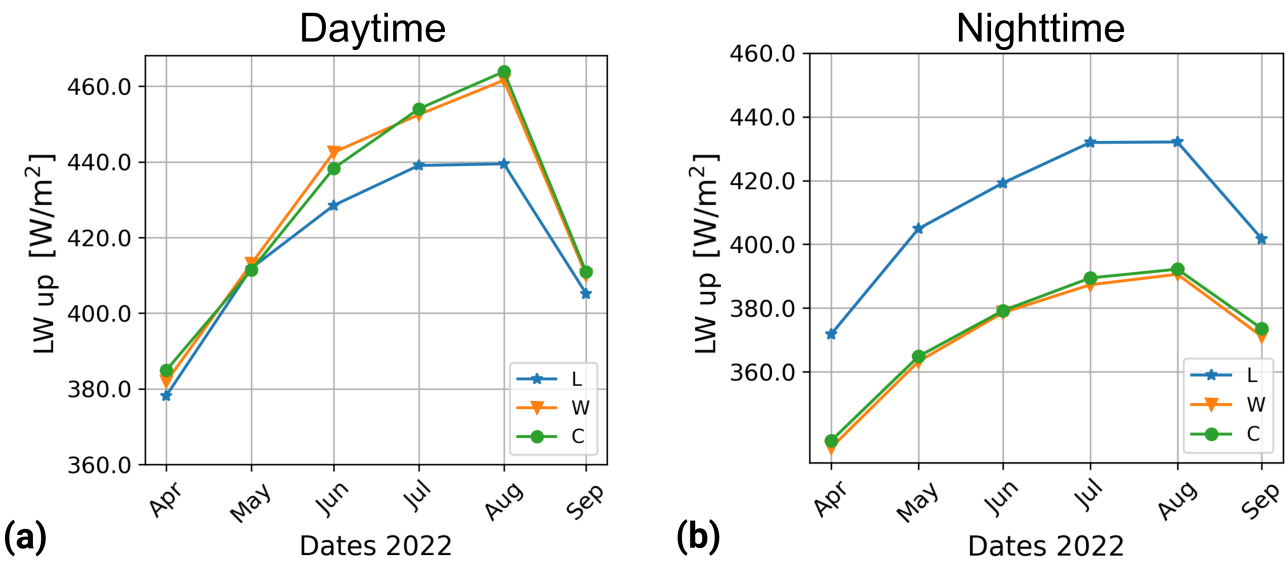

Figure 6.14: The monthly averages over 1 grid cell in the middle of the area of the longwave upwards radiation for the simulations with surface types lake (L), wetland (W) and original land use (C) from April 2022 to September 2022, for the (a) daytime and (b) nighttime.

6.3. Relations between prognostic variables and turbulent fluxes

We will now further analyze some results of the surface energy balance components more in-depth by comparing them to temperatures, specific humidity, and wind.

For color maps indicating the difference between the lake and crop simulations, the temperature shows a time-mean increase around 10 km north of the lake with differences in $T_{sfc} \approx 0.6$ K and $T_{atm} \approx 0.25$ K (see figures 6.1a and 6.1b). At the same location, the SHF showed a positive time-mean difference of 20 W/m^2 and the LHF a negative time-mean difference of -30 W/m^2 (see figures 6.8 and 6.10)

It is hypothesized that these phenomena occur due to horizontal advection of relatively warm and moist air downwind from the lake. The resulting negative q_v gradient downwind leads to a negative time-mean LHF. In turn, this might lead to a higher sensible heat flux (SHF). However, there are two indicators rejecting this hypothesis. First, the notable differences are predominantly observed upwind rather than downwind (refer to the northwest wind direction as visualized in figure 6.6b). Secondly, the rather small variations in the specific humidity do not suggest a reason for such a distinct decrease in latent heat flux (see figure 6.5). For these reasons, the hypothesis stating horizontal advection of warm and moist air as a source for the distinct upwind changes is rejected.

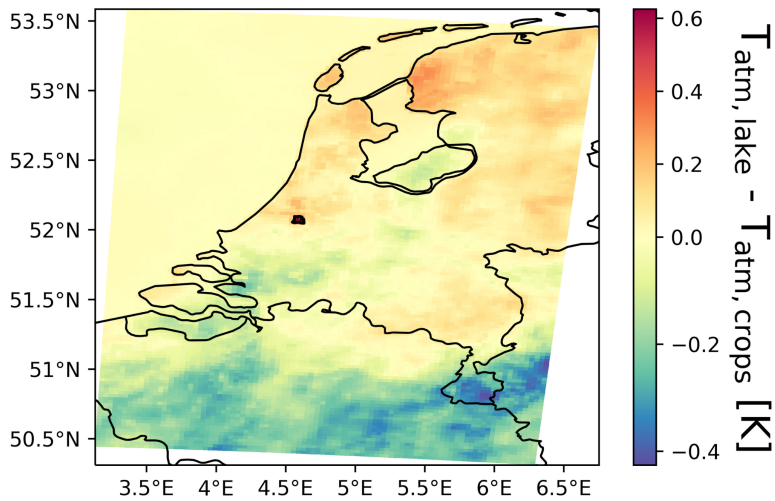

Figure 6.15: The time mean atmospheric temperature difference between the simulations with lakes and crops over a period from 1 April 2022 till 1 October 2022. A positive value indicates a higher temperature for the simulation with the lake as compared to the simulation with crops.

To further investigate this, the whole of the Netherlands is plotted for the atmospheric temperature in figure 6.15. Now, we observe these differences do not occur solely 10 km north of the lake, but throughout the whole domain. For example, in Friesland the time mean differences show a positive T_{atm} increase of 0.3 K, while in the south of Limburg there is a negative T_{atm} difference down to - 0.4 K. Also, the upwind differences are spotted for the wetland minus crop color maps, while locally much smaller differences are present (see figure C.3.

The lateral boundaries of the HCLIM model domain are fed with ERA5 data, providing a predefined outline of what weather events are expected to occur at various times. If a local change is implemented, like a lake, its effect on the model results can be noted throughout the entirety of the Netherlands. This finding could be due to the chaotic behavior of atmospheric flow, in which even the smallest perturbation in an initial condition leads to a completely different weather pattern at forecast time scales of a couple of days. The fact that the reference and perturbed runs are fed by the same lateral boundary conditions prohibits such a strong runaway effect. In the study by Boonekamp (2023), analogous chaotic patterns were identified on a significantly larger scale compared to the induced local land use changes, affirming this hypothesis.

Now the sensible heat flux is related to the vertical temperature gradient (refer to equation 2.13). We already found in section 6.1.1 that during the daytime, the air temperature (T_{atm}) above the lake is only slightly lower than above crops and wetlands (figure 6.1b). Moreover, the lake surface temperature exhibits less variation across time compared to crops and wetlands (figure 6.1b). Consequently, due to a relatively small vertical temperature gradient ($\partial T/\partial z$), the sensible heat flux remains rather small (about 15 W/m^2) during daytime at the lake surface. This is in contrast to wetland and crops simulation, showing clear diurnal fluctutation of the SHF and temperatures (figure 6.9). During the nighttime, the sensible heat flux above the lake remains positive, due to a persistent $T_{\text{sfc}} > T_{\text{atm}}$, leading to the warming of the air above the lake and vice versa, so the lake acts as a heat source to the atmosphere above.

Specific humidity changes in the atmosphere can partially be attributed to direct perturbations in the latent heat flux, through equation 2.18b. Because the lake skin surface is saturated with water evaporation, the rise in latent heat flux results in an increased water vapor density in the air and its immediate vicinity. Consequently, there is an increase in specific humidity right above the lake.

This explains why the time-averaged atmospheric specific humidity is higher with the presence of a lake than as compared to a land surface (figure 6.5a). This difference is particularly pronounced in July and August, directly corresponding to the contrast in latent heat flux, reaching a maximum average difference of about 80 W/m^2 (figure 6.5b).

6.4. Case study: observing the cold start initialization and diurnal cycle of FLake variables

In this section, the results of the experiments with extra FLake model output for the heatwave case study are explored (see the experimental set-up in section 5.3.2). In section 6.1 and 6.2, only the near-surface and surface variables are discussed. The elements making up the surface energy balance lead to heat flux into the ground or the lake G, as described in equation 2.6.2. This section explores the variations of the water column temperatures after a cold start initialization due to the net heating or cooling at the (water)surface-atmosphere interface as described by the FLake model (see section 2.4). This encompasses the temperature profiles within the mixed layer of the water column and the heat budgets (see equations 2.5 and 2.6 for the time-evolution of T_{mnw} and T_{wml} respectively), which are perturbed through the net flux.

In figure 6.16, the diurnal temperatures are plotted for the new lake (L) (figures 6.16a), the Reeuwijkse Plassen (R) (fig. 6.16c) and the Vinkeveense Plassen (V) (fig. 6.16d). Refer to table 5.3 for the characteristics of the lakes. In the right column of figure 6.16 the surface energy balances are shown for the respective lakes (figures 6.16b, 6.16d and 6.16f). Figure 5.8 in the pre-study section 5.4, reveals the cold start values for each lake in August. The cold start lake surface temperature for the one-day FLake experiment on 12-08-2022 is 4 K lower compared to the model results on 12-08-2022 of regular experiments starting on 1-04-2022. In the experiment with the spin-up period the temperature in the lake has been able to adapt to the prevailing local weather conditions, which is not captured by the climatological mean value applied in the cold start. This finding stresses the need for a spin-up period.

The temperatures present in the water column are the bottom temperature T_{bot} , mean water column temperature T_{mnw} , mixed-layer temperature T_{wml} and surface temperature T_{sfc} . The variation of the water column temperatures are the same as T_{sfc} over the diurnal cycle. The diurnal maximum difference for T_{atm} and T_{sfc} , are 7 K and 4 K respectively, as shown in figure 6.16a. For the Reeuwijkse Plassen (R), a similar pattern is depicted, showing the same curve for T_{bot} , T_{mnw} and T_{wml} (figure 6.16c). The surface temperature at $t = 0$ is 293.37 K for the Reeuwijkse Plassen, indicating again the cold start initialization of existing lakes by default in HLCIM (as described in the pre-study in section 5.4). However, the initial surface temperature of the FLake model output shows a slightly higher value of 294.41 K. It is unknown what the reason for these rather small differences is, and it might be attributed to yet undiscovered interpolation techniques for the time, depth, or spatial data points. The daily minima and maxima for the Reeuwijkse Plassen are almost twofold compared to the new lake (14 K for T_{atm} and 7 K for T_{sfc}). Due to the uncertainties regarding the effect of the cold start for water column variables, the temperature profiles and their relation to the surface energy balance (SEB) cannot be interpreted with absolute values, only relative to each other.

Noteworthy is that for the Vinkeveense Plassen, T_{bot} and T_{mnw} differ from T_{wml} . The bottom temperature seems almost independent of the diurnal cycle, and the mean water column temperature shows rather small variations. These model results are as expected since there is little mixing near the lake bottom for a 12-meter-deep lake like the Vinkeveense Plassen (figure 6.16e). In this case,

the $t = 0$ water surface temperature values are according to the initialization file (figure 5.8b). The difference between the daily minimum and maximum of T_{wml} is about 4 K for all lakes, and during this specific daily cycle on 12-08-2022, it seems not directly dependent on the visible differences in ground heat flux G across the different lakes (figure 6.16)

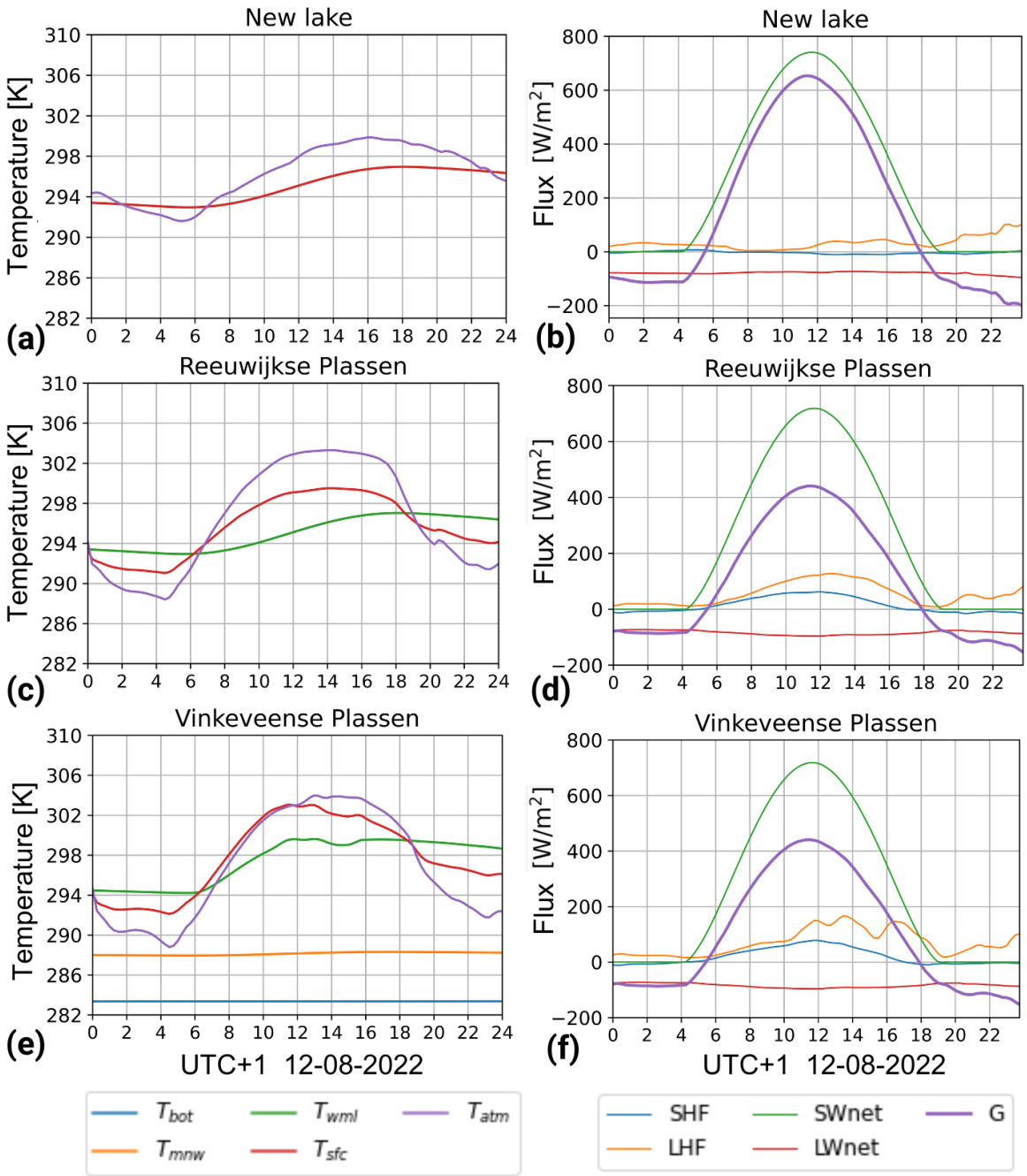

Figure 6.16: The left column displays the diurnal cycle of 12-08-2022 for the T_{bot} (blue), T_{mnw} (orange), T_{wml} (green), T_{sfc} (red) and T_{atm} (purple) for the (a) new lake, (c) Reeuwijkse plassen and (e) Vinkeveense Plassen. The right column shows the surface energy balance (SEB) of 12-08-2022 with SHF, LHF, SW_{net}, LW_{net} and the ground heat flux G for the (b) new lake, (d) Reeuwijkse Plassen and (f) Vinkeveense Plassen. In (a), T_{bot} ,T_{mnw} ,T_{wml} and T_{sfc} are identical and therefore do not show up as separate lines. The same holds for T_{bot} , T_{mnw} and T_{wml} in (b).

Another remarkable model result is the relatively consistent flux G of -100 W/m^2 in the first few hours, basically following LW_{net} with only minor perturbation effects of the surface temperature T_{sfc} and atmospheric temperature T_{atm} . In the new lake results, both T_{atm} and T_{sfc} exhibit a minor

diurnal cycle characterized by relatively low temperatures (see figure 6.16a), while the ground heat flux G peaks at the new lake (figures 6.16b, 6.16d and 6.16e). There is a rather small sensible heat flux at the surface of the new lake compared to the Reeuwijkse Plassen (fig. 6.16b and fig. 6.16d). This can be explained by the relatively high temperature gradient above the lake surface of the Reeuwijkse Plassen, as can be seen comparing T_{sfc} and T_{atm} in figures 6.16a and 6.16c.

During the daytime, the model output shows the highest SHF for the Vinkeveense Plassen, followed by Reeuwijkse Plassen and lastly the new lake. This can be explained by the relative differences in T_{sfc} for the three lakes. However, the temperature gradient above the Vinkeveense Plassen is smaller than for Reeuwijkse Plassen, which questions this result. It must be noted again that the locations of the lakes are about 10-30 km distance and the lake fractions of the studied grid cell are less than 100% for the Reeuwijkse and Vinkeveense Plassen (refer to table 5.3). Therefore, it remains difficult to make strong statements and explain their differences. At this point, we suggest that in future research care should be taken with interpreting simulations with new lakes with a cold start and we recommend including a spin-up period of a few months.

The specific humidity (q_{v}) throughout the day is depicted for all surface types and locations in figure 6.17. Assuming the lake is fully saturated with water vapor, the dip of atmospheric q_{v} observed during nighttime results in a higher humidity gradient, increasing the latent heat flux (eq. 2.18b). Around noon, q_{v} for Reeuwijkse Plassen is lower than for the new lake, potentially explaining the rise in LHF, as seen in figures 6.16b and 6.16d.

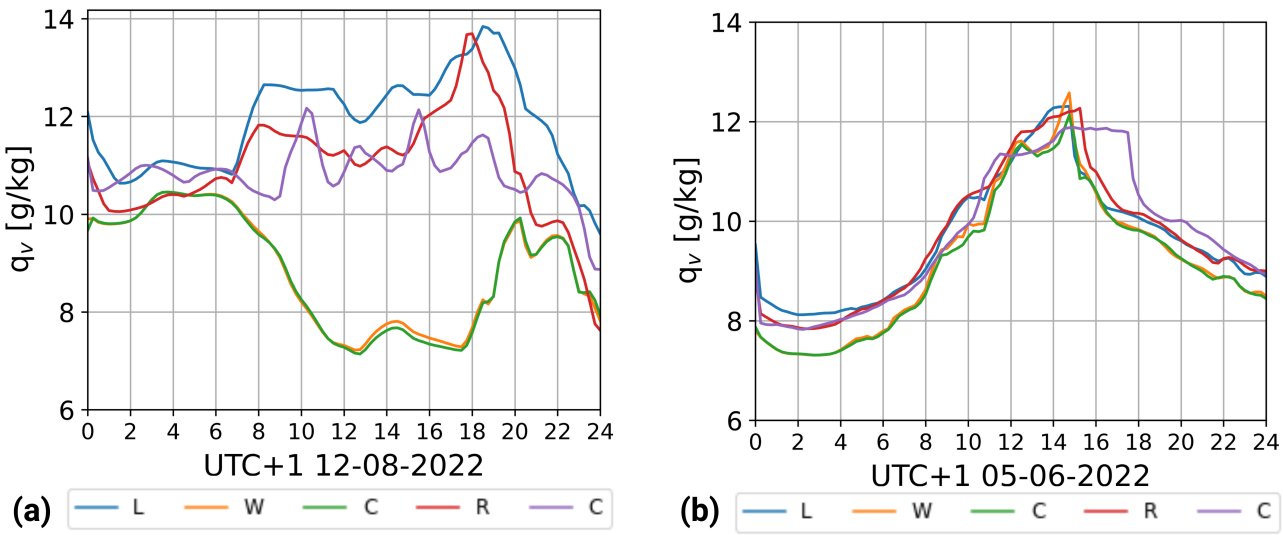

Figure 6.17: The diurnal cycle of the specific humidity for the new lake (L), wetland (W), crops (C), Reeuwijkse Plassen (R), Vinkeveense Plassen (b) and wetland (W) on (a) 12-08-2022 (extreme heat) and (b) 5-06-2022 (extreme precipitation).

In any case, for all lakes, the positive LHF leads to cooling of the lake during the night, which can be seen for the net heat flux down to - 200 W/m^2. As all the fluxes of the SEB exhibit only very small variations in time during the morning hours (till 04:00 local time), it is to be discussed whether this is due to the lake properties or due to the spin-up period of the system.

Similarly, figure 6.18 introduces temperatures and variables encompassing the SEB for a simulation with crops (figure 6.18a and 6.18b) and wetland (figure 6.18c and 6.18d). We observe a clear diurnal pattern for both the wetland and crops. The temperature differences across the land surface types are rather small.

The surface energy balance illustrated in figure 6.18b and 6.18d indicates a higher LW_{net} at the land

points of approximately 140 W/m^2 compared to the lakes (see figures 6.16b, 6.16d and 6.16f). This difference might be attributed to an increase in upward longwave radiation (LW_{up}) due to the high daytime surface temperatures of the land surfaces as compared to the lake surfaces. Moreover, during the daytime, the sensible heat flux is notably higher compared to lakes, affirming the results presented in section 6.2.1.

An interesting model result is the higher latent heat flux at the wetland and crops surface, even though the surface is not saturated with water vapor like the near the lake surface. Looking at figure 6.17a, a severe dip in q_{v} of 3 g/kg is observed during the day, which is 30% of its value in the evening and night. It is hypothesized that this phenomenon could be explained by the concept of dry entrainment. The turbulent fluxes result in the rise of hot and moist air directly above the hot surface. As a consequence of the present cold air columns adjacent to the heat plumes, mixing with the moist warm air takes place, resulting in a drop op q_{v} . This phenomenon still needs further exploration, as this dip of 30 % on a diurnal cycle is extreme. Comparing this with a day with high precipitation levels, namely 5-06-2022, the humidity pattern is considerably different (see figures 6.17a and 6.17b).

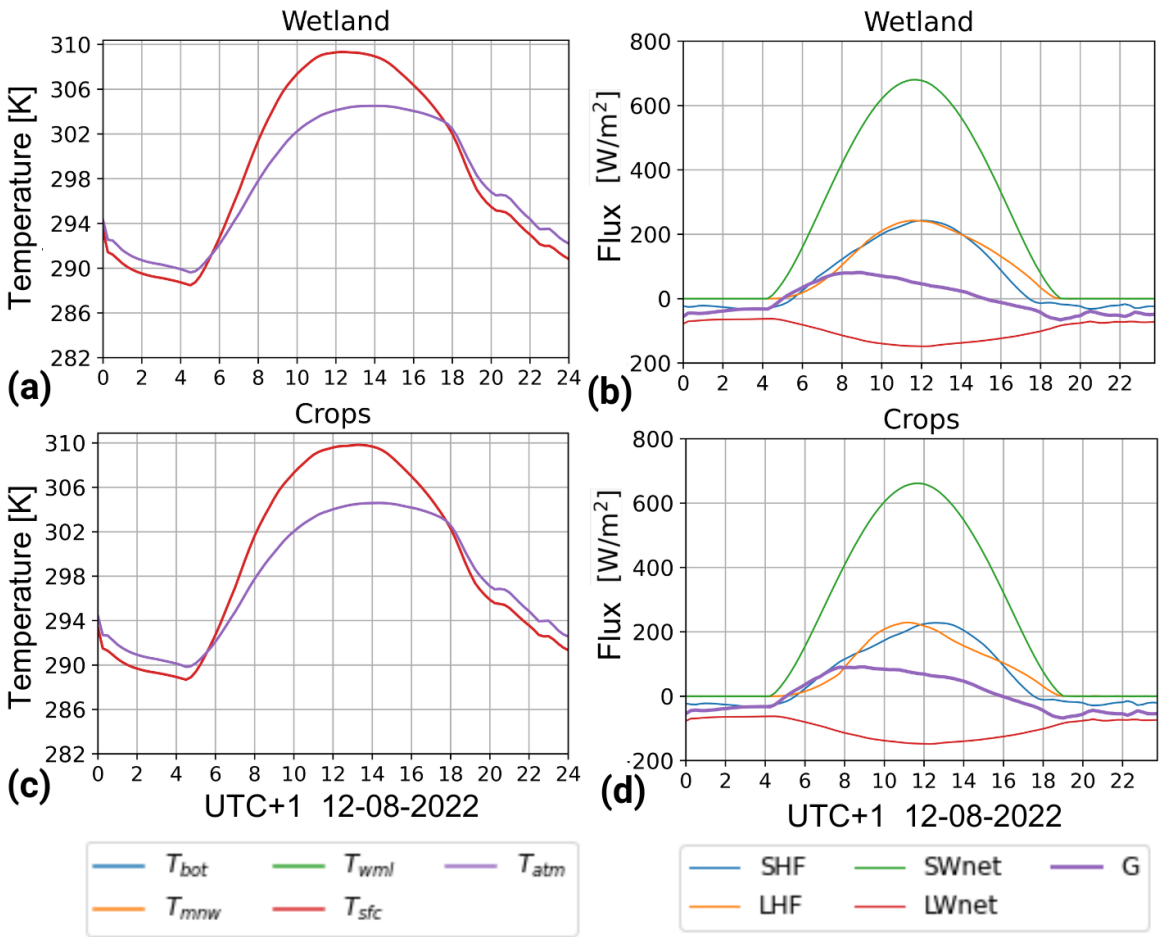

Figure 6.18: The left column displays the diurnal cycle of 12-08-2022 for the T_{sfc} (red) and T_{atm} (purple) for (a) wetland and (c) crops. The right column shows the surface energy balance (SEB) of 12-08-2022 with SHF, LHF, SW_{net}, LW_{net} and the ground heat flux G for (b) wetland (d) and crops.

7

Conclusion and recommendations

This chapter aims to further discus research results and draw conclusions to address the main research question:

How will the development of new water areas in South Holland affect the local weather?

First, we will highlight some key findings from the preliminary studies and the methods used in section 7.1.1. Next, we will discuss the final simulation results in section 7.1.2. Finally, we will provide suggestions for further research in section 7.2.

7.1. Research insights and conclusions

7.1.1. Pre-studies and methodology

To evaluate the heterogeneity of HARMONIE-Climate in urban and natural areas, a validation is done by comparing HCLIM model outputs to installed weather stations throughout the city of Rotterdam by the TU Delft and nationwide by the KNMI (chapter 3). Limitations such as varying observation heights, sub-optimal station locations, and the relatively low resolution of the HCLIM grid cell compared to point-like observations, prompt questions about model accuracy and station biases. HCLIM tends to overestimate atmospheric temperature by approximately 1.5 K during a heatwave in 2020 while underestimating temperature on regular summer days in 2021. Specific humidity is consistently underestimated during heatwaves, with a bias of approximately -1 g/kg in 2020. Though 2021 results align more closely with observations, outliers persist. Urban heat island effects are evident during the 2020 heatwave in Rotterdam, as observed by an average of 1.08 K urban-rural difference. HCLIM demonstrates better predictions of extreme specific humidity changes in rural areas compared to urban environments.

Another aspect of the research encompassed the assessment of possible land use scenarios (chapter 4). For this, multiple interviews with policymakers and researchers have been conducted. To assess the scenarios qualitatively for the purpose of the research goals, a Multi-Decision Criteria Analysis has been made, weighing the scenarios based on criteria, such as spatial resolution and the incorporation of climatology and water management aspects. A general focus lied on the development of water areas (either wetlands or lakes), as they are expected to affect mosquito development, bird migration, and viral transmission in the future. Five scenarios have been evaluated:

Redesigning Delta's, Project Delfland (ZUS et al., 2022), Ruimtelijke Verkenning by CPB (Kuiper et al., 2023), the Delta Scenarios (Wolters et al., 2018), Opportunity Map Climate Buffers by CAS (CAS, 2023) and a research project A Climate proof buffer for South Holland (Kramer, 2023). The latter has been chosen based on the MCDA evaluation, as it scored relatively high on all criteria. In the remainder of the study is this scenario used for studying changes in land use, with a water storage area localized east of Zoetermeer, in the Noordplaspolder, connecting the Rotte and Hoogeveensche Vaart.

As outlined introduction, climate change and weather conditions directly affect mosquito development, bird migration and transmission of vector-borne viruses. To set up experiments that are useful for the interdisciplinary facets of the PDPC Frontrunner project, the studied periods are carefully chosen (section 5.1). Through personal communication, literature research, and monthly KNMI weather evaluations, a selection is made. Conditions affecting the mosquito-borne disease establishment were a soft winter and spring, followed by an extremely hot summer, preferably with periods of high precipitation levels. This resulted in the period from April 1st, 2022 to September 30th, 2022.

To assess the impact of imposed land use changes in HCLIM, it is essential to modify the physiographic data (PGD) files and integrate them into the HCLIM system. The PGD files, serving as input for climate initialization, can be altered through a comprehensive workflow outlined in section 5.2, specifically tailored for the chosen water storage area location. This approach allows for assigning up to 31 cover types, such as wetlands and lakes, on a spatial resolution of about 300 by 300 m. However, it is important to note that such manipulations are experimental, and the PGD files have varying resolutions, adding complexity to the workflow.

For the experimental set-up, simulations have been executed with HCLIM with original land use (C3 and C4 crops), a new lake, and a new wetland on a default 2.5 by 2.5 km resolution grid. Also, simulations are done to further study the cold start initialization of lakes and the evolution of the temperature profile for a diurnal cycle during a heatwave (12-08-2022).

7.1.2. The effect of changes in local land use on the local weather

Distinct temperature differences in the model results are observed between the lake and agricultural land. On a local scale, the time mean reveals a surface temperature increase of 2.4 K, an atmospheric temperature rise of 0.65 K, and a 50 m temperature increase over the lake of 0.06 K (covering the entire period from 1-04-2022 till 1-10-2022). Additionally, the diurnal cycle of the temperature over land surfaces has a higher amplitude than over the lake, which is also found in Meng et al. (2023) comparing grasslands with high-altitude lakes.

The analysis of temperature patterns reveals significant differences between surface types, influencing mosquitoes' living conditions. The daily mean surface temperature (T_{sfc}) of the lake generally exceeds that of wetlands and crops, with occasional exceptions during extremely hot days. However, during the night, vegetation surfaces cool rapidly, dipping below the 290 K threshold. The lake's minimum surface temperature consistently remains above 290 K for an uninterrupted 13-week period, providing favorable conditions for *Culex pipiens* development and the establishment of viral transmission cycles (Costa et al., 2010; Vogels et al., 2016, 2017; Brown et al., 2023). Furthermore, daily mean air temperatures (T_{atm}) above the lake, wetland, and crops fluctuate within the 290 K to 301 K range. Minimum atmospheric temperatures above the lake consistently hover around 290 K (17°C) throughout the summer. The daily means and minima of T_{atm} also indicate more favorable conditions for mosquitoes and potential viral transmission due to the

presence of a lake. It is essential to acknowledge the potential overestimation of temperatures in HCLIM during hot and dry summer periods, as observed in comparisons with weather station data and mentioned in Boonekamp (2023). Furthermore, the mosquito development cycle is highly complex, and mosquitoes' favorable weather conditions vary across types, thus drawing general conclusions must be done with caution. Still, these findings emphasize the impact of land use change on temperature variations, which are related to mosquito habitat suitability.

The time-mean humidity is 1 g/kg higher above the lake as compared to the crops and shows foremost local effects. A higher humidity generally indicates better living conditions for mosquito (Brown et al., 2023; Costa et al., 2010). This result points out again the risk of virus establishment around lakes in The Netherlands (considering the spring and summer of 2022) (Brown et al., 2023; Costa et al., 2010).

Wind speeds over the lake are predominantly higher than over wetland and crops, especially during nighttime. The small roughness length of the lake as compared to the crops, decreases the vertical momentum flux, enhancing the horizontal wind over the lake and altering the habitat of species. Again results of lake-grassland observations in Meng et al. (2023), highlight similar patterns.

The sensible heat flux over the new lake is smaller compared to the land, with a time-mean decrease of 30 W/m^2. This is explained by the high diurnal temperature range of the wetland and crops, resulting in a significant increase in sensible heat flux during the daytime. During the nighttime, the lake is a constant heat source to the atmosphere, such that a positive SHF remains at the lake. The latent heat flux above the lake is higher as a result of the vertical humidity gradient, remaining positive overnight, leading to a time-mean increase of 35 W/m^2 compared to the wetland and crops. Between the original land use and wetland simulation notable differences occur in the latent heat flux, which can partly be explained by less evaporation resistance above the wetland, but must be further studied. The longwave radiation reflects directly the surface temperature differences across the studied surface types.

The effects of local changes in land use are noted throughout the Netherlands due to the chaotic behavior of atmospheric flow. The introduction of a new lake, as a small perturbation in initial conditions, induces significant differences in the weather pattern over the Netherlands. Both the perturbed and reference HCLIM simulations are driven by the same lateral domain boundaries derived from ERA5 data, prohibiting a runaway effect. This chaotic behavior has also been found in the study of Boonekamp (2023).

No similar studies have yet been performed by implementing smaller blue areas in HCLIM, but simulations with the Weather Research and Forecasting model of Ampatzidis et al. (2023) highlight temperature and humidity effects are clearly dependent on the shape and size of water bodies. A too-large water body could indeed lead to excessive heat and humidity, but the study of Ampatzidis et al. (2023) focuses on a rather small scale compared to the water area size of this research.

Impacts of lake initialization in a simulation with a cold start

In a case study during a heatwave on August 12th, 2022, the FLake model and its integration within the HCLIM system is analyzed, with a focus on evolving temperature profiles within the water column's mixed layer and the associated heat budgets. However, interpreting our findings is somewhat constrained due to the model's cold start initialization process. Currently, it technically remains impossible to run experiments of multi-day periods and obtain extra FLake model output, so no spin-up period is included. The cold start values for lake surface temperatures exhibit a difference of 4 K compared to experiments starting 4 months earlier, emphasizing this spin-up period might be necessary. Also, some initial values from the FLake output do not reflect those of the

initialization file, which points towards a yet undiscovered grid or temporal averaging process.

With a cold start, shallow lakes (≈ 2 m) show equal values for all water column and lake bottom temperatures. The temperature structure of a new lake behaves differently from a similar neighboring lake (Reeuwijkse Plassen). Additionally, we observed discrepancies between the latent heat flux and sensible heat flux and their respective temperature gradients, suggesting the need for a spin-up period.

7.2. Recommendations for future research

Further physical interpretation and validation of land use change in HCLIM
Changing land surfaces to a lake gives local changes that we understand physically, like impacts on temperatures and fluxes of heat and moisture. However, effects further away from the land use change are hard to interpret. Further research could include longer simulations of multiple years to obtain statistically better results, less prone to individual events. Also, lakes can create their own micro-climates in wind variation and turbulence. This suggests a more comprehensive and high resolution study must be done. Regional effects remain hard to interpret due to the nudging effects as a result of changing land uses in a domain fed by ERA5 data. To gain more knowledge, simulations with elaborate output and spin-up are desirable. Next to the current studied variables, lake surface wind speed and precipitation patterns could be evaluated. For the wetland and crop comparisons, the vegetation- and soil physics strike important, and could be further studied to explain differences across natural surface types.

Insights for urban designers and policymakers: are sweet lakes near sweet lake city not so sweet?
To mitigate heating within cities, nationwide municipalities and provinces are working on implementing blue-green measures. Although they are aware such nature-based solutions could enhance localized weather change and mosquito development, only a few concrete studies in the Dutch Delta present actual effects of blue-green measures on the weather conditions (Ampatzidis et al., 2023). The current study indicates that if you take too large blue-green measures such as lakes of > 2.5 km^2 or place a water buffer, it could locally significantly increase temperature and humidity levels. Although wetlands show smaller differences, human- or nature-induced development of water areas, might be a risk for enhancing the heat-humidity risk in nearby urbanized areas. Also, humans recreating nearby lakes where mosquito-bird interaction is enhanced could lead to zoonotic viral transmission. Even though it was first unexpected, viral transmission from mosquitoes to humans has been detected in the past years (Duijster et al., 2016; Zaaijer et al., 2019; Vlaskamp et al., 2020). The locations and orientations of spatial development projects should therefore be carefully considered through induced localized climatology change, also affirmed by the results of Ampatzidis et al. (2023). For example, the Opportunity Map for Natural Buffers of Climate Adaptation Services (CAS, 2023), could introduce an aspect of climatology impact when narrowing down potential locations in the future. Urban designers, policymakers, and spatial map developers should inform themselves on this matter, before deciding upon implementing blue-green areas within and nearby cities.

Explore the variety of land use scenarios and re-evaluate for a greater purpose
For further research, a more extensive assessment for the identification of wetland development and water storage areas in the Netherlands can be done. Over the course of the search for these potential areas, it becomes clear there is no uniform decision on this yet. Multiple parties remain to be contacted, and this knowledge network should be enhanced. In this research, a permanent water storage area east of Zoetermeer is eventually chosen based on a tailor-made Multi-Decision Criteria Analysis. However, based on the purpose of future research, other criteria could be in-

cluded or weighted differently. For example the outlook on how feasible the maps are in terms of politics, the potential near-future developments in each scenario, and the input from other experts such as ornithologists, entomologists and virologists. Also, it might interesting to look further than only South Holland, as this growing matter concerns the entirety of Western Europe and possibly other deltas around the globe.

Enhance collaborations with medical and environmental disciplines
Mosquitoes are known to exhibit diapause, a state of winter hibernation amidst a temperate climate, resulting in the persistence of WNV in these warmer regions (Rudolf et al., 2017; Sauer et al., 2022). Prolonged mosquito lifespan by hibernation potentially heightens the transmission risk of viruses like WNV and USUV. Also, the effect of the diurnal temperature cycle could be related to mosquito conditions. It is advisable to investigate the influence of diverse land use practices during winter periods and enhance the alignment of land use scenarios, temporal segments, and variable dynamics with interdisciplinary collaborations. The relevance of these studies and alignment of the interests will increase by enhancing collaborations with for example the Public Health Authorities (GGD).

Expand validation on TU Delft weather station data
For now, for the model-observation validation only the temperature and specific humidity levels are compared. The wind speed measurements are not compared as the lowest HCLIM model level is 10 meters, which is approximately 8 meters higher. Moreover, employing higher-resolution model results would enhance the comparability, given that the parameterizations are conducted over a more confined area in the vicinity of point-like weather stations.

Explore opportunities to implement seasonal land use change in HCLIM
In this research, the effect of water storage areas could only be simulated permanently, since it is technically impossible to modify the HCLIM system as such to implement seasonal land use change. However, it is posed that semi-permanent wetlands and water storage areas for extreme precipitation events could become a common climate mitigation measurement (CAS, 2023; Kramer, 2023). Even temporary blue-green areas might alter the mosquito and bird habitats, emphasizing the need to investigate implementation of seasonal land use changes in HCLIM.

Elongate the spin-up period for HCLIM experiments evaluating lakes
As the initialization file with climatological mean values for FLake variables has a low spatial resolution and is limited to general climatology established a decade ago by Kourzeneva et al. (2012), the lake temperatures can be under- or overestimated for short-period experiments. Therefore, if the HCLIM model would be used for temporary water storage areas or experiments, it might be interesting to study whether overruling the initialization temperatures would improve the reliability of the model results. This can be done based on the lake temperature observations from neighboring lakes. In any case, it is recommended to compare the initialization values with observations. If a longer period is studied and the initial conditions are not overruled, it is advised to run the experiments for a few months as a spin-up period to avoid misinterpretation of the model results

Enable lateral boundary and data storage improvements for high-resolution experiments
Efforts to explore changing local weather patterns with high-resolution experiments in NWP models have been made, targeting 1 x 1 km spatial and 24 s temporal resolutions. While progress has been made in applying these resolutions to lake and wetland experiments, full-scale tests remain pending due to technical challenges. Foremost, these challenges lie in the high required amount of data storage and the lack of frequently renewed lateral boundary conditions, as detailed in the Appendix B.3. High resolution experiments will enhance the local effect of anticipated land use change, for example, the changes in specific humidity on the lake sides. Besides increasing the

boundary interval for the host-nest boundary, the ERA5 data feeds lateral boundaries of the host domain on a 3-hour interval, which could be increased for improvement.

Implement automation for the modification and integration of land use scenarios
A streamlined and automated approach using Python packages, particularly Geopandas, is recommended for the modification of land use maps. The current manual workflow is time-consuming and prone to errors. By leveraging Python packages, vector data from QGIS can be directly integrated into Fortran subroutines, significantly making the process more efficient and error-free. Moreover, an automated method makes it feasible for large-scale land use modifications, a critical necessity for assessing future land use scenarios, particularly for comprehensive maps like those from Climate Adaptation Services (CAS, 2023).

Concluding this chapter, we will look back at the ramifications of the PDPC Frontrunner project presented in the introduction 1.3. This study focused specifically on the land use interventions and resulting weather condition change within Workpackage 1, indicating clear changes in the local heat-humidity levels. The expected increasing salinization due to sea level rises and subsidence of the Dutch soil, just as the implementations of pseudo climatology simulations, were out of scope. It is advised similar and more extensive simulations should be done, including the pseudo climate perturbations in HCLIM, and include HCLIM results in salinity models. With this, researchers can thoroughly contribute to advising medical and governmental parties on blue-green measures in the Dutch Delta and the potential risks of vector-borne viral outbreaks.

A

Retrospective on research choices

A.1. A wide-scale collection of land use scenarios

Workpackage 1 of the PDCP Frontrunner 1 project focuses on salinization, water management, and land use change in the Rotterdam Delta. This research mainly focused on implementing land use in a climate model and studying the resulting changing weather patterns. As climate mitigation measures are necessary and spatial development is a nationwide topic, multiple governmental or independent institutions research future scenarios of changing land use. Part of this master thesis was to explore multiple scenarios that are in development and assess the utility as input for quantitative and meteorological models. Scenarios come in all shapes and sizes, ranging from quantitative, high spatial resolution, and detailed scenarios to qualitative, low spatial resolution, and rough scenarios published on maps, reports, and more. Exploring the options entailed reaching out the all stakeholders considering land use change in the Netherlands.

- Peak water storage areas in Haarlemmermeer by Hoogheemraadschap Rijnland, `https://www.rijnland.net/wat-doet-rijnland/in-uw-buurt/piekberging-haarlemmermeer/` by Hoogheemraadschap Rijnland. Not incorporated due to missing information and not South Holland.
- Land use scenarios for disease development by Martha Dellar, part of OneHealthPact. Not incorporated as the scenarios were not finished yet.
- NL2120: Een natuurlijke toekomst voor Nederland by Wageningen University and Research, `https://www.wur.nl/nl/dossiers/dossier/nederland-in-2120.html`. Not included as it had low resolution and was indicative.
- Atelier Groen Blauw `https://www.ateliergroenblauw.nl/`. Focus city climate adaptation measures.
- Groenblauwe Netwerken `https://klimaatadaptatienederland.nl/`. Focus on city climate adapation measures.

A.2. Approach on selection weather periods of interest

	Unity	Explanation	TMY	2022	2021	2020	2019	2018
Ice	days	$T_{max} < 0°C$	8	2	7	0	2	3
Frosty	days	$T_{min} < 0°C$	53	30	50	31	40	50
Warm	days	$T_{max} > 20°C$	11	112	97	110	99	132
Summer	days	$T_{max} > 25$ °C	28	35	20	32	26	55
Tropical	days	$T_{max} > 30°C$	5	9	1	12	11	9
Total sun	hours	n.a.	1774	2233	1800	2026	1964	2090
Total precipitation	mm	n.a.	795	729	806	785	783	607

Table A.1: A numerical summary of the monthly and seasonal overviews of the Dutch weather from the KNMI (`https://www.knmi.nl/nederland-nu/klimatologie/maand-en-seizoensoverzichten/`)

In words, the years are summarized by the KNMI as following:

- **2022** Spring brought mild and dry weather after a stormy winter. Summer was very warm, sunny, and dry, especially in August. June was warm but also had significant rainfall. July had near-normal temperatures but was exceptionally dry and sunny. August ranked among the warmest and sunniest on record. Autumn was mild, quite wet, and exceptionally sunny. December experienced a cold period, ending with record-warm conditions.
- **2021** Snow in February. Winter period in February, flooding in July. Record number of code orange or red alerts. Wintry week with two instances of code red and a spring-like interlude. Extremely cold spring. Early summer weather by late March. Very cold April (6.7°C compared to 9.8°C). Second cold spring month in a row. Summer with two faces. Warm summer weather until June 18. Flooding in the southeast in July. Mild and sunny autumn, wet October. Freezing rain in a mild December.
- **2020** In general extremely warm, very sunny, and dry conditions. Extended heatwave in August. Mild winter. February exceptionally mild. Spring was mild with a record amount of sunshine and very dry. Frost in late March, cold start in April. Mild April and normal May. Warm June, cool July (17°C compared to 17.9°C), hot August. August exceptionally warm. Mild and sunny autumn, warmer than usual. October mild and wet, November mild. December mild and wet.
- **2019** Little snowfall. Mild and dry January. February characterized by mild and sunny conditions. Entire spring marked by mild temperatures. March was wet, April exceptionally sunny, and May cool. Summer saw heatwaves in late July and late August. Periods of variation, mostly dry. Autumn was relatively mild, sunny, and wet.
- **2018** Mild winter. Cold, dry, and sunny February. March exhibited varied conditions. April was exceptionally mild and wet. May experienced unusually warm temperatures. Summer averaged 19 degrees and was consistently warm. Heatwaves occurred from mid-July to early August. Autumn was mild with ample sunshine. September began warm but turned cold later on. Abundant sunshine due to high-pressure areas. October was warm and sunny. November alternated between mild and cold. December followed a normal pattern.

Based on the KNMI climatology evaluation of each year presented in table A.1 and the yearly summaries, a selection is made on whether a year would be of interest with the knowledge present at

that moment. Primarily the goal was to select 2 years: one with a period of heavy precipitation followed by heat and one with a period of drought and heat. Both with mild winters, followed by a regular spring and an extremely hot summer with heat waves.

- **Oct 2021-Sep 2022**: Yes, as it had a mild winter, a soft, dry, and sunny spring, followed by heavy rain in June and extreme heat in the summer.
- **Oct 2020-Sep 2021**: No, because it experienced an entire winter period with cold conditions and a chilly spring, accompanied by significant flooding in the summer.
- **Oct 2019-Sep 2020:** No, despite a mild winter, the spring was partly cold, and July had cold spells. Ideally, there should be at least 10 weeks with temperatures at 17 degrees or higher, and this spring/summer was too unpredictable.
- **Oct 2018-Sep 2019:** Yes, with a normal winter featuring little snow, a mild spring (although May was cool), and plenty of heat and dryness in the summer.
- **Oct 2017-Sep 2018**: Yes, as the winter was mild, and from May onwards, there was a consistently dry and warm summer, contributing to a rise in water temperatures and the occurrence of heat waves.

Ideally, the simulation would run an entire year including the preceding winter and we would run 2 years. However, due to technical difficulties, it was only possible to run 6 months, running from 1 April to 1 October. As this research focuses on water areas, a year with a period of high precipitation followed by an extreme heatwave is chosen. This resulted in 2022. Still, it is advised to run at least 1 year and multiple years to obtain more statistical data and include winter periods. The second best option is advised to be 2017-2018.

B

Process background on modifying the HCLIM system for experimental purposes

B.1. Modifying physiographic data files

B.1.1. Code for preprocessing: from QGIS to ECOCLIMAP coordinates

coord_transfer_final.ipynb

```
file_path = "/home/nlab/Documents/Buffers/Hoekpunten_Zoetermeer_Buffer.xlsx"
     # Replace with the actual path to your XLSX file
df = pd.read_excel(file_path, engine='openpyxl')

x_lon_column = df['x_lon']
y_lat_column = df['y_lat']

x_lon_list = x_lon_column.tolist()
y_lat_list = y_lat_column.tolist()

coordinates_buffer =  [(lon, lat) for lat, lon in zip(y_lat_list, x_lon_list
    )]
print(coordinates_buffer)

def coordinates2raster(coordinates,rows,columns):
    # Create a Shapely Polygon object from the polygon coordinates
    polygon = Polygon(coordinates)

    # Determine the minimum and maximum longitude and latitude within the
    polygon
    min_lon, min_lat = polygon.bounds[0], polygon.bounds[1]
    max_lon, max_lat = polygon.bounds[2], polygon.bounds[3]

    # Calculate the row and column indices within the raster that fall
    within the polygon
    min_row = math.floor((north - max_lat) / ((north - south) / rows))
    max_row = math.ceil((north - min_lat) / ((north - south) / rows))
    min_col = math.floor((min_lon - west) / ((east - west) / columns))
    max_col = math.ceil((max_lon - west) / ((east - west) / columns))

    # Create a raster array with all zeros
    raster = np.zeros((rows, columns))
```

```
    counter = 0
    lat_raster = []
    lon_raster = []
    row_raster = []
    col_raster = []

    # Set the values within the polygon to 1
    for row in range(min_row, max_row + 1):
        for col in range(min_col, max_col + 1):
            lat = north - (row * ((north - south) / rows))
            lon = west + (col * ((east - west) / columns))
            if polygon.contains(Point(lon, lat)):
                row_raster.append(row)
                col_raster.append(col)
                lat_raster.append(lat)
                lon_raster.append(lon)
                raster[row, col] = 1
                counter += 1


    polygon_raster = raster[min_row:max_row+1, min_col:max_col+1]

    return polygon_raster, lat_raster, lon_raster, counter, min_lon, min_lat
   , max_lon, max_lat

#COVER rasters
rows = 64800
columns = 129600

raster_buffer, cover_lat_raster_buffer, cover_lon_raster_buffer,
   cover_count_buffer, min_lon, min_lat, max_lon, max_lat =
   coordinates2raster(coordinates_buffer,rows,columns)

print('Number of rasterpoints on ECOCLIMAP',cover_count_buffer )
print('lat_raster_buffer',cover_lat_raster_buffer)
print('lon_raster_buffer',cover_lon_raster_buffer)

#LAKE rasters
rows = 21600
columns = 43200

raster_buffer, lake_lat_raster_buffer, lake_lon_raster_buffer,
   lake_count_buffer, min_lon, min_lat, max_lon, max_lat =
   coordinates2raster(coordinates_buffer,rows,columns)

print('Number of rasterpoints on GlobalLakeDatabase',lake_count_buffer )
print('lat_raster_buffer',lake_lat_raster_buffer)
print('lon_raster_buffer',lake_lon_raster_buffer)

data = {
    'Cover Count': [cover_count_buffer],
    'Cover Lat Raster': [cover_lat_raster_buffer],
    'Cover Lon Raster': [cover_lon_raster_buffer],
    'Lake Count': [lake_count_buffer],
    'Lake Lat Raster': [lake_lat_raster_buffer],
    'Lake Lon Raster': [lake_lon_raster_buffer],
}

df = pd.DataFrame(data)
```

```

# Define the output file path and name
output_file_path = '/home/nlab/Documents/Buffers/Change_coords_Zoetermeer_BufferV2.csv'  # Adjust the file name and path as needed

# Save the DataFrame to a CSV file
df.to_csv(output_file_path, index=False)
```

B.1.2. Modification in ECOCLIMAP-SG

This program runs the process of modifying the cover map `ecosg_final_map.dir` physiographic data file ECOCLIMAP-SG, which is embedded within HCLIM. The Ecoclimap binary file `ecosg_final_map.dir` is an integer 8 byte file with (129600x64800) data grid where for each grid cell a value between 1 and 33 should be assigned, corresponding to a land-use type. With a nearest neighbor method, the coordinates which should be changed are obtained through a workflow as described in `coord_transfer_final.ipynb`. The coordinates are now copied and pasted here. Next, the code runs over nx*nlines, and for every coordinate which where the distance is lower than the threshold (360/129600/2=0.0014), it changes. Finally, the modified region map should be put back in the original ECOCLIMAP-SG and be saved.

`mod_ecosg_cover.F90`

```
program mod_ecosg_cover

  implicit none

  ! variable declarations
  character(len=512)       :: binfile ! name of binary input file
  character(len=512)       :: outfile ! path of binary output file
  character(len=512)       :: outfile2 ! path of mask output file
  integer                  :: nx, ny, nlines, i, j, jx, jy, jp  ! dimensions and counters
  integer*1, allocatable   :: ivals(:)  ! for reading 1 byte integers
  integer*1, allocatable   :: ivals2(:)  ! for reading 1 byte integers
  real                     :: zbN, zbS, zbW, zbE  ! block definition lat/lon
  real                     :: zN, zS, zlat, zlon ! lat/lon calulcations
  real                     :: z_lat_diff, z_lon_diff,zlat_change,zlon_change, threshold  ! lat/lon calulcations
  integer, parameter :: n_changes = 360     ! Replace with the total number of elements in your list
  real, dimension(:), allocatable :: zlat_changes  ! create allocatable variable for zlat_changes
  real, dimension(:), allocatable :: zlon_changes  ! create allocatable variable for zlat_changes
  integer:: modification_count = 0

  allocate(zlat_changes(n_changes))
  allocate(zlon_changes(n_changes))

  ! Hard-coded paths and dimensions of files
  binfile = "/hpcperm/hlam/data/climate/ECOCLIMAP-SG/COVER/ecosg_final_map.dir"
  outfile = "/ec/res4/scratch/nlab/final_test/ecosg_final_map_buffer_floodedgrassland.dir"
  outfile2 = "/ec/res4/scratch/nlab/final_test/
```

```
  ecosg_final_map_buffer_floodedgrassland_mask.dir"

!Number of columns (nx) and number of rows (ny) of ECOCLIMAP
nx = 129600
ny = 64800

!The block in which we want to modify (part of the Netherlands)
zbN = 53.0
zbS = 50.0
zbW = 3.0
zbE = 5.0

! Threshold level to make sure the correct grid cell is modified
threshold = 0.0014

! Hardcoded change array (lats and lons seperatly)
zlat_changes = [52.09444444444444, 52.09444444444444, 52.09444444444444,
 ..., 52.05, 52.05, 52.05]
zlon_changes = [4.591666666666669, 4.594444444444463, 4.5972222222222285,
 ... , 4.625, 4.627777777777794, 4.63055555555556]

! Open binary files and read per n lines, modify only in subdomain of nx*
 nlines
nlines=400
allocate(ivals(nx*nlines))
allocate(ivals2(nx*nlines))

open (unit=13, file=binfile, form='unformatted', access='direct', recl=nx*
 nlines, status="old", convert='big_endian')
open (unit=14, file=outfile, form='unformatted', access='direct', recl=nx*
 nlines, status="replace", convert='big_endian')
open (unit=15, file=outfile2, form='unformatted', access='direct', recl=nx
 *nlines, status="replace", convert='big_endian')

!The for loop for modifying only in subdomain nx*nlines
do j = 1, ny/nlines, 1
  print *, j*nlines, " of ", ny
  read(unit=13, rec=j) ivals
  read(unit=13, rec=j) ivals2

  ! modify in a block, assuming 360 points per degree, and global file,
 going N -> S, turn all nature in inland water.
  zN = 90.0 - ((j-1)*nlines+0.5)/360.0
  zS = 90.0 - (j*nlines-0.5)/360.0

  !if in the block of rotterdam area
  if ( zN >= zbS .and. zS <= zbN ) then

    !loop over the changes
    do i = 1, n_changes,1
      zlat_change = zlat_changes(i)
      zlon_change = zlon_changes(i)

    ! read block and if below threshold:
      ! remember the jx and jy, calculate jp and modify in ECOCLIMAP to a
 certain value
      do jy = 1, nlines, 1
        zlat = 90.0 - ((j-1)*nlines + jy)/360.0
        z_lat_diff = ABS(zlat - zlat_change)
```

```
          if (z_lat_diff <= threshold ) then
            do jx = 1, nx, 1
              zlon = -180.0 + (jx)/360.0
              jp = (jy-1)*nx + jx
              ! change both nature as urban tiles
              if (zlon >= zbW .and. zlon <= zbE) then
                z_lon_diff = ABS(zlon - zlon_change)
                if (z_lon_diff <= threshold) then
                  print *, "Modify (", zlon, ",", zlat, ")", ivals(jp), "to"
    , 23
                  ivals(jp) = 23
                  modification_count = modification_count + 1
                !simultaneously put the mask to one
                  ivals2(jp) = 1
                endif
              endif
            enddo
          endif
        enddo
      enddo
      print*, 'Modifications:', modification_count
    endif

    write(unit=14, rec=j) ivals
    write(unit=15, rec=j) ivals2

  enddo

  close(13)
  close(14)
  close(15)

  deallocate(ivals)
  deallocate(ivals2)

end program
```

A similar code is written for the lake files `mod_lake_depth.F90` and `mod_lake_status.F90`. Here, the following things are important:

- Change `nx=129600` to `nx=43200`
- Change `ny=64800` to `ny=21600`
- Change the threshold to `threshold=` 360/43200/2 =0.0083

For the manipulation of the `GlobalLakeDepth_V3.0.dir` file with `mod_lake_depth.F90`, the record-type is 16 bytes instead of 8 bytes.

- Set `integer*1, allocatable :: ivals(:) ! for reading 1 byte integers` to `integer*2, allocatable :: ivals(:) ! for reading 2 byte integers`
- Double the reclamation number when opening and reading the files and change the conversion method. From

```
open (unit=13, file=binfile, form='unformatted', access='direct', recl=nx*
nlines, status="old", convert='big_endian') open (unit=13, file=binfile, form
='unformatted', access='direct', recl=2*nx*nlines, status="old", convert='
nation')
```

B.1.3. Changes in HCLIM system

1. Add new file paths to the location of the modified maps in Env System (make sure the modified maps keep the same name as the original ones for both the binary file and the header)

   Original

```
export PGD_DATA_PATH=$HM_CLDATA/PGD
export ECOSG_DATA_PATH=$HM_CLDATA/ECOCLIMAP-SG
```

   Modified

```
export PGD_DATA_PATH=$HM_CLDATA/PGD
export ECOSG_DATA_PATH=$HM_CLDATA/ECOCLIMAP-SG
export NEW_ECOSG_DATA_PATH=/ec/res4/scratch/nlab/final_test/cover
export FLAKE_DATA_PATH=/ec/res4/scratch/nlab/final_test/lake
```

2. Replace in Prepare PGD to the correct filepaths defined in step 1 $\Rightarrow rules212and408$.

Original

```
for PGD_TYPE in hdr dir ; do
      FILE=$ECOSG_DATA_PATH/$dirname/$FILENAME.$PGD_TYPE
      echo $FILE
      [[ -s $FILE ]] || { echo "Could not find $FILE" ; exit 1 ; }
      ln -sf $FILE .
    done
```

```
# FLake files

FLAKE_FILES="GlobalLakeStatus GlobalLakeDepth"
for FLAKE_FILE in $FLAKE_FILES ; do
  for PGD_TYPE in hdr dir ; do
   FILE=$PGD_DATA_PATH/${FLAKE_FILE}_V${LDB_VERSION}.$PGD_TYPE
   [[ -s $FILE ]] || { echo "Could not find $FILE" ; exit 1 ; }
   ln -sf $FILE ${FLAKE_FILE}.$PGD_TYPE
  done
done
```

Modified

```
for PGD_TYPE in hdr dir ; do
      FILE=$NEW_ECOSG_DATA_PATH/$dirname/$FILENAME.$PGD_TYPE
      echo $FILE
      [[ -s $FILE ]] || { echo "Could not find $FILE" ; exit 1 ; }
      ln -sf $FILE .
    done
```

```
# FLake files

FLAKE_FILES="GlobalLakeStatus GlobalLakeDepth"
for FLAKE_FILE in $FLAKE_FILES ; do
  for PGD_TYPE in hdr dir ; do
   FILE=$FLAKE_DATA_PATH/${FLAKE_FILE}_V${LDB_VERSION}.$PGD_TYPE
```

```
    [[ -s $FILE ]] || { echo "Could not find $FILE" ; exit 1 ; }
    ln -sf $FILE ${FLAKE_FILE}.$PGD_TYPE
  done
done
```

B.2. Monitoring Flake output experiments

This section is only relevant for individuals working with HCLIM within the ECMWF environment and present technical advances on FLake output experiments.

If you want netCDF4 files, it is necessary to have the conversion done in `scr/convertFA`, just like it is done for the other variables. Besides this, many other steps need to be taken. It is currently not possible to run experiments for longer than a few days, due to the limited amount of bits available for in-between data storage of sub-hourly files. Also, to convert the FA files, the code is not written for all FA files. Therefore, the current approach is experimental, works for obtaining some FLake variables as netCDF4 output, but must be further studied.

B.2.1. Technical details

The following steps should be undertaken (but are still not error-free) and allow you to read 15 min FLake variables from Masson et al. (2013), like `T_BOT, T_WML`, etcetera.

- Copy from the `/home/nlab/hm_home/23_FLK_22081213/Convert_FA` script to `FLAKE_EXPERIMENT/scr/Convert_FA`
  - This script entails some changes to help convert the FA files. Make sure `RFRMIN(24)=2.5` (to avoid differences with your regular experiments). - Add the FLake variables to the name list: `readkey%faname= "SFX.TS", "SFX.Z0" [insert variables like "SFX.T_BOT"]`

- Change the following in `config_exp.h`
  - `TFLAG="h"` ⇒ `TFLAG="min` (enables subhourly output)
  - `HWRITUPTIMES="00-760:24"` ⇒ `HWRITUPTIMES="00-45600:1440"`
  - `PWRITUPTIMES="00-760:1"` ⇒ `PWRITUPTIMES="00-45600:15"`
  - `SFXWRITUPTIMES="00-760:1"` ⇒ `SFXWRITUPTIMES="00-45600:15"`
  - `SFXWRITUPTIMES="00-760:24"` ⇒ `SFXWRITUPTIMES="00-45600:1440"`

- Copy from the `PERM` the `nam/surfex_selected_output.pm` script to `FLAKE_EXPERIMENT/nam/Surfex_selectoutput.pm`
  - Add the extra variables `TS_WATER,T_WML,T_BOT..` or others to obtain FLake variables as SFX output.

- Copy from the `PERM` the `scr/Select_postp.pl` script to `FLAKE_EXPERIMENT/scr/Select_postp.pl`
  - This script determines which output fields go into the fullpos files (PFHARM*). In this, there is a separate piece for sub-hourly output. Make sure the fields are like this to avoid aborts.
  - To write all variables quarterly `LCFU$namfpphyCLCFU $namfpphyC = [@ ];`

- Copy from the `PERM` script to `FLAKE_EXPERIMENT/scr/Setup_inline_postp.pl`
  - Increase `NMAXFPHOLD=24` to `NMAXFPHOLD=51` (or any higher number required since for every full pos step name lists have to be generated, named `NFPPHY_HOLDERS`)

- Copy from the PERM the util/gl/inc/nc_tab.h script to FLAKE_EXPERIMENT/util/gl/inc/nc_tab.h
  - Make sure the extra variables added in nam/surfex_selected_output.pm from FLake are correctly defined in here, similar to the other variables.

- Copy from the /home/nlab/hm_home/23_FLK_22081213/util/gl/netcdf/output_2_netcdf.h script to FLAKE_EXPERIMENT/util/gl/netcdf/output_2_netcdf.h

Another way to approach FLake output variables by reading its FA files is through is a python package called Epygram (https://umr-cnrm.github.io/EPyGrAM-doc/)

B.3. High resolution experiments

Currently, high resolution experiments with a spatial resolution below 2.5 by 2.5 km are purely experimental and not in operational use. When the spatial resolution is increased, the temporal resolution needs to be increased on the same scale for stability, which consequently boosts the computational time. Therefore, there are two options. Either one defines a domain with the same default settings spanning the same horizontal area, but with smaller sized grid cells and a smaller time step. The other option is to run a host experiment in the regular domain and nest a higher resolution experiment within, which uses the host experiment for the lateral boundary conditions. The regular Netherlands domain has 800 points in the the x- and y-direction with 2.5 km grid cells. If the spatial resolution is increased to 1 km, the number of grid points increase by a factor 2.5 as well and the time step need to be divided by 2.5, which results in an increase of about 6.25 times the number of points, and such an expected computation time of 15 times. Since the computational time and required data storage is so high, it is preferred to use the nested experiments.

In the host experiment, it is required to increase the write-up times of the history files to daily, since they are used for the lateral boundaries. For the nested experiment, a new domain has to be designed in the HIRLAM-NWP domain design tool.

Instead of its boundaries being 6 hourly fed by IFS scaled down by ERA5 data, the nested domain now obtains hourly input at all its boundaries from the forecast of the host experiment. To achieve this, multiple steps need to be taken in several subroutines, system and submit files.

B.3.1. Technical details

This section is only relevant for individuals working with HCLIM within the ECMWF environment and present technical advances on high resolution experiments.

It is required to first run the host experiments (example name: `HOST_EXPERIMENT`), before starting the high resolution nested experiment (example name: `NESTED_EXPERIMENT`). Although it is a computationally more efficient method than the aforementioned option, saving all the hourly SURFEX and climate files for the host experiments takes up a lot of memory space, which prevents it from running year-long experiments.

Prepare and run host experiment

1. Create a new domain (ex: `HOST_DOMAIN`) and smaller domain `NEST_DOMAIN` for the embedded high resolution experiment. Replace the domain in `scr/Harmonie_domains.pm` This can be done with `https://www.hirlam.org/nwptools/domain.html`

2. Change the configuration settings for the (`HOST_EXPERIMENT`). - `DOMAIN = HOST_DOMAIN`
   - `HWRITUPTIMES="00-760:24"` ⇒ `HWRITUPTIMES="00-760:24"`
   - `SFXWRITUPTIMES="00-760:1"` ⇒ SFXWRITUPTIMES="00-760:1"

3. Start the simulation for the `HOST_EXPERIMENT`.

Prepare and run nested experiment

1. Change the configuration settings for the (`NESTED_EXPERIMENT`). In `config_exp.h`:
   - `HOST_MODEL= "ifs"` ⇒ `HOST_MODEL= "aro"`

- HOST_SURFEX = "no" ⇒ HOST_SURFEX = "yes"
- BDLIB = /ec/res/nlab/archive/yyyy/mm/dd/hr ⇒
BDLIB = HOST_DOMAIN (now retrieves ICMSHHARM files from the host experiment)
- HWWRITUPTIMES="00-760:24" ⇒ HWRITUPTIMES="00-760:1"
- BDSTRATEGY=era5 ⇒ BDSTRATEGY=same_forecast
- BDCLIM= ../../NESTED_DOMAIN ⇒BDCLIM= ../../HOST_DOMAIN (now retrieves climate boundary climate files from HOST_EXPERIMENT)

2. In NESTED_EXPERIMENT/Env_submit:
   - Add 'e927_bd' to @scalar_list
   - Add e927_bd'MEM_PER_CPU'$job_list'' = $submit_type.' --mem-per-cpu=32000'
   (where other MEM_PER_CPU tasks are defined)

3. Copy from the PERM the Convert_FA script to NESTED_EXPERIMENT/scr/Convert_FA and add at line 211: elif ["HOST_MODEL" == "aro" -a "BDSTRATEGY" == "same_forecast "]; then chostmod="AROME"

4. In Prepare_PGD, increase the CPU:
   Prepare_pgd'MEM_PER_CPU'$job_list'' = $submit_type.' --mem-per-cpu=12000';
   ⇒
   Prepare_pgd'MEM_PER_CPU'$job_list'' = $submit_type.' --mem-per-cpu=36000';

5. Start the simulation for the NESTED_EXPERIMENT.

C

Additional figures

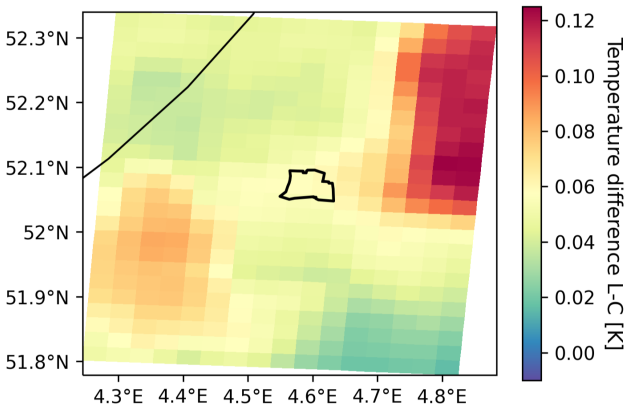

Figure C.1: The time mean difference between the simulations with lake and crops at the surface for the 50-meter temperature over a period from 1 April 2022 till 1 October 2022. A positive value indicates a higher value for the simulation with the lake as compared to the simulation with crops.

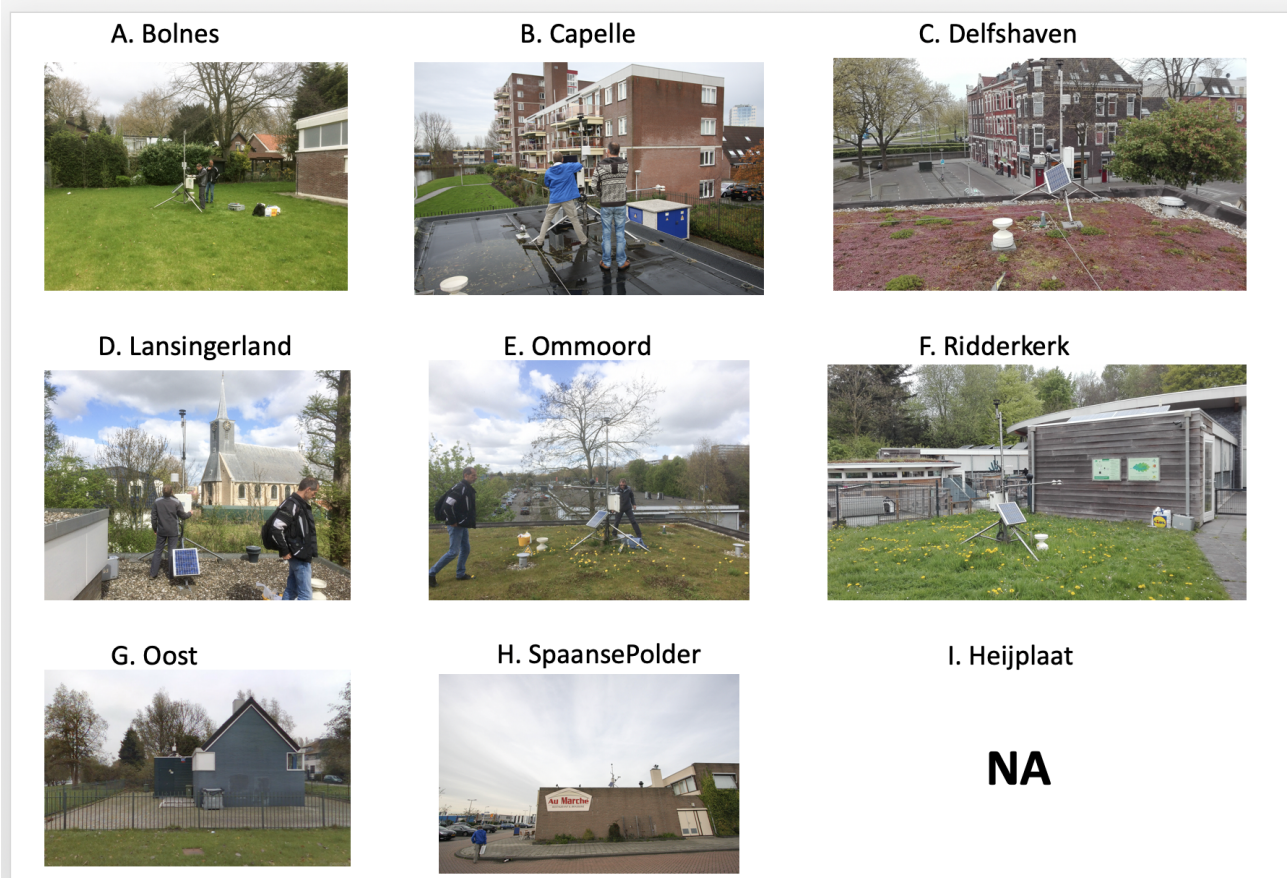

Figure C.2: A picture of all the locations of the 8 weather stations in Rotterdam placed by Delft University of Technology.

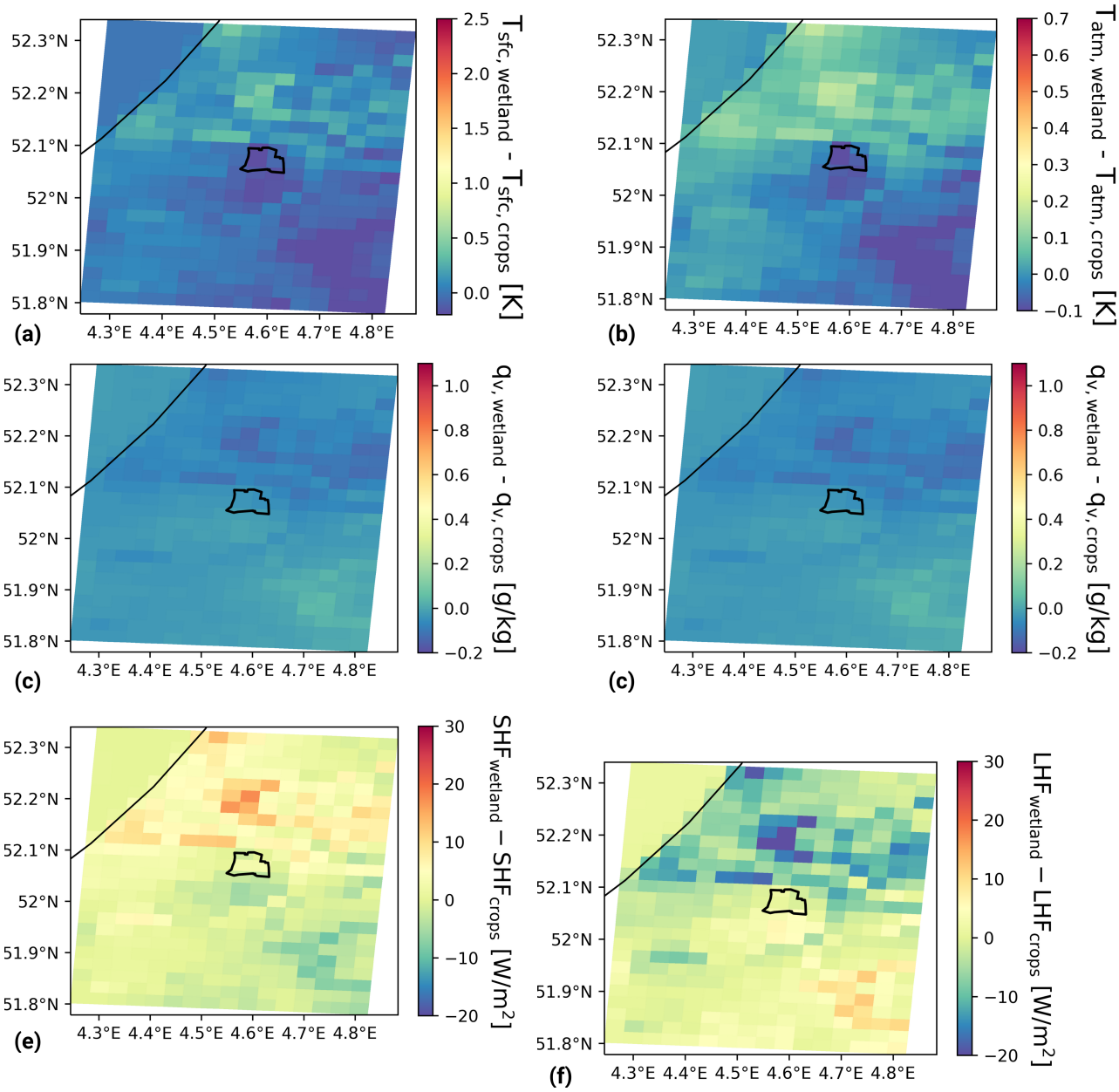

Figure C.3: The time mean difference between the simulations with wetlands and crops at the surface for (a) T_{sfc} , (b) T_{atm} , (c) q_{v} , (d) U_{spd}, (e) SHF and (f) LHF over a period from 1 April 2022 till 1 October 2022. A positive value indicates a higher value for the simulation with the lake as compared to the simulation with crops.

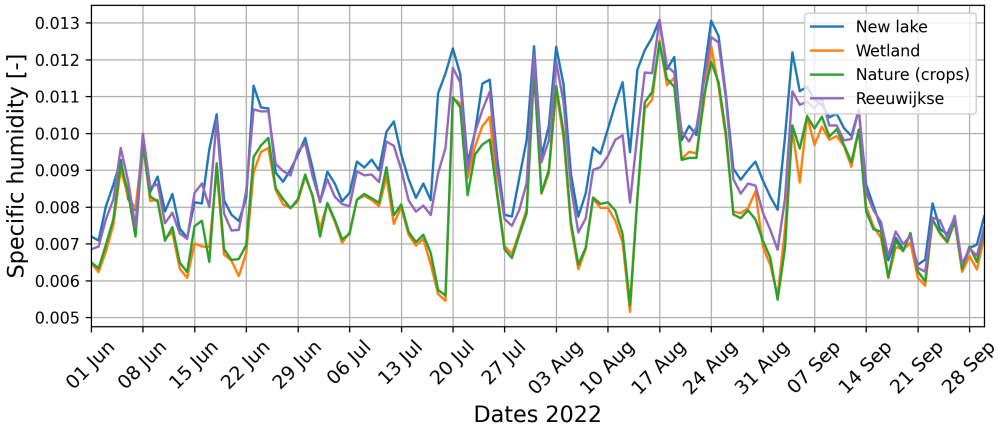

Figure C.4: The daily averages over 1 grid cell in the middle of the area for the specific humidity for the simulations for the new lake, wetland, nature (crops) and Reeuwijkse from June 1st, 2022 to September, 1st 2022.

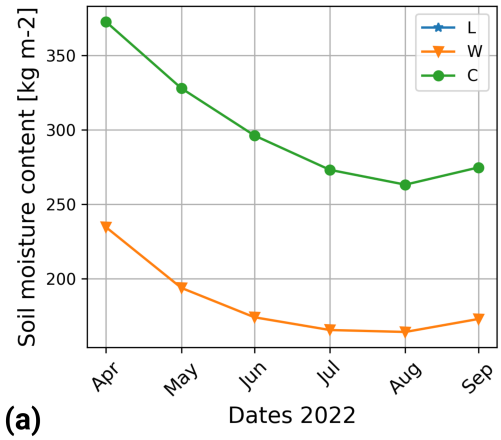

Figure C.5: The monthly averages over 1 grid cell in the middle of the area for the total soil moisture content for the simulations with surface types lake (L), wetland (W) and original land use (C) from April 2022 to September 2022.

D

Air thermodynamics

Thermodynamic quantities are directly related to surface heat fluxes. The equation of state for an ideal gas, typically used in molecular dynamics, is

$$pV = NkT, \tag{D.1}$$

The equation of state for a gas used for an atmosphere that consists of a mixture of gases like Earth is

$$p = \rho R_m T, \tag{D.2}$$

where ρ is the density, R_m is the specific gas constant of a mixture and T is the temperature. The gas law described in (D.1) law is only applicable for a single component, a similar expression must be defined for a multi-component substitution to arrive at (D.2), like dry air or air including water. According to Dalton's law of partial pressures, the total pressure of a mixture is the sum of pressures $\sum p_i$ of each species. For dry air, in the absence of water, the gas law reads:

$$p_d = \rho_d R_d T, \tag{D.3}$$

where the gas constant for dry air R_d = 287.05 Jkg^{-1} K^{-1} and p_d is the dry air pressure. The water vapor pressure is defined as

$$e_v = \rho_v R_v T, \tag{D.4}$$

where the gass constant for water vapor is R_v = 461.5 Jkg^{-1} K^{-1}

Following Dalton's law, this yields the total pressure of

$$p = p_d + e_v = \rho_d R_d T + \rho_v R_v T. \tag{D.5}$$

This gives the virtual temperature $T_v = T(1+0.608q_\mathrm{v})$. If we compare the gas laws with and without water vapor with each other, we can draw an important conclusion. Dry air constitutes mainly of nitrogen and oxygen, which have higher atom numbers hence a larger mass than that of water vapor molecules. The ideal gas law omits the effect of molecular mass, and only includes the number of molecules. If we keep the pressure, volume and temperature constant and replace all dry air molecules with the same amount of water vapor molecules, the air with water vapor has a

smaller mass and thus a smaller density. Therefore, air with water vapor rises faster. If the pressure remains constant, warm air can also hold more water, since the density of water vapor in the air is lower.

Molecules are constantly changing phases, which is called evaporation and condensation. The water vapor pressure e_v affects the rate at which water vapor molecules change phase. The rate of evaporation is thus also dependent on temperature. With a higher temperature, molecules have higher energy and can evaporate more rapidly. Now, as the air is cooled, the evaporation rate decreases more than the condensation rate does. At the dew point temperature, condensation takes the overhand and droplets can grow into a cloud drop. The point where the concentration of water vapor reaches its maximum is the saturation water vapor pressure e_{sat}.

Relative humidity is the ratio of how much moisture the air is actually holding (water vapor pressure) and how much moisture the air could hold (saturation water vapor pressure),

$$RH = \frac{e_v}{e_{\text{sat}}}, \tag{D.6}$$

often expressed in percentages.

The theoretical definition of the saturation water vapor pressure e_{sat} is defined by the Clausius-Clapeyron relation:

$$\frac{de_{\text{sat}}}{dT} = \frac{1}{T}\frac{L_v}{(v_v - v_l)}, \tag{D.7}$$

with v_v the specific volume that is occupied by water vapor. The saturation pressure only depends on the temperature.

The saturation water vapor pressure e_{sat} for typical temperatures in the atmospheric boundary layer is

$$e_{\text{sat}} = 610.78 \exp\left[\frac{17.2694(T - 273.16)}{T - 35.68}\right] \tag{D.8}$$

for the absolute temperature θ [K] and increases about 7% per K.

The saturated water vapor specific humidity q_{sat} is calculated by,

$$q_{\text{sat}} = \frac{e_{\text{sat}}}{\frac{R_v}{R_d}(p - e_{\text{sat}}) + e_{\text{sat}}} = \frac{\epsilon e_{\text{sat}}}{p + e_{\text{sat}}(\epsilon - 1)}, \tag{D.9}$$

with

$$\epsilon \equiv \frac{R_v}{R_d}. \tag{D.10}$$

The water vapor specific humidity can be approximated by the relative humidity and q_{sat} through,

$$q_v = q_{\text{sat}} \cdot RH. \tag{D.11}$$

Bibliography

C. Albergel, A. Boone, S. Belamari, B. Decharme, M. Dumont, P. Le Moigne, and V. Masson. Surfex scientific documentation. Technical report, Météo France, Laboratoire-de-Métorologique-Dynamique, German-Weather-Service, KNMI, 2018.

T. Allen, K. A. Murray, C. Zambrana-Torrelio, S. S. Morse, C. Rondinini, M. Di Marco, N. Breit, K. J. Olival, and P. Daszak. Global hotspots and correlates of emerging zoonotic diseases. *Nature Communications*, 8(1):1124, October 2017. doi: 10.1038/s41467-017-00923-8. Publisher: Nature Publishing Group.

P. Ampatzidis, C. Cintolesi, and T. Kershaw. Impact of Blue Space Geometry on Urban Heat Island Mitigation. *Climate*, 11(2):28, February 2023. ISSN 2225-1154. doi: 10.3390/cli11020028. URL `https://www.mdpi.com/2225-1154/11/2/28`.

S. Angel, J. Parent, Daniel L. Civco, A. Blei, and D. Potere. The dimensions of global urban expansion: Estimates and projections for all countries, 2000–2050. *Progress in Planning*, 75(2): 53–107, February 2011. ISSN 0305-9006. doi: 10.1016/j.progress.2011.04.001. URL `https://www.sciencedirect.com/science/article/pii/S0305900611000109`.

R. E. Baker, A. S. Mahmud, I. F. Miller, M. Rajeev, F. Rasambainarivo, B. L. Rice, S. Takahashi, A. J. Tatem, C. E. Wagner, L-F. Wang, A. Wesolowski, and C. J. E. Metcalf. Infectious disease in an era of global change. *Nature Reviews Microbiology*, 20(4):193–205, April 2022. doi: 10.1038/s41579-021-00639-z.

V. Belton and T. Stewart. *Multiple Criteria Decision Analysis: An Integrated Approach*. Springer Science Business Media, 2002.

D. Belušić, H. de Vries, A. Dobler, O. Landgren, P. Lind, D. Lindstedt, R. A. Pedersen, J. C. Sánchez-Perrino, E. Toivonen, B. van Ulft, F. Wang, U. Andrae, Y. Batrak, E. Kjellström, G. Lenderink, G. Nikulin, J-P. Pietikäinen, E. Rodríguez-Camino, P. Samuelsson, E. van Meijgaard, and M. Wu. HCLIM38: a flexible regional climate model applicable for different climate zones from coarse to convection-permitting scales. *Geoscientific Model Development*, 13(3):1311–1333, March 2020. doi: 10.5194/gmd-13-1311-2020. Publisher: Copernicus GmbH.

L. Bengtsson, U. Andrae, T. Aspelien, Y. Batrak, J. Calvo, W. Rooy, E. Gleeson, B. Sass, M. Homleid, M. Hortal, K-I. Ivarsson, G. Lenderink, S. Niemelä, K. Nielsen, J. Onvlee, L. Rontu, P. Samuelsson, D. Santos-Muñoz, A. Subias, and M. Køltzow. The HARMONIE-AROME model configuration in the ALADIN-HIRLAM NWP system. *Monthly Weather Review*, 145, February 2017. doi: 10.1175/MWR-D-16-0417.1.

A. Boone, J-C. Calvet, and J. Noilhan. Inclusion of a Third Soil Layer in a Land Surface Scheme Using the Force–Restore Method. *Journal of Applied Meteorology and Climatology*, 38(11):1611–1630, November 1999. doi: 10.1175/15200450(1999)038<1611:IOATSL>2.0.CO;2. Publisher: American Meteorological Society Section: Journal of Applied Meteorology and Climatology.

M. P. A. Boonekamp. The influence of local land use on the local weather, 2023.

L. Bounoua, R. DeFries, G. J. Collatz, P. Sellers, and H. Khan. Effects of Land Cover Conversion on Surface Climate. *Climatic Change*, 52(1):29–64, January 2002. ISSN 1573-1480. doi: 10.1023/A:1013051420309.

B. Breman, W. Nieuwenhuizen, J. Dirkx, R. Pouwels, B. de Knegt, E. de Wit, H. Roelofsen, A. van Hinsberg, P. van Egmond, G. Maas, M. van Aar, J. Veraart, R. Snep, B. van Delft, V. Mensing, Y. Hellegering, F. de Blois, I. Woltjer, N. Heidema, M. Lof, M. Mulder, L. Biersteker, M. van Eupen, R. Jochem, T. Nijs, R. de Koopman, and N. de Sena. Natuurverkenning 2050 – Scenario Natuurinclusief. 2022. doi: 10.18174/558179. Publisher: WOT Natuur & Milieu.

J. J. Brown, M. Pascual, M. C. Wimberly, L. R. Johnson, and C. C. Murdock. Humidity – The overlooked variable in the thermal biology of mosquito-borne disease. *Ecology Letters*, 26(7):1029–1049, 2023. ISSN 1461-0248. doi: 10.1111/ele.14228. URL `https://onlinelibrary.wiley.com/doi/abs/10.1111/ele.14228`.

M. Calzolari, P. Gaibani, R. Bellini, F. Defilippo, A. Pierro, A. Albieri, G. Maioli, A. Luppi, G. Rossini, A. Balzani, M. Tamba, G. Galletti, A. Gelati, M. Carrieri, G. Poglayen, F. Cavrini, S. Natalini, M. Dottori, V. Sambri, P. Angelini, and P. Bonilauri. Mosquito, Bird and Human Surveillance of West Nile and Usutu Viruses in Emilia-Romagna Region (Italy) in 2010. *PLoS ONE*, 7(5):e38058, May 2012. doi: 10.1371/journal.pone.0038058.

C. J. Carlson, G. F. Albery, C. Merow, C. H. Trisos, C. M. Zipfel, E. A. Eskew, K. J. Olival, N. Ross, and S. Bansal. Climate change increases cross-species viral transmission risk. *Nature*, 607(7919):555–562, July 2022. doi: 10.1038/s41586-022-04788-w.

CAS. Opportunity map for natural climate buffers, 2023. URL `https://www.klimaateffectatlas.nl/nl/kansenkaart-natuurlijke-klimaatbuffers`.

I. B. Celik. *Introductory turbulence modeling*. Virginia, Western Virginia University, 1999.

CNRM. Ecoclimap-sg, 2018. URL `https://opensource.umr-cnrm.fr/projects/ecoclimap-sg/wiki`.

CNRM. An introduction to surfex, 2023. URL `https://www.umr-cnrm.fr/surfex/IMG/pdf/2023_surfex_general.pdf`.

F. J. Colón-González, M. O. Sewe, A. M. Tompkins, H. Sjödin, A. Casallas, J. Rocklöv, C. Caminade, and R. Lowe. Projecting the risk of mosquito-borne diseases in a warmer and more populated world: a multi-model, multi-scenario intercomparison modelling study. *The Lancet Planetary Health*, 5(7):e404–e414, July 2021. doi: 10.1016/S2542-5196(21)00132-7. Publisher: Elsevier.

E. A. P. A. Costa, E. M. M. C. Santos, J. C. Correia, and C. M. R. de Albuquerque. Impact of small variations in temperature and humidity on the reproductive activity and survival of Aedes aegypti (Diptera, Culicidae). *Revista Brasileira de Entomologia*, 54:488–493, 2010. ISSN 1806-9665. doi: 10.1590/S0085-56262010000300021.

A. Dai, K. E. Trenberth, and T. R. Karl. Effects of Clouds, Soil Moisture, Precipitation, and Water Vapor on Diurnal Temperature Range. *Journal of Climate*, 12(8):2451–2473, August 1999. doi: 10.1175/1520-0442(1999)012<2451:EOCSMP>2.0.CO;2. Publisher: American Meteorological Society Section: Journal of Climate.

J. Damen. How well do spatially interpolated citizen weather data capture extreme weather events?, 2021.

E. Daniels, G. Lenderink, R. Hutjes, and A. Holtslag. Relative impacts of land use and climate change on summer precipitation in the Netherlands. *Hydrology and Earth System Sciences*, 20 (10):4129–4142, October 2016. ISSN 1027-5606. doi: 10.5194/hess-20-4129-2016. URL https://hess.copernicus.org/articles/20/4129/2016/. Publisher: Copernicus GmbH.

J. Duijster, A. Stroo, and M. Braks. Birds, mosquitoes and West Nile virus: Little risk of West Nile fever in the Netherlands. *Nederlands tijdschrift voor geneeskunde*, 160, January 2016.

ECMWF. Ifs documentation cy36r1 - part iv: Physical processes, 2010. URL https://www.ecmwf.int/en/elibrary/74350-ifs-documentation-cy36r1-part-iv-physical-processes.

Z. Farooq, J. Rocklöv, J. Wallin, N. Abiri, M. Odhiambo Sewe, H. Sjödin, and J. C. Semenza. Artificial intelligence to predict West Nile virus outbreaks with eco-climatic drivers. *The Lancet Regional Health. Europe*, 17:100370, June 2022. doi: 10.1016/j.lanepe.2022.100370.

S. Faroux, A. T. Kaptué Tchuenté, J.-L. Roujean, V. Masson, E. Martin, and P. Le Moigne. ECOCLIMAP-II/Europe: a twofold database of ecosystems and surface parameters at 1 km resolution based on satellite information for use in land surface, meteorological and climate models. *Geoscientific Model Development*, 6(2):563–582, April 2013. doi: 10.5194/gmd-6-563-2013. Publisher: Copernicus GmbH.

J.R. Garratt. *The atmospheric boundary layer*. Cambridge University Press, 1992.

R. Gulati and E. Donk. Lakes in the Netherlands, their origin, eutrophication and restoration: State-of-the-art review. *Hydrobiologia*, 478:73–106, June 2002. doi: 10.1023/A:1021092427559.

B. Helm, E. Gwinner, A. Koolhaas, P. Battley, I. Schwabl, A. Dekinga, and T. Piersma. Avian migration: Temporal multitasking and a case study of melatonin cycles in waders. *Progress in brain research*, 199:457–79, August 2012. ISSN 9780444594273. doi: 10.1016/B978-0-444-59427-3.00026-5.

T. Iwamura, A. Guzman-Holst, and K. A. Murray. Accelerating invasion potential of disease vector Aedes aegypti under climate change. *Nature Communications*, 11(1):2130, May 2020. doi: 10.1038/s41467-020-16010-4. URL https://www.nature.com/articles/s41467-020-16010-4. Number: 1 Publisher: Nature Publishing Group.

K. E. Jones, N. G. Patel, M. A. Levy, A. Storeygard, D. Balk, J. L. Gittleman, and P. Daszak. Global trends in emerging infectious diseases. *Nature*, 451(7181):990–993, February 2008. doi: 10.1038/nature06536. Publisher: Nature Publishing Group.

E. Kalnay and M. Cai. Impact of urbanization and land-use change on climate. *Nature*, 423(6939):528–531, May 2003. ISSN 1476-4687. doi: 10.1038/nature01675. URL https://www.nature.com/articles/nature01675. Number: 6939 Publisher: Nature Publishing Group.

S.A. Kitaygorodskiy and Y.Z. Miropolskiy. On the theory of the open-ocean active layer. *Atmospheric and Oceanic Physics*, 6(2).

KNMI. Maand- en seizoensoverzichten, a. URL https://www.knmi.nl/nederland-nu/klimatologie/maand-en-seizoensoverzichten/.

KNMI. KNMI - Implications of the KNMI'14 climate scenarios for the discharge of the Rhine and Meuse; comparison with earlier scenario studies, b. URL https://www.knmi.nl/kennis-en-datacentrum/publicatie/implications-of-the-knmi-14-climate-scenarios-for-the-discharge-of-the-rhine-and-meus

KNMI. Klimaatscenario's '23, oct 2023. URL https://www.knmi.nl/kennis-en-datacentrum/achtergrond/knmi-23-klimaatscenario-s-voor-gebruikers/.

Kay Koster, Jan Stafleu, and Esther Stouthamer. Differential subsidence in the urbanised coastal-deltaic plain of the Netherlands. *Netherlands Journal of Geosciences*, 97(4):215–227, December 2018. doi: 10.1017/njg.2018.11. Publisher: Cambridge University Press.

E. Kourzeneva, H. Asensio, E. Martin, and S. Faroux. Global gridded dataset of lake coverage and lake depth for use in numerical weather prediction and climate modelling. *Tellus A*, 64, February 2012. doi: 10.3402/tellusa.v64i0.15640.

E. Kourzevena, P. Samuelsson, G. Ganbat, and D. Mironov. Implementation of lake model FLake in HIRLAM. *HIRLAM newsletter*, 54:54–61, January 2008.

C. Kramer. A climate proof water buffer for south holland, 2023.

R. Kuiper, D. Hamers, F. Nabielek, K. van Dam, E. Dammers, E. Evenhuis, F. van Gaalen, G. de Hollander, A. van Hoorn, J. van Minnen, B. Pols, Leo. annd Rijken, T. Rood, Snellen. D. (PBL), J. (Wageningen University Research) Dirkx, and H. (Deltares) Wolters. Vier scenario's voor de inrichting van nederland in 2050. *Planbureau voor Leefomgeving*, 2023.

E. H. Loh, C. Zambrana-Torrelio, K. J. Olival, T. L. Bogich, C. K. Johnson, Jonna A. K. Mazet, W. Karesh, and P. Daszak. Targeting Transmission Pathways for Emerging Zoonotic Disease Surveillance and Control. *Vector Borne and Zoonotic Diseases*, 15(7):432–437, July 2015. ISSN 1530-3667. doi: 10.1089/vbz.2013.1563.

D. S. Lührsen, E. Zavitsanou, C. Cerecedo-Iglesias, M. Pardo-Araujo, J. R. B. Palmer, F. Bartumeus, T. Montalvo, A. Michaelakis, and R. Lowe. Adult Aedes albopictus in winter: implications for mosquito surveillance in southern Europe. *The Lancet Planetary Health*, 7(9):e729–e731, September 2023. doi: 10.1016/S2542-5196(23)00170-5. Publisher: Elsevier.

R. Mahmood, R. A. Pielke, K. G. Hubbard, D. Niyogi, G. Bonan, P. Lawrence, R. McNider, C. McAlpine, A. Etter, S. Gameda, B. Qian, A. Carleton, A. Beltran-Przekurat, T. Chase, A. I. Quintanar, J. O. Adegoke, S. Vezhapparambu, G. Conner, S. Asefi, E. Sertel, D. R. Legates, Y. Wu, R. Hale, O. W. Frauenfeld, A. Watts, M. Shepherd, C. Mitra, V. G. Anantharaj, S. Fall, R. Lund, A. Treviño, P. Blanken, J. Du, H-I. Chang, R. Leeper, U. S. Nair, S. Dobler, R. Deo, and J. Syktus. Impacts of Land Use/Land Cover Change on Climate and Future Research Priorities. *Bulletin of the American Meteorological Society*, 91(1):37–46, January 2010. ISSN 0003-0007, 1520-0477. doi: 10.1175/2009BAMS2769.1. URL https://journals.ametsoc.org/view/journals/bams/91/1/2009bams2769_1.xml. Publisher: American Meteorological Society Section: Bulletin of the American Meteorological Society.

R. Mahmood, R. A. Pielke Sr., K. G. Hubbard, D. Niyogi, P. A. Dirmeyer, C. McAlpine, A. M. Carleton, R. Hale, S. Gameda, A. Beltrán-Przekurat, B. Baker, R McNider, D. R. Legates, M. Shepherd, J. Du, P. D. Blanken, O. W. Frauenfeld, U.S. Nair, and S. Fall. Land cover changes and their biogeophysical effects on climate. *International Journal of Climatology*, 34(4):929–953, 2014. ISSN 1097-0088. doi: 10.1002/joc.3736. URL https://onlinelibrary.wiley.com/doi/abs/10.1002/joc.3736.

V. Masson, P. Le Moigne, E. Martin, S. Faroux, A. Alias, R. Alkama, S. Belamari, A. Barbu, A. Boone, F. Bouyssel, P. Brousseau, E. Brun, J.-C. Calvet, D. Carrer, B. Decharme, C. Delire, S. Donier, K. Essaouini, A.-L. Gibelin, H. Giordani, F. Habets, M. Jidane, G. Kerdraon, E. Kourzeneva,

M. Lafaysse, S. Lafont, C. Lebeaupin Brossier, A. Lemonsu, J.-F. Mahfouf, P. Marguinaud, M. Mokhtari, S. Morin, G. Pigeon, R. Salgado, Y. Seity, F. Taillefer, G. Tanguy, P. Tulet, B. Vincendon, V. Vionnet, and A. Voldoire. The SURFEXv7.2 land and ocean surface platform for coupled or offline simulation of earth surface variables and fluxes. *Geoscientific Model Development*, 6 (4):929–960, July 2013. doi: 10.5194/gmd-6-929-2013. Publisher: Copernicus GmbH.

Valéry Masson. A Physically-Based Scheme For The Urban Energy Budget In Atmospheric Models. *Boundary-Layer Meteorology*, 94(3):357–397, March 2000. doi: 10.1023/A:1002463829265.

X. Meng, S. Lyu, Z. li, Y. Ao, L. Wen, L. Shang, S. Wang, M. Deng, S. Zhang, L. Zhao, H. Chen, D. Ma, S. Li, L. Shu, Y. An, and H. Niu. Dataset of Comparative Observations for Land Surface Processes over the Semi-Arid Alpine Grassland against Alpine Lakes in the Source Region of the Yellow River. *Advances in Atmospheric Sciences*, 40:1142–1157, February 2023. doi: 10.1007/s00376-022-2118-y.

D. Mironov, G. Kirillin, E. Heise, S. Golosov, A. Terzhevik, and I. Zverev. Parameterization of Lakes in Numerical Models for Environmental Applications. January 2003.

D. Mironov, E. Kourzeneva, B. Ritter, and N. Schneider. Implementation of the lake parameterisation scheme FLake into numerical weather prediction model COSMO. *Boreal Environ. Res.*, 15, January 2009.

D. V. Mironov. COSMO Technical Report No. 11: Parameterization of Lakes in Numerical Weather Prediction. Description of a Lake Model. 2008. doi: 10.5676/DWD_PUB/NWV/COSMO-TR_11. Publisher: COSMO Consortium for Small-Scale Modelling.

A.F. Moene and J.C. Van Dam. *Transport in the Atmosphere-Vegetation-Soil Continuum*. Cambridge University Press, 2014.

C. Mora, T. McKenzie, I. M. Gaw, J. M. Dean, H. von Hammerstein, T. A. Knudson, R. O. Setter, C. Z. Smith, K. M. Webster, J. A. Patz, and E. C. Franklin. Over half of known human pathogenic diseases can be aggravated by climate change. *Nature Climate Change*, 12(9):869–875, September 2022. ISSN 1758-6798. doi: 10.1038/s41558-022-01426-1. URL `https://www.nature.com/articles/s41558-022-01426-1`. Publisher: Nature Publishing Group.

S. S. Morse. Factors in the emergence of infectious diseases. *Emerging Infectious Diseases*, 1(1): 7–15, 1995. ISSN 1080-6040. doi: 10.3201/eid0101.950102.

C. E. Moulton, J. D. Carlisle, S. J. Knetter, K. Brenner, and R. A. Cavallaro. Importance of flood irrigation for foraging colonial waterbirds. *The Journal of Wildlife Management*, 86(7):e22288, 2022. doi: 10.1002/jwmg.22288.

K. A. Murray and P. Daszak. Human ecology in pathogenic landscapes: two hypotheses on how land use change drives viral emergence. *Current Opinion in Virology*, 3(1):79–83, February 2013. ISSN 1879-6257. doi: 10.1016/j.coviro.2013.01.006. URL `https://www.sciencedirect.com/science/article/pii/S1879625713000072`.

B. Oude Munnink, E. Münger, D. F. Nieuwenhuijse, R. Kohl, A. van der Linden, C. M. E. Schapendonk, H. van der Jeugd, M. Kik, J. M. Rijks, C. B. E. M. Reusken, and M. Koopmans. Genomic monitoring to understand the emergence and spread of Usutu virus in the Netherlands, 2016–2018. *Scientific Reports*, 10(1):2798, February 2020. doi: 10.1038/s41598-020-59692-y. Number: 1 Publisher: Nature Publishing Group.

S. Paz, D. Malkinson, M. S. Green, G. Tsioni, A. Papa, K. Danis, A. Sirbu, C. Ceianu, K. Katalin, E. Ferenczi, H. Zeller, and J. C. Semenza. Permissive Summer Temperatures of the 2010 European West Nile Fever Upsurge. *PLOS ONE*, 8(2):e56398, February 2013. ISSN 1932-6203. doi: 10.1371/journal.pone.0056398. Publisher: Public Library of Science.

T. C. Pierson and M. S. Diamond. The continued threat of emerging flaviviruses. *Nature Microbiology*, 5(6):796–812, 6 2020. doi: 10.1038/s41564-020-0714-0.

J. M. Rijks, M. L. Kik, R. Slaterus, R. P. B. Foppen, A. Stroo, J. IJzer, J. Stahl, A. Gröne, M. G. P. Koopmans, H. P. van der Jeugd, and C. B. E. M. Reusken. Widespread Usutu virus outbreak in birds in the Netherlands, 2016. *Eurosurveillance*, 21(45):30391, November 2016. ISSN 1025-496X. doi: 10.2807/1560-7917.ES.2016.21.45.30391.

D. J. Rogers and S. E. Randolph. Climate Change and Vector-Borne Diseases. In Simon I. Hay, Alastair Graham, and David J. Rogers, editors, *Advances in Parasitology*, volume 62 of *Global Mapping of Infectious Diseases: Methods, Examples and Emerging Applications*, pages 345–381. Academic Press, January 2006. doi: 10.1016/S0065-308X(05)62010-6.

M. Romanello, C. di di Napoli, C. Green, H. Kennard, P. Lampard, D. Scamman, M. Walawender, Z. Ali, N. Ameli, S. Ayeb-Karlsson, P. J. Beggs, K. Belesova, L. B. Ford, K. Bowen, W. Cai, M. Callaghan, D. Campbell-Lendrum, J. Chambers, T. J. ... Cross, Hugh Montgomery, and Anthony Costello. The 2023 report of the Lancet Countdown on health and climate change: the imperative for a health-centred response in a world facing irreversible harms. *The Lancet*, 0(0), November 2023. ISSN 0140-6736, 1474-547X. doi: 10.1016/S0140-6736(23)01859-7. URL `https://www.thelancet.com/journals/lancet/article/PIIS0140-6736(23)01859-7/fulltext`. Publisher: Elsevier.

I. Rudolf, L. Betášová, H. Blažejová, K. Venclíková, P. Straková, O. Šebesta, J. Mendel, T. Bakonyi, F. Schaffner, N. Nowotny, and Z. Hubálek. West Nile virus in overwintering mosquitoes, central Europe. *Parasites & Vectors*, 10(1):452, October 2017. ISSN 1756-3305. doi: 10.1186/s13071-017-2399-7. URL `https://doi.org/10.1186/s13071-017-2399-7`.

F. G. Sauer, E. Timmermann, U. Lange, R. Lühken, and E. Kiel. Effects of Hibernation Site, Temperature, and Humidity on the Abundance and Survival of Overwintering Culex pipiens pipiens and Anopheles messeae (Diptera: Culicidae). *Journal of Medical Entomology*, 59(6):2013–2021, November 2022. ISSN 0022-2585. doi: 10.1093/jme/tjac139. URL `https://doi.org/10.1093/jme/tjac139`.

Y. Seity, P. Brousseau, S. Malardel, G. Hello, P. Bénard, F. Bouttier, C. Lac, and V. Masson. The AROME-France Convective-Scale Operational Model, Mon. *Weather Rev*, 139:976–991, January 2010.

R. S. Sikkema, M. Schrama, T. van den Berg, J. Morren, E. Munger, L. Krol, J. G. van der Beek, R. Blom, I. Chestakova, A. van der Linden, M. Boter, T. van Mastrigt, R. Molenkamp, C.J.M. Koenraadt, J.M.A. van den Brand, B. B. Oude Munnink, M.P.G Koopmans, and H. van der Jeugd. Detection of West Nile virus in a common whitethroat (Curruca communis) and Culex mosquitoes in the Netherlands, 2020. *Euro Surveillance: Bulletin Europeen Sur Les Maladies Transmissibles = European Communicable Disease Bulletin*, 25(40):2001704, October 2020. doi: 10.2807/1560-7917.ES.2020.25.40.2001704.

S. M. Sterling, A. Ducharne, and J. Polcher. The impact of global land-cover change on the terrestrial water cycle. *Nature Climate Change*, 3(4):385–390, April 2013. doi: 10.1038/nclimate1690. Number: 4 Publisher: Nature Publishing Group.

K. R. van Daalen, M. Romanello, J. Rocklöv, J. Semenza, C. Tonne, A. Markandya, N. Dasandi, S. Jankin, H. Achebak, J. Ballester, H. Bechara, M. W. Callaghan, J. Chambers, S. Dasgupta, P. Drummond, Z. Farooq, O. Gasparyan, N. Gonzalez-Reviriego, ... Hamilton, J. M. Anto, M. Nilsson, and R. Lowe. The 2022 Europe report of the Lancet Countdown on health and climate change: towards a climate resilient future. *The Lancet Public Health*, 7(11):e942–e965, November 2022.

C. van Heerwaarden. *Surface evaporation and water vapor transport in the convective boundary layer*. PhD thesis, Wageningen University, 2011.

P. H. Verburg, J. R. Ritsema van Eck, T. C. M. de Nijs, M. J. Dijst, and P. Schot. Determinants of Land-Use Change Patterns in the Netherlands. *Environment and Planning B: Planning and Design*, 31 (1):125–150, February 2004. ISSN 0265-8135. doi: 10.1068/b307. URL `https://doi.org/10.1068/b307`. Publisher: SAGE Publications Ltd STM.

D. R. M. Vlaskamp, S. Thijsen, J. Reimerink, P. Hilkens, W. H. Bouvy, S. E. Bantjes, B.J.M. Vlaminckx, H. Zaaijer, H. T. C. van den Kerkhof, S. F. H. Raven, and C. Reusken. First autochthonous human West Nile virus infections in the Netherlands, July to August 2020. *Euro Surveillance: Bulletin Europeen Sur Les Maladies Transmissibles = European Communicable Disease Bulletin*, 25(46): 2001904, November 2020. doi: 10.2807/1560-7917.ES.2020.25.46.2001904.

C. B. F. Vogels, J. J. Fros, G. P. Göertz, G. P. Pijlman, and C. J. M. Koenraadt. Vector competence of northern European Culex pipiens biotypes and hybrids for West Nile virus is differentially affected by temperature. *Parasites & Vectors*, 9(1):393, July 2016. doi: 10.1186/s13071-016-1677-0.

C. B. F. Vogels, N. Hartemink, and C. J. M. Koenraadt. Modelling West Nile virus transmission risk in Europe: effect of temperature and mosquito biotypes on the basic reproduction number. *Scientific Reports*, 7(1):5022, July 2017. doi: 10.1038/s41598-017-05185-4. Number: 1 Publisher: Nature Publishing Group.

B. Wang, Y. Ma, Y. Wang, Z. Su, and W. Ma. Significant differences exist in lake-atmosphere interactions and the evaporation rates of high-elevation small and large lakes. *Journal of Hydrology*, 573:220–234, June 2019. ISSN 0022-1694. doi: 10.1016/j.jhydrol.2019.03.066. URL `https://www.sciencedirect.com/science/article/pii/S0022169419302951`.

T. T. Warner. *Numerical Weather and Climate Prediction*, volume 19. Cambridge University Press, 2012. doi: 10.1002/met.1309.

S. C. Weaver and W. K. Reisen. Present and future arboviral threats. *Antiviral Research*, 85(2):328–345, February 2010. doi: 10.1016/j.antiviral.2009.10.008.

N. D. Wolfe, C. P. Dunavan, and J. Diamond. Origins of major human infectious diseases. *Nature*, 447(7142):279–283, May 2007. ISSN 1476-4687. doi: 10.1038/nature05775. URL `https://www.nature.com/articles/nature05775`. Number: 7142 Publisher: Nature Publishing Group.

H.A. Wolters, G.J. van den Born, and Reinhard E. S. Dammers. Deltascenario's voor de 21e eeuw, actualisering 2017. *Deltares*, 2018.

H. L. Zaaijer, E. Slot, M. Molier, C. B. E. M. Reusken, and M. H. G. M. Koppelman. Usutu virus infection in Dutch blood donors. *Transfusion*, 59(9):2931–2937, 2019. ISSN 1537-2995. doi: 10.1111/trf.15444.

X. Zhang, F. W. Zwiers, G. C. Hegerl, F. H. Lambert, N. P. Gillett, S. Solomon, P. A. Stott, and T. Nozawa. Detection of human influence on twentieth-century precipitation trends. *Nature*, 448(7152):461–465, July 2007. ISSN 1476-4687. doi: 10.1038/nature06025. URL `https://www.nature.com/articles/nature06025`. Number: 7152 Publisher: Nature Publishing Group.

B. Zondag, M. de Bok, K. T. Geurs, and E. Molenwijk. Accessibility modeling and evaluation: the TIGRIS XL land-use and transport interaction model for the Netherlands. *Computers, environment and urban systems*, 49:115–125, July 2015. doi: 10.1016/j.compenvurbsys.2014.06.001. Publisher: Elsevier.

ZUS, Flux, and Sweco. *National Productive Park Delftland: Redesigning Delta.* 2022.